MICROFABRICATED PRESSURE TRANSDUCERS BASED ON ANTI-RESONANT REFLECTING OPTICAL WAVEGUIDES

by

Albert Min-Hsien Young

B.A. The Johns Hopkins University (1986)
S.M. Massachusetts Institute of Technology (1989)

Submitted to the

DEPARTMENT OF ELECTRICAL ENGINEERING AND COMPUTER SCIENCE

in partial fulfillment of the requirements

for the degree of

DOCTOR OF PHILOSOPHY

at the

MASSACHUSETTS INSTITUTE OF TECHNOLOGY

February 1994

Signature of Author _____
Department of Electrical Engineering and Computer Science
January 31, 1994

Certified by _____
Professor Stephen D. Senturia
Barton L. Weller Professor of Electrical Engineering
Thesis Supervisor

Accepted by _____
Professor Frederic R. Morgenthaler
Chair, Department Committee on Graduate Students

MICROFABRICATED PRESSURE TRANSDUCERS BASED ON ANTI-RESONANT REFLECTING OPTICAL WAVEGUIDES

by

Albert M. Young

Submitted to the Department of Electrical Engineering and Computer Science
on January 31, 1994 in partial fulfillment of the requirements
for the Degree of Doctor of Philosophy in Electrical Engineering and Computer Science

Abstract

Silicon microstructure fabrication and integrated optics technology have both progressed rapidly in recent years. The use of these two technologies to create a new class of integrated-optical microsensors remains a potentially important area to explore. One interesting possibility is the use of evanescent loss effects to measure the interaction between a deformable microstructure and an optical waveguide. This work reports on a specific device design using silicon-based integrated optics to fabricate a waveguide-based pressure transducer. The device uses laser light coupled into an optical waveguide that has its leakage enhanced by interaction with a deformable silicon diaphragm located a small distance above the waveguide. Since the attenuation level is a strong function of gap spacing, monitoring the waveguide output can give a measure of the diaphragm deflection, and hence can be related to the pressure applied to the diaphragm.

Ease of alignment was identified as a critical issue for the manufacturability of such a sensor, since fiber-to-waveguide alignment procedures can add significantly to total device cost. The waveguide structure chosen to help ease alignment tolerances is based on the anti-resonant reflecting optical waveguide (ARROW) principle, where light is confined in a low index core through total internal reflection at the top interface, and high grazing angle reflections enhanced by Fabry-Perot effects at the lower interface. This structure has a guiding layer which is quite large by integrated optic standards and is well matched to single-mode optical fiber.

Microsensors based on these concepts have been fabricated and tested. This work demonstrates that evanescent loss can be used to detect the interaction between an optical waveguide and a leakage-inducing attenuator. First order simulation models were successful in discovering the salient features of device operation, with the exception of the apparent stiffening of the diaphragm in the small deflection regime. This problem is attributed to small particulates entrapped in the gap spacing and can be modelled empirically by using an effective spring constant. Input / output coupling tolerances are somewhat improved by going to the ARROW structure. However, this improvement comes at the expense of the introduction of higher order modes into the structure, which can complicate alignment procedures and can decrease the effective signal-to-noise ratio when devices are scaled down to smaller dimensions. The main advantage of ARROW waveguides, improved coupling efficiency, may not necessarily outweigh its disadvantages, since a standard waveguiding structure with high insertion loss may still be acceptable if one has enough measurement headroom. Results of these studies and directions for future research will be presented.

Thesis Supervisor: Stephen D. Senturia

Title: Barton L. Weller Professor of Electrical Engineering

Acknowledgments

This work required the assistance of a great many people whose help cannot be over-emphasized. Building up a program involving the combination of integrated optics and silicon microstructures was an exciting project, and I hope all of those who gave so much help to me were able to catch some of that excitement. First, I would like to acknowledge the support of Prof. Steve Senturia who undoubtedly has made many important contributions to this work. I would also like to thank him for his constant support, and for the courage he showed in exploring a completely new area of research with me. I must also give great thanks to Chenglin Xu and Prof. Weiping Huang who helped in much of the simulation work involved in device design. The few days I spent with them at the University of Waterloo were quite important to the progress of this work, and I have fond memories of my travels there. I should also thank Karl Kissa of the Charles Stark Draper Laboratory, who helped me run simulations a little closer to MIT. I would also like to thank my thesis readers, Profs. Hermann Haus and Shaoul Ezekiel, for our discussions on leaky waves, device modelling, and ways to improve this document.

Prof. Marty Schmidt helped provide support for this work and provided much useful information about wafer bonding technologies. Leonard Johnson provided much useful hands on advice for getting started in the world of integrated optics. Having been through the typical experiences in the optics laboratory, I have come to see the importance of his advice. I need to thank Susan Noe and the group of Modest Oprysko at the IBM T.J. Watson Research Center for their assistance as well. Susan and I thought at great length about what our little optical corner of the world would look like, and without her efforts this project would certainly not be anywhere near where it is today. Also, for solving problems in all the days of the project's infancy, the help of John Jackson of Metricon is gratefully appreciated. I would like to thank Profs. Mike Duguay and Francois Ouellette of Laval University for interesting discussions on the prospects of ARROW waveguides and for help with multilayer film analysis. Richard Soref and Debra Koker were also of great help in the analysis of the waveguides.

Fabrication and testing also proved to be quite a challenge, and I was fortunate enough to able to explore quite a number of trails that I could not have travelled alone. Craig Keast provided help in film deposition and polishing. Skip Hoyt also provided assistance in polishing waveguide end-faces. David Breslau provided many creative ideas in the machining of the testing apparatus. Kohichi Tamura provided assistance in finding equipment to measure mode profiles. Jay Damask provided assistance with fiber-tip etching and lensing. Of course, no acknowledgment could be remotely complete without thanks to the staff of the Microsystems Technology Laboratories. Octavio Hurtado, Joe DiMaria, Paul Tierney, Tim Tyson, Brian Foley, Rob Cuikay, Jim Bishop, Joe Walsh, Bernard Alamariu, Nestore Polce, Dick Westberg, Velma McClure, Rudy Lia, Mark Laroche, Paul McGrath: thanks to all of you. This work made it only because of your dedicated efforts in the lab. Of course, thanks also go out to Linus Cordes and Pat Burkhart who made the lab a pleasant place to work.

I would like to thank all the members of our "mega-group" that I have interacted with over the years. Scotti Fuller gets special thanks for her administrative support. I am also glad that guys like Jeff Pan, Aleks Nikolich, Mike Huff, and Vince McNeil were always there to bounce around ever-changing ideas about our field. Peter Osterberg provided help with the mechanical simulations reported in this work. Dan Sobek provided immeasurable support in the fabrication laboratory. I owe a great deal of my current sanity to his extra effort. Of course, a great deal of sanity was also spared through my interactions with the old gang: Tony Yen, Yao-Ching Ku, Bill Chu, Joe Kung, Vince Wong, Lisa Su, Martin Burkhardt, and Ken Yee. Late nights at work just wouldn't have been the same without them.

Partial support for this work was provided by 3M. I'd like to extend a thank you to John Huizinga and Yvonne Cadwallader for helping to hatch the ideas for this work. Thanks also to Ron Schmid for financial support.

Finally, a great big thank you to Melanie Sherony, who has been an incredibly positive influence in my life during the completion of this work. And thanks to Mom, Dad, and Janice -- I couldn't have done it without you.

Contents

List of Figures

List of Tables

Chapter 1

Introduction

1.1 Goals

Silicon microstructure fabrication and integrated optics technology have both progressed rapidly in recent years. It is interesting to ask if these technologies can be combined to form a new class of microsensors. Such a sensor would have a variety of advantages, especially for applications in harsh environments. However, before such sensors can be designed, some fundamental issues must be addressed. The first involves finding a suitable mechanism for transducing a mechanical action into optical modulation, where we define "optical modulation" in the conventional optical sense, i.e. the alteration of a detectable property of a coherent light wave. In this work, intensity is the detectable property of interest; hence, this class of interaction is often referred to as intensity-modulation. More specifically, this work investigates whether evanescent loss can be used effectively to measure the level of interaction between a deformable silicon microstructure and an integrated optical waveguide. Another critical issue is that of improving the ease of alignment for coupling to such a sensor. At present, packaging and alignment considerations add greatly to the cost of integrated optical components. This work attempts

to discover if these input / output difficulties can be significantly reduced by designing an appropriate waveguiding structure, such as the anti-resonant reflecting optical waveguide (ARROW).

The vehicle used to address these concerns is a specific device design that incorporates a silicon-based ARROW waveguide in the microfabrication of a pressure and force transducer. A fabrication process for such a device was developed and completed devices were tested. Results from numerical simulation studies were compared with experimental results to determine our level of understanding of device operation. This thesis tries to provide a thorough understanding of the issues relevant to the design of such a sensor.

1.2 Background

1.2.1 Silicon-Based Integrated Optics and Microstructures

The field of integrated optics has seen tremendous growth over the last thirty years, driven forward largely by the drive for optical communication [1-3]. Interest in silicon-based integrated optics has found renewed interest in the last ten years as well [4,5]. Many of its advantages stem from its ability to leverage off of the semiconductor industry. Silicon is a technology that is already mature for mass production. The substrates offer very high surface quality over large areas. Patterned processing such as photolithography is well developed and high levels of integration are possible. Additional advantages come from silicon's inherent material properties. Silicon is a robust material with good mechanical stability [6]. It has a high thermal conductivity that makes it attractive for use as a substrate for lasers and amplifiers. Furthermore, the crystalline nature of silicon allows

anisotropic etching of V-grooves, which can facilitate the attachment of optical fibers [7,8]. A final set of advantages come from the electronic properties of silicon. Complete hybrid optical packages on silicon are currently being pursued to take advantage of these ideas [9].

In addition to the use of silicon as a substrate, there is a large body of work dealing with the waveguiding materials that can be deposited on silicon. These include materials such as silicon nitride, doped glasses, and other types of silicon dioxides [10-14]. For example, high pressure oxidation (HIPOX) [13] and flame hydrolysis [14] have both been used in the fabrication of modern waveguiding devices. In fact, silicon itself is emerging as a potential waveguiding material since it is transparent at communication wavelengths.

Silicon microsensors have been explored extensively over the last fifteen years. Silicon microstructure fabrication has been used in the construction of a variety of pressure transducers, including sensors based on piezoresistive [15-19] and capacitive [20-23] detection schemes. Optical sensors combining microstructures with fiber-optic technologies have also seen rapid developments in the last several years. A commercial sensing system (MetriCor, FiberOptic MultiSensor^{TM} System) based on the ratiometric comparison of spectral shifts has been on the market for over six years. In addition, a number of fiber-optic sensors have been developed based on methods including: interferometry [24-26], shutter modulation [27], reflectivity [28], evanescent loss [29,30], and digital encoding [31]. These sensors are particularly suited to applications in harsh environments such as high-temperature or explosive locations, and to applications where immunity to large bands of electromagnetic interference is important. The low cost of optical fiber and the simplicity of processing required to fabricate devices have made them attractive for many applications. Integrated optical sensing devices hope to garner many of the benefits of fiber optic sensors as well as a few additional advantages. For example, patterning capabilities in integrated optics should give the designer better control over the

nature of light in the waveguide and the topologies of waveguide that are possible. In addition, better control of the index profile and hence the structure of the optical field should be possible with integrated optical devices. Alignment of critical components may be easier with such devices as well, since photolithographic capabilities can align waveguides with sub-micron accuracy. Although the combination of the disciplines of integrated optics and microstructures is quite a recent event, the capabilites of integrated optical microsensors can be expected to grow in the future as technologies for optical communication and the semiconductor industry continue to improve.

Silicon-based integrated optics for sensing applications has recently received serious attention [32,33]. Position sensors [34] and accelerometers [35] have been designed using silicon technology. In addition, microfabricated pressure sensors based on interferometry have been built [36-38]. Integrated optical sensors using evanescent techniques have been fabricated to sense changes in a liquid medium above a light-carrying waveguide [39], as well as to probe layers of molecules adsorbed to the waveguide surface [40]. However, work studying the effect of solid-phase structures on integrated optical waveguides remains limited. Lukosz and Plinka [41-43] have shown that the interaction of an optical waveguide with a component of lower refractive index creates a shift in the propagation constant, β, and hence the effective-index, β/k_o, of the entire structure. This shift does not directly result in a change of waveguide power; however, the phase change created can be converted to an intensity shift by using an interferometric configuration. Unfortunately, interferometers are generally extremely sensitive to a variety of stimuli and thus may not be suitable for some sensor applications. This thesis investigates the use of attenuators with indices higher than the waveguide effective-index in order to enhance waveguide leakage. This should provide a path towards a more direct method of intensity modulation.

1.2.2 The Anti-Resonant Reflecting Optical Waveguide (ARROW)

At the time of this writing, fiber-to-waveguide coupling is still not a fully mature technology. Coupling from large single-mode waveguides (> 4 μm diameter) to other similarly large waveguides has improved greatly as optical fiber alignment technologies have begun to enter the market. However, coupling to single-mode waveguides as fabricated in silicon remains difficult to accomplish with low insertion loss. This is primarily due to the high index difference between most silicon-based waveguides and their cladding layers, which means that very thin guiding layers are required in order to maintain single-mode operation. This single-mode operation is desirable because an evanescent-loss-based sensor depends on the ability to control the evanescent tail of the propagating wave. A lower index differential between the guiding and cladding layers can be used to enlarge the spatial profile of the beam. However, this results in the need for a large buffer layer between the waveguide and the substrate, which can be prohibitively costly.

Lenses may be used to reduce the beam waist to achieve greater coupling efficiencies into the waveguide. There are a number of manufacturers of microfabricated lenses and lens holders in both glass and plastic. While tolerances in manufacturing have improved greatly, handling these components is difficult to automate, and assembly of lensing systems to required tolerances remains an expensive process. Another technique recently developed to circumvent this problem involves the direct lensing of the optical fiber tip itself, which will be discussed in greater detail in Chapter Five. Unfortunately, microfabricated lens alignment and fiber-tip lensing are both still difficult to perform repeatably.

Another idea for easing the alignment tolerances on the waveguide structure is to change the structure itself. In a standard optical waveguide, light is confined in a core

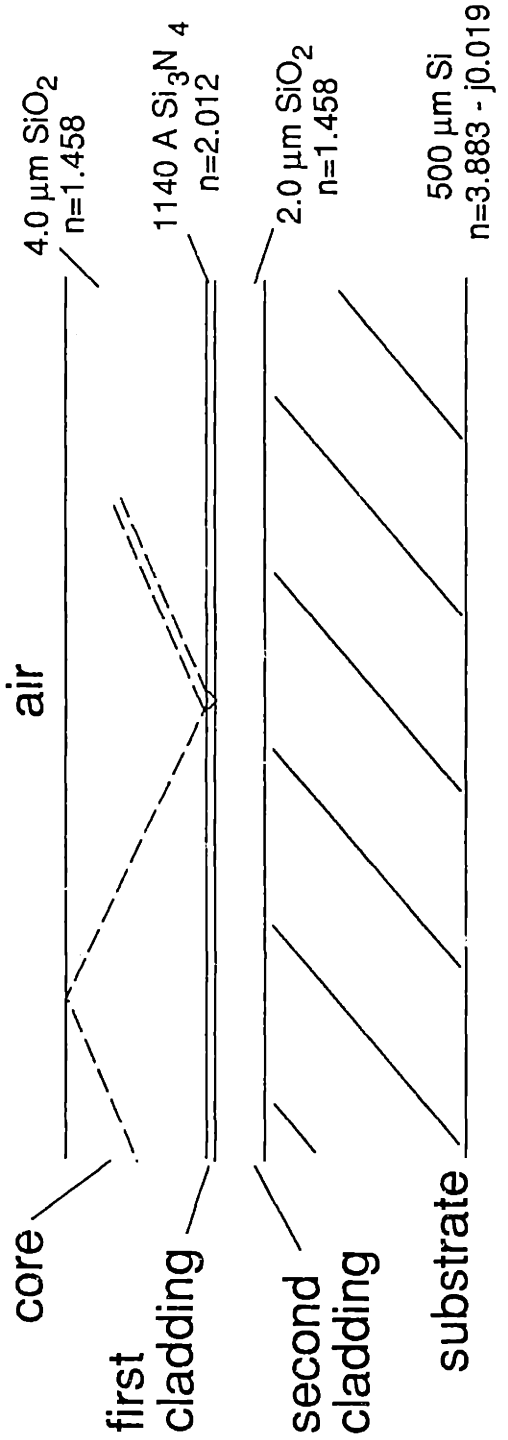

Fig. 1 Cross-section of anti-resonant reflecting optical waveguide (ARROW)

region with a refractive index which is higher than its surroundings. However, another class of optical waveguides, known as leaky waveguides, exists in which the core index is actually lower than that of its surroundings. The functionality of these waveguides is limited by leakage loss, but this loss can be reduced significantly if the layers of the guiding structure are designed carefully. One example of such a device design is the anti-resonant reflecting optical waveguide (ARROW) which is shown in Fig. 1.

This particular structure is designed for operation at He-Ne wavelengths (0.6328 μm) and consists of a low-temperature-deposited silicon dioxide core (n=1.458) of 4.0 μm, a silicon nitride first cladding layer (n=2.012) of 1140 Å, and a thermally grown silicon dioxide second cladding layer (n=1.458) of 2.0 μm. This structure has many advantages: most notably the fact that it allows coupling into a large, low-index waveguide as opposed to a very thin, high-index waveguide. Thus, fiber-coupling losses due to spatial and index mismatch can be reduced, and alignment tolerances can be increased.

In a typical ARROW waveguide, the light propagating in the core layer is totally internally reflected at the core-air interface and is separated from the substrate by a two-layer interference cladding. This two-layer cladding provides a set of interfaces with large index differences in order to increase the reflectivity at each interface. If the core layer is thick enough, the fundamental mode will propagate with a near-grazing angle of incidence, and hence the reflectivity at each interface will be quite high. Additionally, each layer acquires a Fabry-Perot character relative to the component of propagation normal to the layers. Very high reflectivities can be achieved by designing the layer thickness to coincide with the anti-resonant points of the cavity which is formed by the two interfaces of the first cladding layer. The second cladding layer also forms a similar cavity and can be designed to increase reflectivity back into the waveguide core even further. Anti-resonance is an effect used in Fabry-Perot interferometers and occurs at the point where the reflectivity of

the Fabry-Perot structure is at its maximum. An additional benefit of using anti-resonance comes from the fact that the reflectivity of the fabricated structure is insensitive to errors in film thickness. This occurs because when the resonances of a Fabry-Perot are spectrally sharp, the anti-resonances are quite broad. As one example of this effect, the ARROW radiation loss varies periodically from minimum loss to maximum loss as the thickness of the first cladding layer is increased; however, the regions of low loss are quite broad.

Higher order modes are often effectively filtered out, since mode angles of higher-order modes are farther away from grazing incidence. Thus, these modes exhibit lower reflectivities at the cladding interfaces and the anti-resonance originally designed for the fundamental mode is no longer optimal for higher-order modes. These waveguides have already found limited application in the laser field [44], in III-V optoelectronics [45-48], and in components such as polarizers [49], demultiplexers [50], and remotely-controlled couplers [51]. For further details, the reader is referred to the literature [44-68]. Additional discussion on design considerations and coupling characteristics of these waveguides can be found in Chapter 2.

1.3 Device concept

In this work, an ARROW-waveguide-based sensor is built to address the following fundamental questions:

1) Is evanescent loss a suitable mechanism for sensor design?
2) Can fiber-to-waveguide coupling be improved by using the ARROW structure?
3) Can the behavior of such a sensor be predicted by theoretical and numerical simulation methods?

As described in further detail below, this device will sense the movement of a microfabricated silicon diaphragm in response to pressure. Small changes in the position of this diaphragm relative to the optical waveguide will change the rate of optical leakage from the waveguide. Thus, intensity variations at the sensor output can be related to applied pressure. The approach of this work involves initial theoretical and numerical modelling to aide in device design. Prototype devices are then fabricated and tested experimentally to validate the models.

There are a few additional design considerations which should be mentioned. First, the general design philosophy takes advantage of the inherent strengths of optical sensing methods in adverse environments by using only optical components in close proximity to the sensing region. Light is coupled to the detection and signal processing electronics through a fiber-optic link. Second, ultimately an ultra-thin device is desired, which will measure the pressure applied across its body without introducing a significant perturbation to the system. Although the device design reported here is 600 μm in thickness, the concepts involved may ultimately be downscaled to devices with thicknesses on the order of 100 μm. The multi-layer waveguide concepts involved may potentially be applied to sheet polymeric films as well.

An exploded schematic of the original concept for a fully packaged device can be seen in Fig. 2. The package is designed so that single-mode optical fiber can be used to couple light from a helium-neon laser (λ = 6328 Å) to an integrated optical chip. In this conception, fiber alignment V-grooves have been designed to allow alignment of the fibers to the waveguide end-faces, which are to be exposed upon removal of detachable silicon parts. The figure shows these parts already removed, thus exposing the waveguide end-faces. The waveguide on the chip travels from input to output and through the active sensing area. Output light from the chip is then coupled out through a similar fiber to a

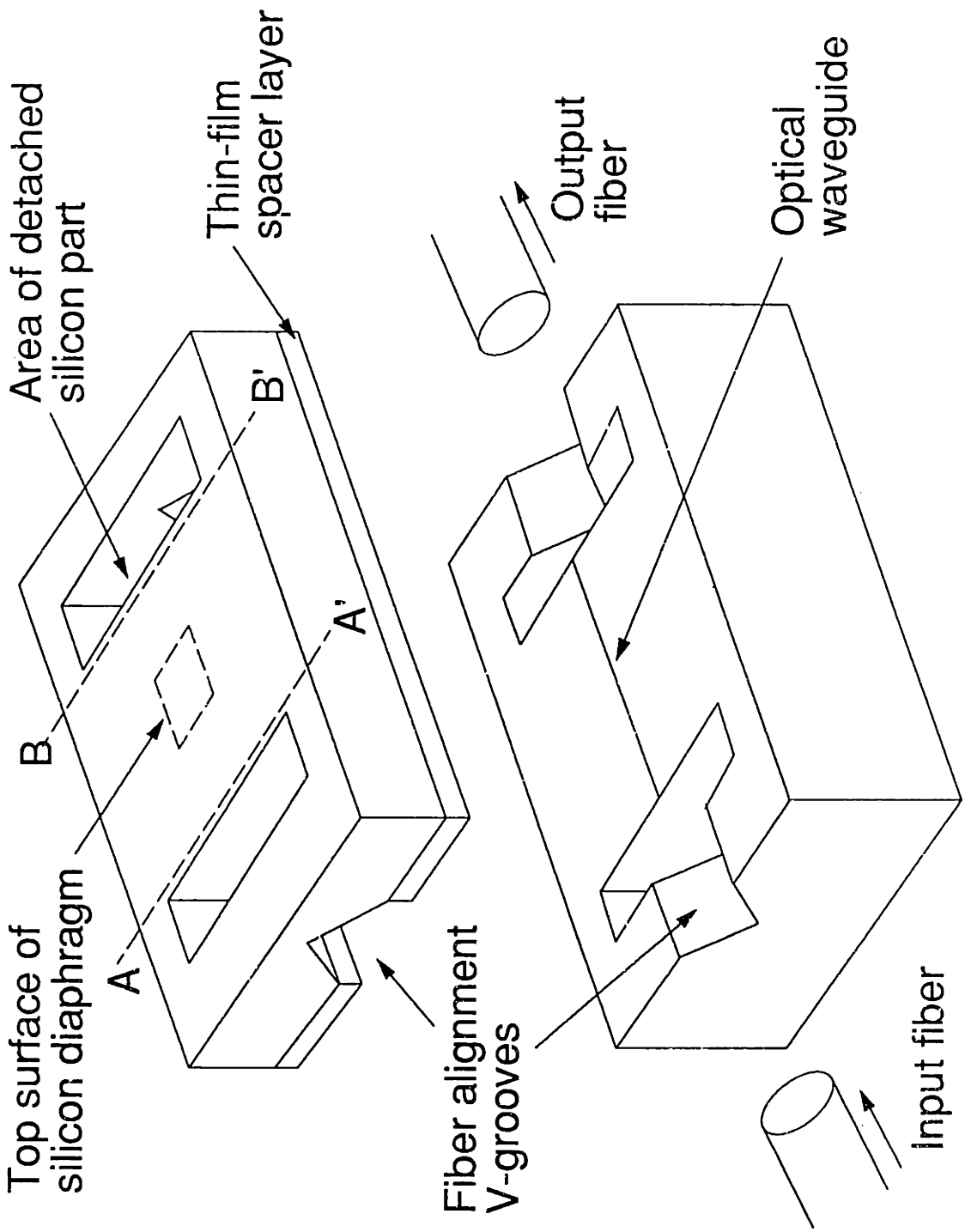

Fig. 2 Exploded schematic of ARROW-waveguide-based silicon pressure transducer

photodetector. The actual sensor package reported in Chapter Five is similar to the original concept shown in Fig. 2, but was fabricated without the set of provisions used to mount the fibers relative to the waveguide end-faces. Instead, input coupling was achieved by exposing and polishing the waveguide at the A-A' plane and by end-firing a bare laser beam into the waveguide end-face with the use of a microscope objective. Output light was similarly coupled to a calibrated photodetector and a CCD-based frame grabber by using another microscope objective to observe the exposed B-B' plane. Other details of the package remained uncompromised.

A cross-sectional schematic of the packaged device along the waveguide axis can be seen in Fig. 3. The edges of a deformable silicon diaphragm are clamped a fixed distance away from the optical waveguide. When pressure is applied to the diaphragm, the diaphragm deflects into closer proximity with the waveguide. Since silicon has a higher refractive index than the materials which make up the waveguide, leakage from the waveguide is enhanced as pressure is increased. In this way, pressure can be measured by detecting the amount of light that remains in the optical waveguide after deformation of the silicon diaphragm. The leakage coupling to the silicon diaphragm is evanescent in nature and therefore the degree of loss experienced by the waveguide is extremely sensitive to the gap spacing between the two structures. For adequate sensitivity of such a device, the gap spacing must be made extremely small. At the same time, the gap spacing must be well controlled for reproducibility of sensor response. The device discussed in this thesis solves these problems through the microfabrication of a thin-film spacer layer between the optical waveguide and the silicon diaphragm light attenuator. Prior to the bonding of the two parts, a hole of desired dimensions is made in the spacer layer to allow the silicon diaphragm room to deflect. By scaling the dimensions of the patterned hole in the spacer

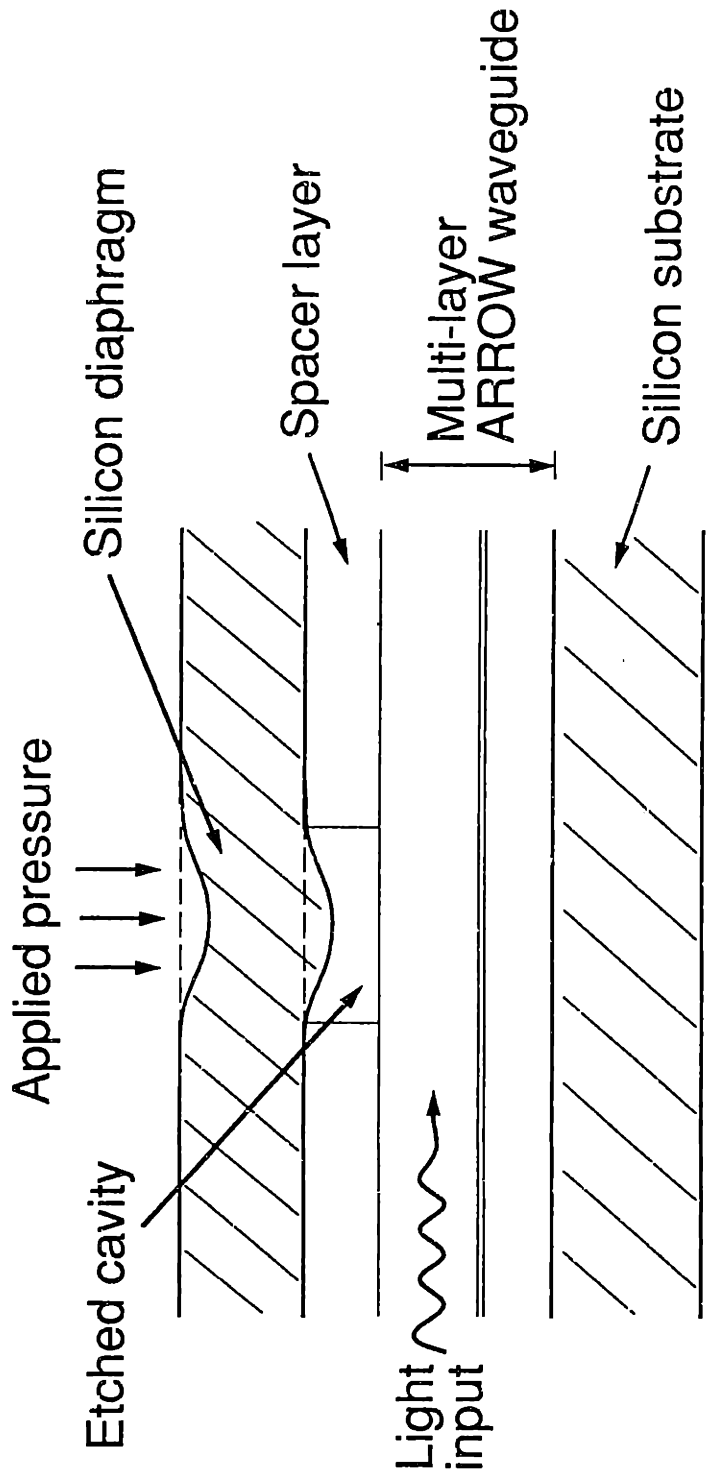

Fig. 3 Cross-sectional schematic of active sensor area

layer or the thickness of the silicon diaphragm, one can scale the range of operation of the transducer as well.

The fabrication concept for the device is shown in Fig. 4. The packaged sensor is formed through the bonding of two separate wafers. One wafer supports the ARROW waveguide and will be referred to as the "waveguide wafer". The other wafer forms the microfabricated gap spacer as well as the diaphragm itself; this wafer is referred to as the "diaphragm wafer". These wafers are then bonded together using an electrostatic bonding process followed by a high-temperature anneal to form the final structure. After bonding, the diaphragm thickness can then be adjusted by conventional lapping techniques.

1.4 Organization of Thesis

In order to fabricate useful devices, it is necessary to understand relevant behavior well enough to design appropriate structures. To accomplish this goal, studies of the properties of the ARROW waveguide were undertaken and are reported in Chapters Two and Three. Chapter Two describes theoretical modelling work performed to understand the ARROW waveguide and its advantages, as well as a number of analytical perspectives towards understanding the interaction of the diaphragm with the optical waveguides. Chapter Three reports on a number of numerical simulation studies on device properties. The simulated effects of gap spacing and attenuator index on the diaphragm-waveguide interaction was analyzed by a two-dimensional beam propagation method. The complete sensor structure response was modelled using these results. Three-dimensional effects due to ridge-etching were later analyzed using an eigen-solver technique. This chapter also includes results from beam propagation simulations on optical coupling issues and

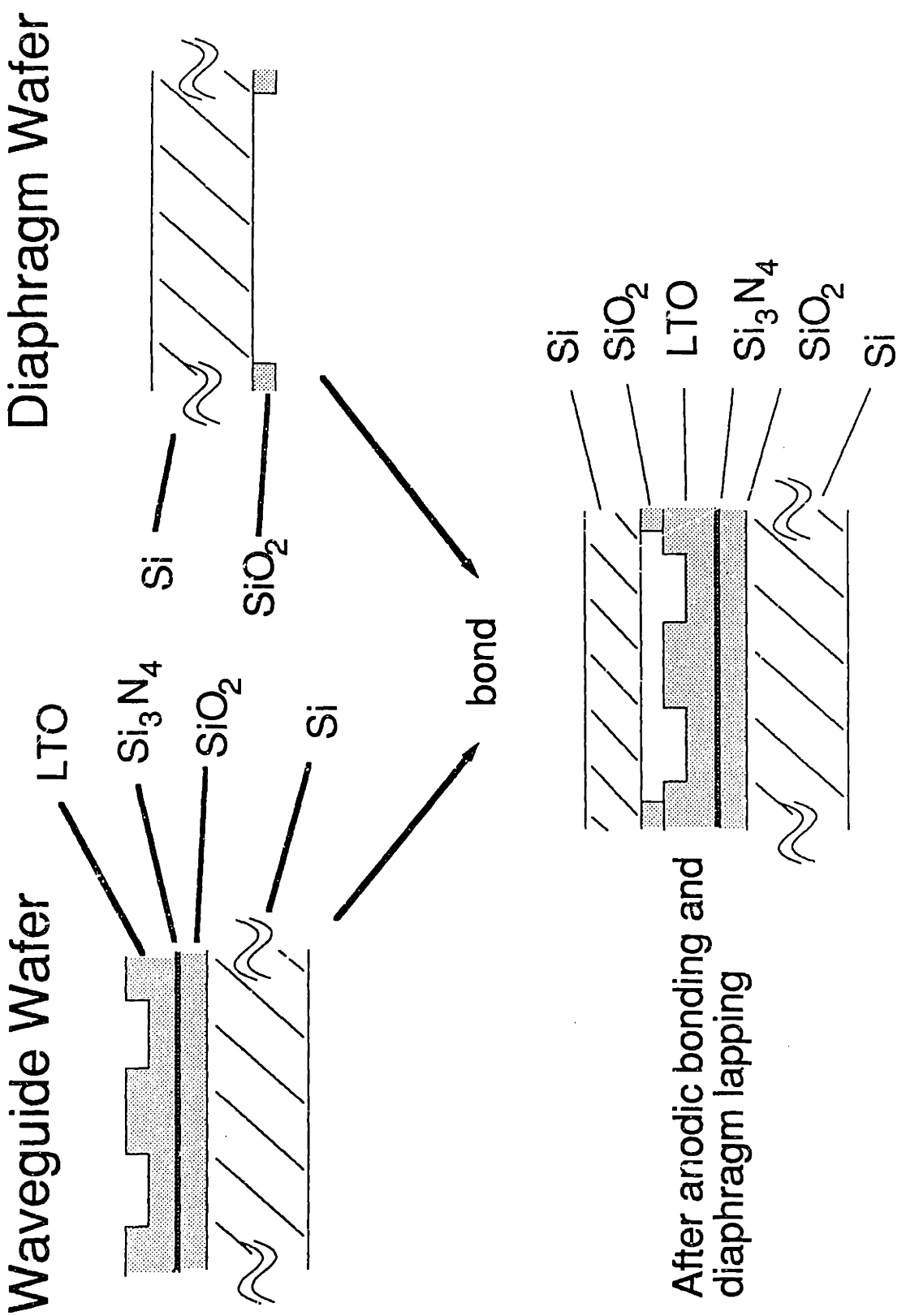

Fig. 4 Cross-sectional schematics of fabrication process

longitudinal beam stability after launch. The act of microfabricating the device led to the development of various processes including direct wafer bonding for appropriate surface materials, anisotropic sidewall etching to achieve lateral confinement, and infrared alignment schemes for use with wafer-to-wafer electrostatic bonding. These and other fabrication issues are addressed in Chapter Four. During testing, it was found that process-dependent particulates significantly affected sensor response. This effect was significant enough to force a change in the method of test from hydrostatic loading from a compressed air source to piezoelectric stack actuation to drive the diaphragm into deflection. Chapter Five reports on these testing procedures and results obtained in the characterization of the sensor. Finally, conclusions and directions for future research are presented in Chapter Six.

Chapter 2

Theoretical Modelling

2.1 Fundamental Design Considerations for the ARROW Structure

In this section, an ARROW waveguide design is presented for operation at helium-neon wavelengths (λ = 6328 Å). Interaction with the attenuator is temporarily ignored; the focus in this section is on the ARROW waveguide itself. Fundamentals of ARROW slab waveguide design have been described in the literature [44-68]. A typical ARROW structure is shown for reference in Fig. 5. The propagation behavior of this structure is treated first. It is understood that the basic principle of operation involves the propagation of light at near grazing incidence between two planes. Light is confined at the top interface due to total internal reflection, and at the bottom interface due to very high reflectivity caused by a combination of grazing angle and Fabry-Perot effects. A ν-th order quasi-mode is said to be supported when the phase matching condition is satisfied, i.e.:

$$2k_o n_c d_c \sin\theta_\nu + \phi_1 + \phi_2 = 2\nu\pi$$

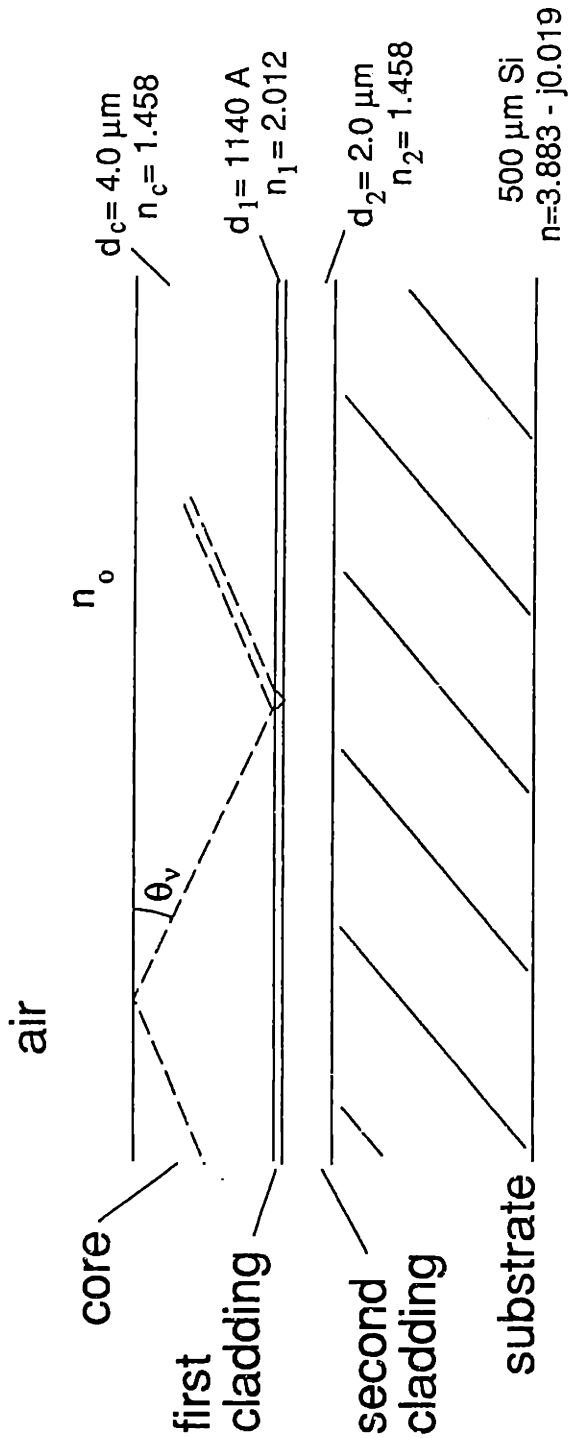

Fig. 5 Typical ARROW structure cross-section

where ϕ_1 and ϕ_2 are the phase-shifts seen at the core-air and core-cladding interfaces respectively, k_0 is the free-space wavenumber, n_c and d_c are the core index and core thickness respectively, and θ_ν is the propagation angle of the light. The propagation constant and the propagation loss can be defined as:

$$\beta_\nu = k_0 n_c \cos\theta_\nu$$

and

$$L_\nu = -5 \tan\theta_\nu \log(R_\nu)/d_{ce} \qquad \text{(dB/cm)}$$

respectively, where the effective core thickness, d_{ce}, can be written as:

$$d_{ce} = d_c + \frac{\lambda}{2\pi\sqrt{n_c^2 - n_o^2}}$$

for the TE mode, and where R_ν represents the power reflectivity of the two-layer cladding for the ν-th order mode. If $R_\nu \cong 1$, then this expression for loss can be approximated as:

$$L_\nu = 2.17(1 - R_\nu) \tan\theta_\nu / d_{ce} \qquad \text{(dB/cm)}$$

Using a ray-optics approach, this expression can be easily understood as the effect of the transmittance loss the light experiences at each bounce at the leaky core-cladding interface multiplied by the number of bounces the quasi-mode experiences per length. This expression also makes clear the mode filtering properties of the ARROW waveguide, since higher order modes will experience much higher degrees of loss than the fundamental mode.

In the following paragraphs, basic design considerations involved in creating ARROW waveguiding structures are considered. When designing a conventional ARROW waveguide, one is interested in building a structure that will propagate the fundamental mode with high efficiency and take advantage of the possibility for good index and spatial matching to optical fibers. A fundamental choice that needs to be made is the desired effective size of the core. There are several factors that influence this decision including: the effective spot size of the optical fiber, the effect of layer thicknesses on the costs of fabrication, and the effect of core thickness on the propagation loss of the waveguiding structure.

In order to achieve high coupling efficiency, it is desirable to design a structure with a guiding layer thickness comparable to the 1/e diameter of optical fiber, which is determined by the points where the E-field strength drops to 1/e of its maximum value. It will be shown that this type of structure can provide low propagation losses as well. The requirements for single-mode operation at helium-neon wavelengths (λ = 6328 Å) are considered here. For most commercial optical fibers, the V-number, V=2. A standard empirically curve-fitted expression for 1/e width is [69]:

$$w \approx d\left(0.65 + \frac{1.619}{V^{1.5}} + \frac{2.879}{V^{6}}\right)$$

This expression has been used in the optical fiber field for over a decade and is generally considered accurate to about 1%. Thus for a conventional optical fiber with diameter d=4 μm, the effective modal width is w=5.07 μm.

As an aside, this result is now compared to that obtained for a standard asymmetric waveguide formed by depositing a silicon nitride core over a thick silicon dioxide layer, with air acting as the top layer in the structure. The silicon nitride guiding layer (n=2.012),

which was chosen for compatibility with conventional integrated circuit processing, is highly mismatched with respect to silicon dioxide (n=1.458). Hence, the waveguide mode supported by the silicon nitride film will be very tightly confined to the core region. A brief calculation shows that the greatest thickness of silicon nitride allowable for single-mode operation of this type of waveguide is approximately 0.27 μm. When accounting for beam propagation in the surrounding media, this corresponds to an effective width of 0.4 μm, which is much smaller than optical fiber modal dimensions. Since coupling efficiencies can be approximated by the overlap integral between the input wavefunction and the eigenmodes of the waveguiding structure, it is clear to see that these types of standard waveguides are poor candidates for coupling to single-mode optical fibers. Although this problem can be alleviated somewhat by lowering the index mismatch between core and buffer layer, such a solution is inherently coupled to a corresponding increase in the buffer layer thickness, which is often impractical for cost reasons.

Returning to the selection of waveguide core thickness, designing the effective core width to be as close as possible to the 5 μm fiber mode width is desirable for enhanced coupling efficiency. However, after taking into account the cost of fabricating the entire ARROW structure, a 4 μm core thickness was selected, since fabrication of the appropriate cladding layers for a full 5 μm core would be prohibitively costly. Solving for loss minimization for fundamental mode operation, the cladding thicknesses must satisfy:

$$d_1 \approx \frac{\lambda}{4n_1}\left\{1-\left(\frac{n_c}{n_1}\right)^2+\left(\frac{\lambda}{4n_1 d_{ce}}\right)^2\right\}^{-\frac{1}{2}}(2N+1) \qquad N=0,1,2,\ldots$$

and

$$d_2 \approx \frac{d_{ce}}{2}(2M+1) \qquad M=0,1,2,\ldots$$

For the 4 μm core selected, this results in a first-cladding-layer silicon nitride thickness of 1140 Å and a second-cladding-layer silicon dioxide thickness of 2.0 μm. Calculations using this geometry give an inherent power reflectivity of 0.9997 for the two-layer cladding and a waveguide loss of 0.09 dB/cm, which corresponds to radiation loss to the silicon substrate below. Thus this design shows promise for low loss propagation of the fundamental mode and the potential for efficient coupling to optical fibers. In the following section, formulas are derived which allow a quantitative analysis of coupling improvements.

2.2 Comparison of ARROW and Standard Waveguides

An advantage in fiber coupling is expected due to the better spatial and index matching properties of the ARROW waveguide as illustrated schematically in Fig. 6. In this section, formulas are derived to make this improvement quantitative. The issue of primary concern is that of alignment. This problem is approached with the use of overlap integral formalism. Reflectivity effects from the waveguide end-faces are neglected in this analysis, since they are relatively small (~8-12% additional loss with air in the intermediary region) and can be further reduced with the use of index-matching epoxy in the final device structure. The results are presented for the three cases of misalignment shown in Fig. 7: transverse, angular, and longitudinal. The effects of these three misalignments are analyzed for the cases where the modes of the launching and receiving waveguides are represented by either "large" (w = 2.0 μm) or "small" (w = 0.2 μm) gaussian wave approximations. The small waveguide approximation is used to represent the silicon nitride

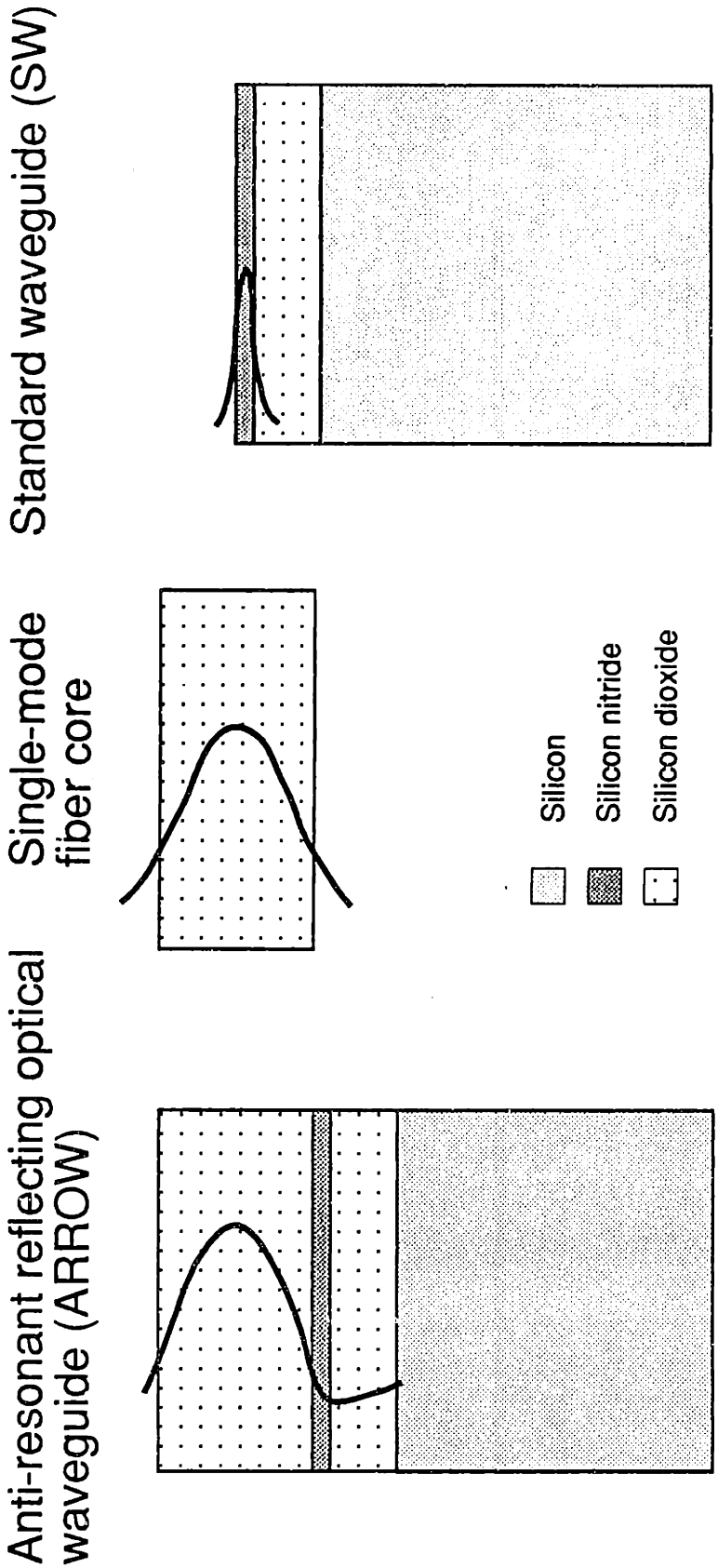

Fig. 6 ARROW and SW waveguide comparison

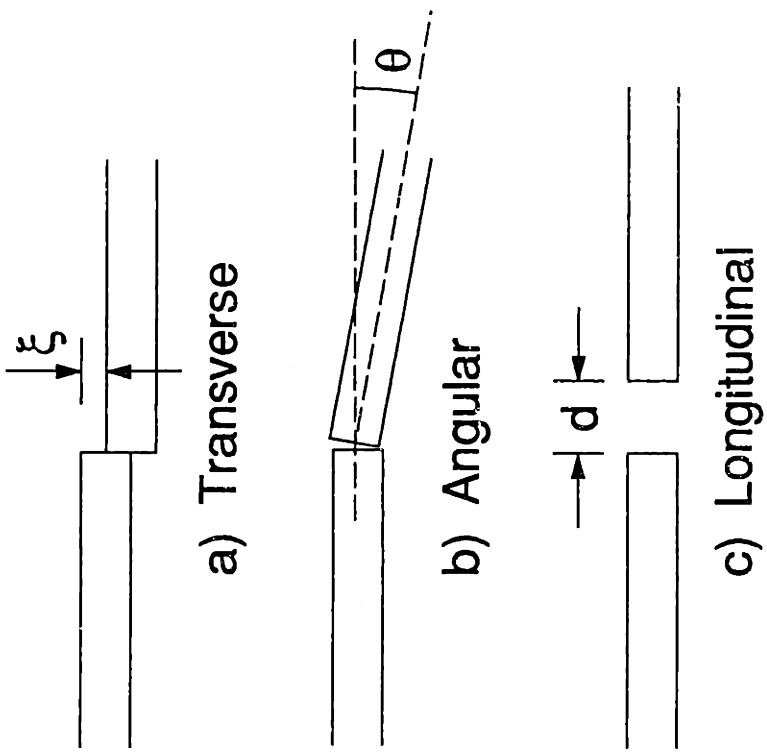

Fig. 7 Three cases of misalignment

waveguide. This approximation admittedly exaggerates insertion losses, since the actual in-plane waveguide dimension is expected to be much larger than the model suggests. However, this approximation is still useful in illustrating the effect of waveguide size on various coupling related parameters. The large waveguide approximation is used to represent both the single-mode optical fiber and the ARROW waveguide modes. Previous authors have demonstrated that improvements in transverse and longitudinal alignment tolerances can come at the expense of angular alignment tolerances [70]. It is found that the ARROW waveguide represents a good compromise and allows for successful mechanical alignment in all three aspects.

The transverse misalignment problem is anticipated to be the most severe. The closed form of the power coupling as calculated from the overlap integral is:

$$T = \left(\frac{2w_1 w_2}{w_1^2 + w_2^2}\right)^2 e^{-2\xi^2/(w_1^2+w_2^2)}$$

where w_1 and w_2 are the 1/e radii of the launching and receiving waveguides respectively, and ξ is the transverse misalignment. From this formula, it can be seen that the maximum transmitted power is:

$$T_{\max} = \left(\frac{2w_1 w_2}{w_1^2 + w_2^2}\right)^2$$

If $w_1 = w_2$, then this expression is reduced to unity, as expected. The half-width for where the power drops to 1/e of its maximum value can also be found from the power coupling formula:

$$\xi_e = \sqrt{\frac{w_1^2 + w_2^2}{2}}$$

Numerical calculations from these expressions show that a fiber with w = 2.0 μm would be expected to couple with near unity efficiency to an ARROW waveguide, whereas coupling to a standard silicon nitride waveguide would show an efficiency of only 0.04, a loss of 14 dB.

If the overlap integral formalism is applied to the problem of angular misalignment, the transmitted power becomes:

$$T = \left(\frac{2w_1w_2}{w_1^2 + w_2^2}\right)^2 \exp\left[-\frac{k_o^2 w_1^2 w_2^2 \sin^2\theta}{2\left(w_2^2\cos^2\theta + w_1^2\right)}\right]$$

where θ is the angular misalignment. If θ is small, this expression reduces to:

$$T = \left(\frac{2w_1w_2}{w_1^2 + w_2^2}\right)^2 \exp\left[-\frac{k_o^2\theta^2 w_1^2 w_2^2}{2\left(w_1^2 + w_2^2\right)}\right]$$

This expression gives a similar result for maximum transmission, and θ_c, which is defined as the 1/e point for θ, can be written as:

$$\theta_e = \frac{\sqrt{2\left(w_1^2 + w_2^2\right)}}{k_o w_1 w_2}$$

Inserting reasonable numerical values for w_1 and w_2 shows that angular misalignment is not truly a limiting factor in device design, since these angular tolerances are easily satisfied.

Finally, the effect of longitudinal error is analyzed by performing the overlap integral between two gaussians, where one has been allowed to propagate over a distance, d. The following result is obtained for transmitted power:

$$T = \frac{4}{w_1^2 w_2^2 \left[1 + \left(\frac{d}{p}\right)^2\right]} \frac{1}{\left(\frac{1}{w_1^2\left[1+\left(\frac{d}{p}\right)^2\right]} + \frac{1}{w_2^2}\right)^2 + \left(\frac{kd/2}{d^2+p^2}\right)^2}$$

where d is the separation distance, $p = (\pi w_1^2)/\lambda$, and w_1 and w_2 are the beam radii at the end-faces of the launching and receiving waveguides respectively. Note that as d goes to zero, the expression reduces to the expression for maximum power obtained from the transverse misalignment formula.

For the case where w_1 and w_2 are equal, the above formula reduces to:

$$T = \frac{1 + 4\Omega^2}{(1 + 2\Omega^2)^2 + \Omega^2}$$

where

$$\Omega = \frac{d\lambda}{2\pi w^2}$$

If this is the case, then the value of d that corresponds to half-maximum is simply:

$$d = \frac{2\pi w^2}{\lambda}$$

For large waveguides, this gives an axial tolerance of 40 μm. For small waveguides, this gives an axial tolerance of 0.4 μm. As expected, the fiber-to-ARROW coupling shows more longitudinal tolerance than coupling between two silicon nitride waveguides. However, a more interesting problem may be to determine the behavior of coupling from large-to-small and small-to-large waveguides. Transmitted power as a function of separation distance is plotted in Fig. 8 for large-to-small and small-to-large coupling. The $w_1 = w_2$ cases are also shown for reference. It can be seen that a large-to-small coupling has very low efficiency at d=0, and decreases monotonically with distance. The small-to-

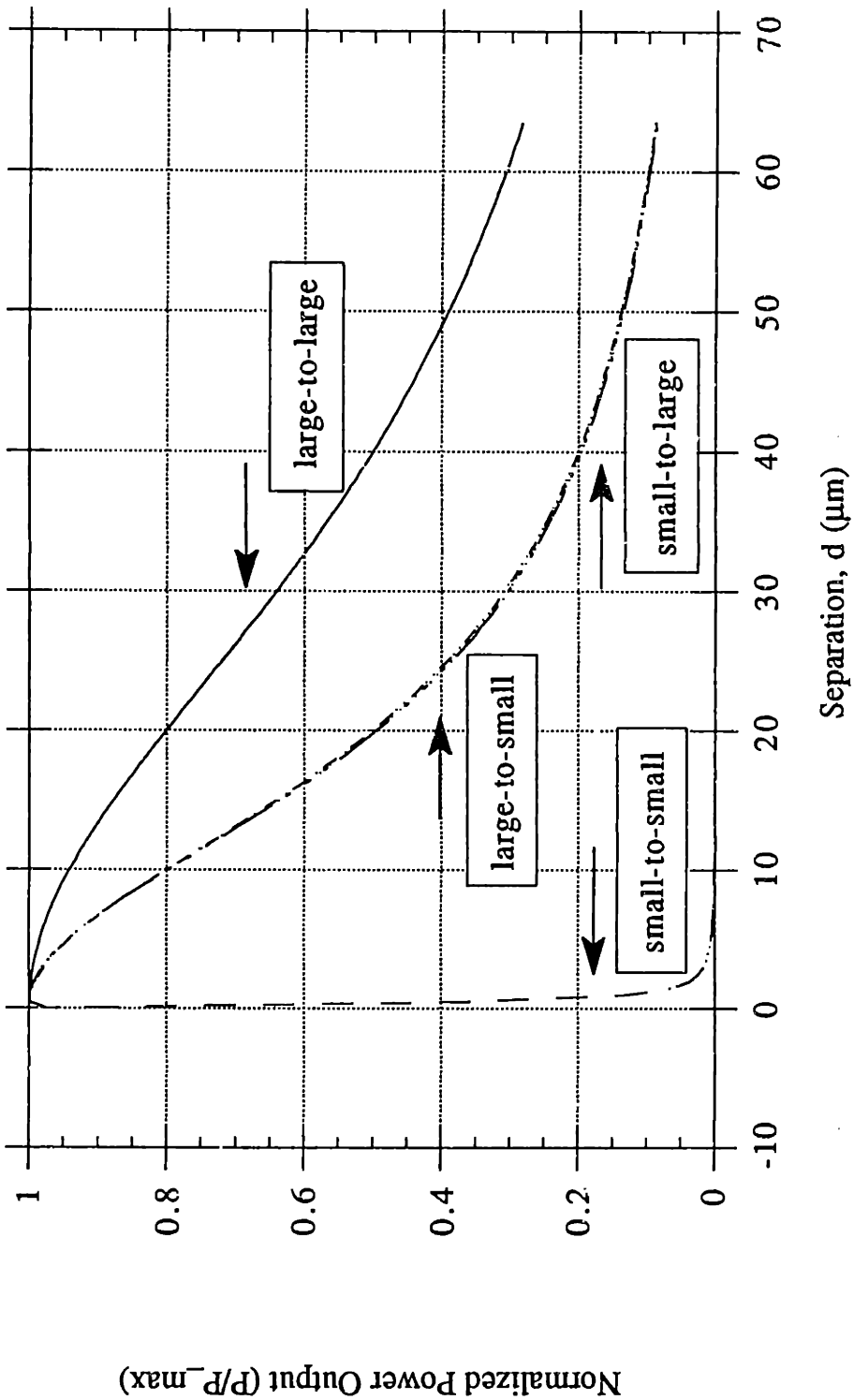

Fig. 8 Transmitted power as a function of separation distance for different coupling arrangements

Waveguide sizes	ξ_e (μm)	θ_e (rad)	$d_{1/2}$ (μm)	T_{max}
large-to-large	2	0.1	40	1
small-to-small	0.2	0.96	0.4	1
large-to-small	1.4	0.80	20	0.04
small-to-large	1.4	0.62	20	0.04

Table 1. Effect of waveguide sizes on coupling parameters

large coupling has the same low value for coupling efficiency at d=0. However, as d is increased, the coupling briefly increases slightly (~2%) before decreasing monotonically. This increase is expected, since the smaller mode should increase in size to more closely match the mode shape of the larger mode. However, apparently the curvature of the beam has a strong adverse effect, since at no point does the transmitted power approach unity. In fact, the results for large-to-small and small-to-large coupling are nearly identical. The half-width half-maximum of large-to-small coupling and small-to-large coupling are both about 20 μm, a factor of 2 worse than the result for large-to-large coupling. Thus, fiber input and output coupling through standard waveguides will result in very high loss (-28 dB) with reduced alignment tolerances at both the input and output. It should be pointed

out that neither of these deficiencies is catastrophic. Collection end tolerances may be improved somewhat by switching to multimode fiber collection. Also, the 28 dB loss is certainly endurable for the case of a single sensor, although configurations of multiple sensors would appear difficult to implement. However, if these deficiencies are undesirable, they can be improved upon by simply converting to the ARROW structure.

A summary of results is shown in Table 1. Important observations are: 1) large-to-large coupling shows the most tolerance to transverse misalignment. However, the corresponding large-to-small and small-to-large tolerances are not far off, 2) large-to-large couplings have the worst angular tolerance figures, but as stated before, even these are still easily satisfied, 3) large-to-large coupling shows a factor of 2 improvement in longitudinal alignment tolerances over either large-to-small or small-to-large coupling, and finally 4) where the large-to-large coupling has its greatest advantage is in its unity maximum transmitted power. It is the only combination which offers high power transmission as well as reasonable alignment tolerances.

Therefore, the advantages of coupling from a single-mode fiber into an ARROW waveguide are: 1) somewhat better transverse alignment tolerances, 2) improved longitudinal alignment tolerances, and 3) improved coupling efficiency. In addition to these coupling advantages, the ARROW has another potential advantage over silicon nitride waveguides that bears directly on evanescent sensors. Since the ARROW core is a relatively low index material, it is expected that the mode supported will extend further into the air space above the core, thus making it more readily accessible for interaction with a light attenuator. The task at hand now becomes looking for a way to calculate the amount of leakage from the top surface of the waveguide which is introduced through interaction with the deformable silicon diaphragm.

2.3 Theoretical Calculation of Leakage Enhancement

This section describes methods used in the calculation of leakage induced by the proximity of a silicon diaphragm attenuator to a light carrying optical waveguide. Initially, a normalization factor analysis is described which predicts the behavior of the device in regions where the attenuator is not in extreme proximity to the waveguide. Obviously such a model is of limited usefulness in predicting device response, since some of the most interesting phenomona will occur when the attenuator is closest to the waveguide. The behavior of the state where the gap is reduced to zero is studied with the use of leaky-mode formulas derived for a three-layer model. However, this model does not incorporate gap dependence so it can only be used in a fashion which complements the normalization factor analysis results. A more comprehensive model is introduced using a transmittance method calculation which can be derived either from Airy summation of ray-optic results or from matrix method calculations.

2.3.1 Normalization Factor Analysis

Normalization factor analysis was initially used by Ulrich to model prism coupling to thin-films [71]. However, this technique is applicable to other types of leaky wave behavior as well. Here, the analysis is used to determine how the degree of leakage from a thin-film structure to a silicon attenuator depends on the gap spacing between the two components. This section is based on a treatment by Ghatak [70, 72-75]. However, to apply this method to the ARROW waveguide structure, Ghatak's treatment is extended to asymmetric structures.

2.3.1.a. Leaky Fields Model

Analysis of the ARROW structure by Jiang, et.al. [59] using transmission-line methods has shown that a very good approximation to the behavior of the ARROW waveguide can be achieved by simply modelling the region below the core as a perfect conductor. This is reasonable, since much modelling work has shown that the electric field is nearly zero at the interface between the core and the first cladding.

Using this approximation, the index profile of the leaky waveguide structure is modelled as shown in Fig. 9a. Properties of the leaky guide will be derived by comparing the structure shown in Fig. 9a, which can only support leaky modes, with the corresponding guiding structure shown in Fig. 9b, where the leakage inducing component has been removed. In this section, region I represents the silicon dioxide core, region II represents the air gap, and region III represents the silicon attenuator. To solve for the TE modes of the leaky structure, $\psi(x)=E_y(x)$ must satisfy the wave equation:

$$\frac{\partial^2\psi}{\partial x^2} + k_0^2 n^2(x)\psi = 0$$

where n(x) represents the index profile shown in Fig. 9a. Thus, the solution for TE modes for $n_2 < \beta/k_0 < n_{1,3}$ is given by:

$$\begin{aligned}
\psi_{\rm I}(x) &= A\sin(\alpha_1 x) \\
\psi_{\rm II}(x) &= B\exp(\gamma(x-x_1)) + C\exp(-\gamma(x-x_1)) \\
\psi_{\rm III}(x) &= D_+\exp(i\alpha_2(x-x_2)) + D_-\exp(-i\alpha_2(x-x_2))
\end{aligned}$$

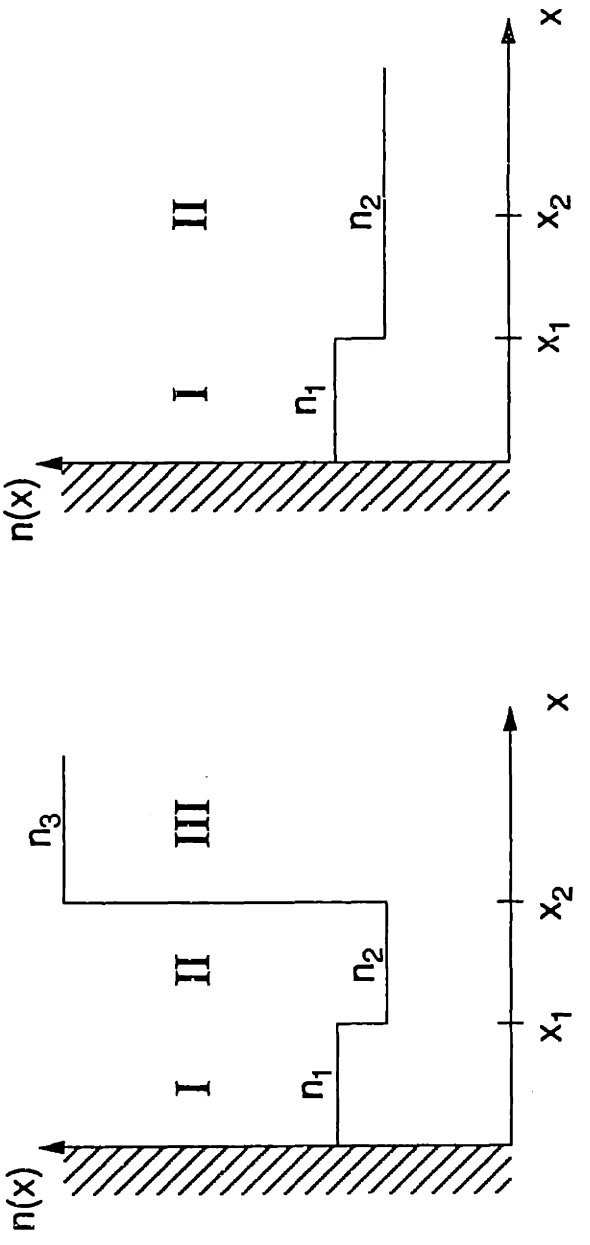

Fig. 9 Refractive index profiles for leaky and guiding waveguide structures

where:

$$\alpha_1^2 = k_o^2 n_1^2 - \beta^2$$

$$\gamma^2 = \beta^2 - k_o^2 n_2^2$$

$$\alpha_2^2 = k_o^2 n_3^2 - \beta^2$$

and β is the propagation constant. B, C, D_+, and D_- can be expressed in terms of A by applying the conditions of continuity of ψ and dψ/dx at $x=x_1$ and $x=x_2$:

$$B = \frac{1}{2}A\left(\sin(\alpha_1 x_1) + \frac{\alpha_1}{\gamma}\cos(\alpha_1 x_1)\right) \tag{2.1}$$

$$C = \frac{1}{2}A\left(\sin(\alpha_1 x_1) - \frac{\alpha_1}{\gamma}\cos(\alpha_1 x_1)\right)$$

$$D_\pm = \frac{1}{2}\left[Be^{\gamma(x_2-x_1)} + Ce^{-\gamma(x_2-x_1)} \pm \frac{\gamma}{i\alpha_2}\left(Be^{\gamma(x_2-x_1)} - Ce^{-\gamma(x_2-x_1)}\right)\right]$$

This solution is now compared with the solution for the guided wave structure shown in Fig. 9b. The guided wave solution is:

$$\psi_{\mathrm{I,g}}(x) = A_g \sin(\alpha_g x)$$

$$\psi_{\mathrm{II,g}}(x) = A_g \sin(\alpha_g x_1) e^{-\gamma(x-x_1)}$$

and it is straightforward to show that the normalization factor A_g is:

$$A_g = \sqrt{\frac{2\gamma}{1+\gamma x_1}} \tag{2.2}$$

Note that if B=0 in Eq.(2.1), then the leaky fields will resemble the guided mode case, with a small oscillatory component in region III; these fields will be called "quasi-modes".

2.3.1.b. Calculation of Waveguide Leakage

The incident wave field can be expressed as the sum of orthonormal components:

$$\psi(x,0) = \psi_g(x) = \int \phi(\beta)\psi_\beta(x)\mathrm{d}\beta$$

where $\psi\beta(x)$ represents the normalized radiation modes and $\phi(\beta)$ represents the appropriate weighting factor for each mode. Hence for $z > 0$ the wave can be written as:

$$\psi(x,z) = \int \mathrm{d}\beta\phi(\beta)\psi_\beta(x)e^{i\beta z}$$

The fractional power remaining in the core at distance z is approximately given by the overlap integral:

$$W(z) = \left|\int_0^\infty \psi^*(x,0)\psi(x,z)\mathrm{d}x\right|^2$$

Rewriting this expression as an integral over β gives:

$$W(z) = \left|\int |\phi(\beta)|^2 e^{i\beta z}\mathrm{d}\beta\right|^2 \qquad (2.3)$$

The immediate problem becomes that of solving for the magnitude of $\phi(\beta)$. Using a similar approach to Ghatak, one notes that if $(x_2 - x_1)$ is large enough, near $\beta=\beta_g$ the normalized radiation modes can be expressed as:

$$\psi_\beta(x) \approx \left(\frac{A}{A_g}\right)\psi_g(x) \tag{2.4}$$

where $\psi_g(x)$ represents the solution for the corresponding guided wave case. This assumption is based on the premise that the shape of the leaky fields in regions 1 and 2 are identical to the shape of the fields in the guided case and that the effect of region III is negligible. Both of these criteria are only satisfied if $(x_2 - x_1)$ is sufficiently large. Therefore, this model is not expected to accurately predict leakage losses when x_2 is near x_1. Since A_g has already been calculated above in Eq.(2.2), the next goal is the calculation of A. A Taylor series calculation of B and C near $\beta=\beta_g$ yields:

$$B \approx \frac{1}{2}A\frac{\beta_g\delta_1}{\gamma^2\alpha_1}(1+\gamma_g x_1)(\beta-\beta_g)$$

$$C \approx \frac{A}{\delta_1}\alpha_1$$

where we define:

$$\delta_i^2 = \gamma^2 + \alpha_i^2 \qquad (i=1,2)$$

Substitution of these results gives an expression for the magnitude of D_+ and D_- in terms of A:

$$|D_{\pm}| \approx \frac{1}{4}|A|\frac{\delta_1\beta}{\gamma^2\alpha_1}(1+\gamma x_1)\left|1+\frac{\gamma}{i\alpha_2}\right| e^{\gamma(x_2-x_1)}$$

$$* \left|(\beta-\beta_g)+\frac{2\gamma^2\alpha_1^2}{\beta^2\delta_1^2(1+\gamma x_1)}\frac{1-(\gamma/i\alpha_2)}{1+(\gamma/i\alpha_2)}e^{-2\gamma(x_2-x_1)}\right|$$

However, this result can easily be compared with the fact that orthonormality of modes implies that:

$$|D_{\pm}| = \sqrt{\frac{\beta}{2\pi\alpha_2}}$$

Thus, solving for the magnitude squared of A gives:

$$|A|^2 = \frac{\frac{\beta}{2\pi\alpha_2}\frac{16\alpha_1^2\gamma^4}{\beta^2\delta_1^2}\frac{1}{(1+\gamma x_1)^2}\frac{\alpha_2^2}{\alpha_2^2+\gamma^2}e^{-2\gamma(x_2-x_1)}}{\left((\beta-\beta_g')^2+\Gamma^2\right)} \tag{2.5}$$

Substitution of Eqs. (2.2) and (2.5) into (2.4) gives:

$$|\phi(\beta)|^2 = \left|\frac{A}{A_g}\right|^2 \approx \frac{\Gamma}{\pi}\frac{1}{(\beta-\beta_g')^2+\Gamma^2} \tag{2.6}$$

where:

$$\Gamma = \frac{4\alpha_1^2\gamma^3\alpha_2}{\beta\delta_1^2\delta_2^2}\left(\frac{1}{1+\gamma x_1}\right)e^{-2\gamma(x_2-x_1)}$$

and

$$\beta_g' = \beta_g + \frac{\Gamma(\alpha_2^2-\gamma^2)}{2\alpha_2\gamma}$$

Further substitution of Eq. (2.6) into (2.3) gives:

$$W(z) \approx \left| \frac{\Gamma}{\pi} \int \frac{e^{i\beta z} d\beta}{(\beta - \beta_g')^2 + \Gamma^2} \right|^2$$

Solving for the power using complex analysis gives a simplified result:

$$W(z) \approx \left| \frac{\Gamma}{\pi} 2\pi i \frac{e^{-\Gamma z}}{2i\Gamma} \right|^2 = e^{-2\Gamma z}$$

The power loss in dB/cm is:

$$L = -10 \log \frac{W(z = 1\text{cm})}{W(z = 0)} \approx 87000\Gamma \qquad (\text{dB/cm})$$

which for the case of the fundamental mode of our ARROW waveguides can be expressed as:

$$L = 92e^{-21(x_2 - x_1)}$$

This expression is plotted in Fig. 10 and will be compared to the results obtained from numerical simulations. It is important to note that the loss, already expressed in dB/cm, shows an exponential decrease with increasing gap spacing. It is also important to bear in mind that it has been one of the major assumptions in this derivation that the gap spacing was not so small that the waveforms were distorted significantly from the unperturbed guiding waveguide case. Thus, the loss predicted for zero gap spacing using this model (92 dB/cm) is not expected to be accurate. However, it is anticipated that understanding the

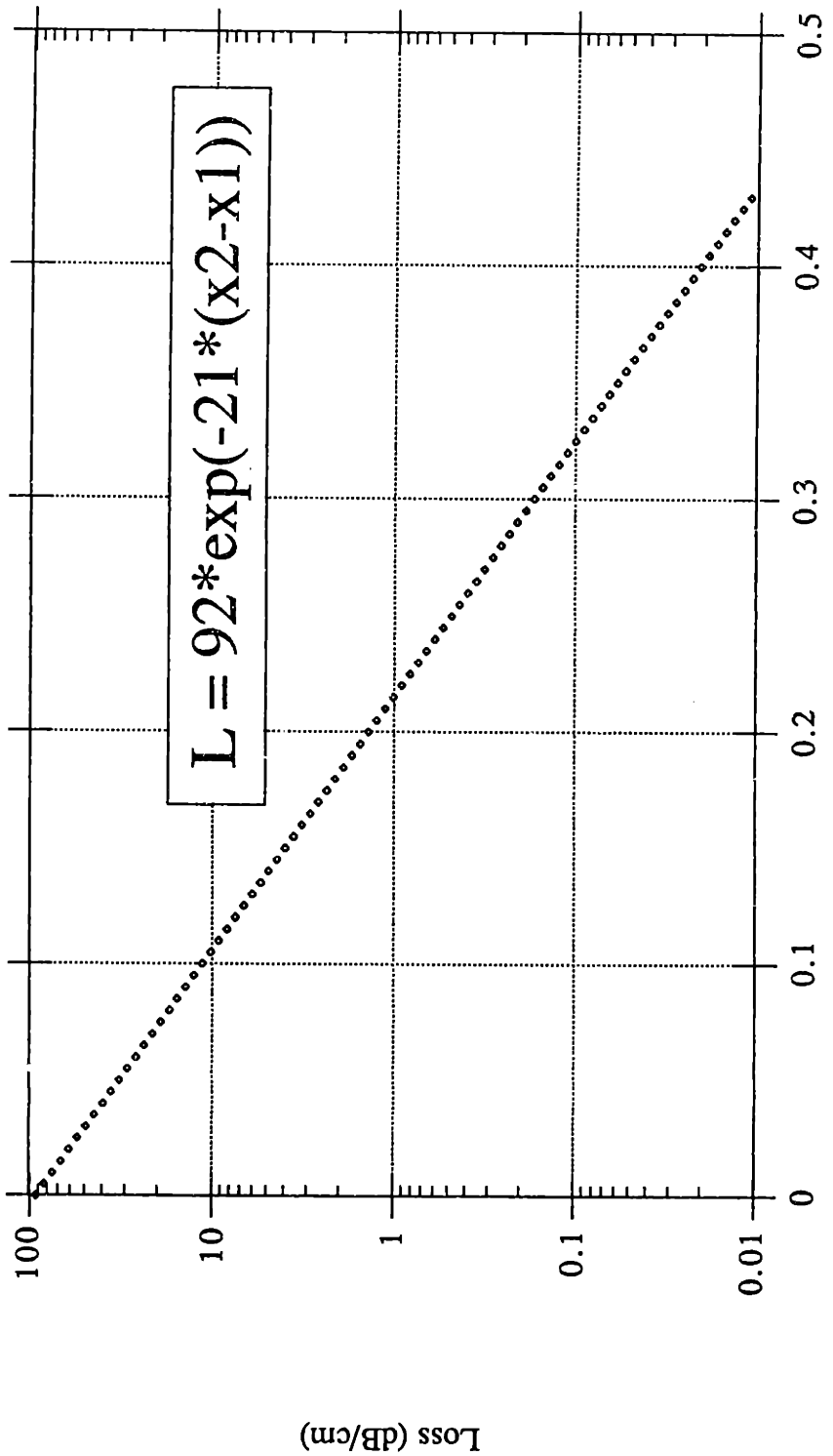

Fig. 10 Predicted loss from normalization factor analysis

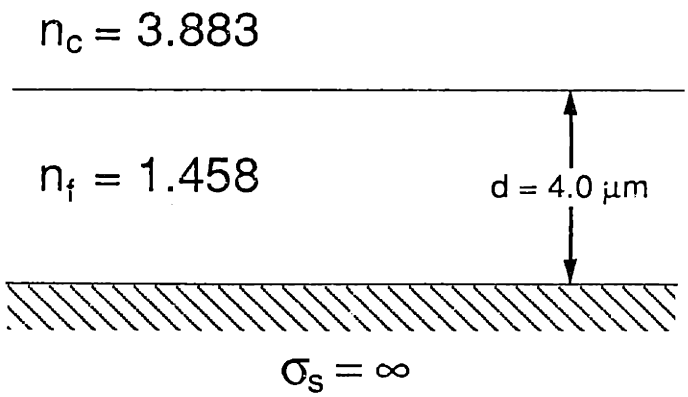

Fig. 11 Model for three-layer formulas

interaction near zero gap spacing will be very important to device modelling. Hence we turn our attention to another technique to attempt to determine the loss in this regime.

2.3.2 Three-Layer Leaky Mode Formulas

One can predict what occurs at zero gap spacing by studying the problem illustrated in Fig. 11. Here the cladding layers have been replaced by a perfectly conducting plane and the air gap has been completely removed. These simplifications make it simple to implement the three-layer formulas reported by Haus and Miller [76]. It is assumed that the magnitude of the reflection coefficient for the bottom interface is unity and that of the top surface is very close to unity. This allows us to describe the power attenuation rate for the fundamental TE mode as:

$$2\alpha = \frac{\lambda^2}{2d^2 n_f^2}\left[\frac{n_f}{n_c}\frac{1}{\sqrt{1-\left(\frac{n_f}{n_c}\right)^2}}\right]$$

which corresponds to the expression reported by Hall and Yeh [77] in their work on leaky waves in heteroepitaxial films. Inserting the appropriate values for the simplified device structure gives a loss of 25.9 dB/cm at zero gap spacing. This calculation is good for zero gap spacing, but it does not take into account the effect of the air gap spacing on power attenuation loss. In order to incorporate this effect, a transmittance method calculation was developed.

2.3.3 Transmittance Method Calculation

The analysis of this section presumes that the light within the waveguide core can be modelled by a ray-optic approach. Leakage due to attenuation is determined by first calculating the transmittance that occurs each time a ray impinges on the core-air interface, and then multiplying this effect by the number of individual losses, which is determined by the angle of incidence of the light in the core. There are two approaches that lead to the same basic result described below. The first is achieved by using an Airy summation in a ray-tracing method across the air gap. The second involves using a matrix method calculation to arrive at the same expression for the transmission coefficient, and hence transmittance. This idea can be summarized mathematically in the following expressions for transmittance and loss:

$$T = \frac{n_3 \cos\theta_3}{n_1 \cos\theta_1} |t|^2$$

$$L = 2.17T \tan\theta / d_{ce} \qquad (2.7)$$

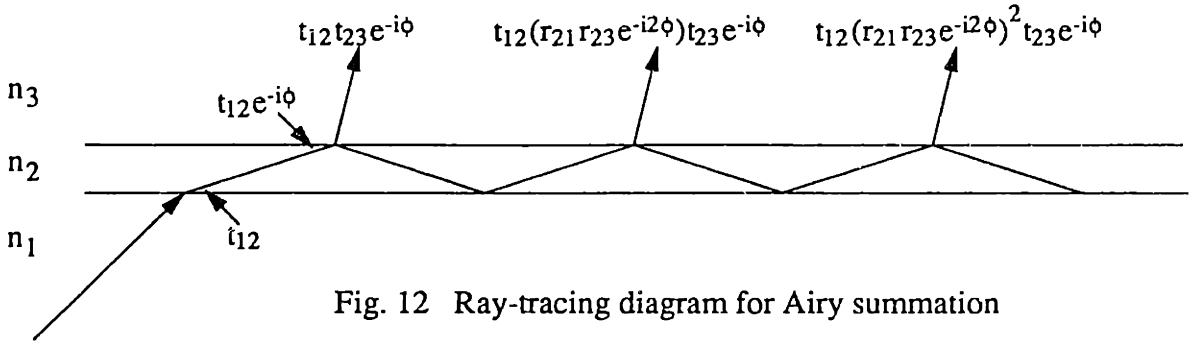

Fig. 12 Ray-tracing diagram for Airy summation

The goal of these approaches is to calculate the transmission coefficient, t, which can be used to calculate the transmittance, T, and hence the loss of the structure. It is found that for d > 0.2 μm, these techniques give similar results to the normalization factor analysis. However, for d < 0.2 μm, the results tend toward the three-layer calculation presented in Section 2.3.2.

2.3.3.a Airy Summation of Ray-Tracing Results

A ray tracing diagram for the system of interest is shown in Fig. 12. By performing an Airy summation of rays that are transmitted across the air gap, the transmission coefficient is given by:

$$t = t_{12}t_{23}e^{-i\phi}\left[1 + r_{23}r_{21}e^{-2i\phi} + (r_{23}r_{21}e^{-2i\phi})^2 + \cdots\right]$$

which can be reduced to:

$$t = \frac{t_{12}t_{23}e^{-i\phi}}{1 + r_{12}r_{23}e^{-2i\phi}}$$

where

$$t_{12} = \frac{2k_{1x}}{k_{1x} + k_{2x}} \qquad r_{12} = \frac{k_{1x} - k_{2x}}{k_{1x} + k_{2x}}$$

$$t_{23} = \frac{2k_{2x}}{k_{2x} + k_{3x}} \qquad r_{23} = \frac{k_{2x} - k_{3x}}{k_{2x} + k_{3x}}$$

for TE waves, and

$$k_{1x} = \sqrt{k_o^2 n_1^2 - \beta^2}$$

$$k_{2x} = \sqrt{k_o^2 n_2^2 - \beta^2}$$

$$k_{3x} = \sqrt{k_o^2 n_3^2 - \beta^2}$$

with $\phi = k_{2x}d$, where d is the gap spacing between the waveguide and attenuator. In this case, the field in region II is evanescent. Therefore,

$$k_{2x} = -i\frac{2\pi}{\lambda}\sqrt{n_1^2 \sin^2\theta_1 - n_2^2} \equiv -iq$$

Hence $\phi = iqd$, and the expression for T becomes:

$$T = \frac{n_3 \cos\theta_3}{n_1 \cos\theta_1}\left|\frac{t_{12}t_{23}e^{-qd}}{1 + r_{12}r_{23}e^{-2qd}}\right|^2$$

2.3.3.b Matrix Method Calculation

The same answers for t and T can be derived using the matrix method. Using Yeh's notation [78], one can write:

$$\begin{pmatrix} A_o \\ B_o \end{pmatrix} = \begin{pmatrix} M_{11} & M_{12} \\ M_{21} & M_{22} \end{pmatrix} \begin{pmatrix} A'_s \\ B'_s \end{pmatrix}$$

where

$$\begin{pmatrix} M_{11} & M_{12} \\ M_{21} & M_{22} \end{pmatrix} = \frac{1}{t_{12}} \begin{pmatrix} 1 & r_{12} \\ r_{21} & 1 \end{pmatrix} \begin{pmatrix} e^{i\phi_2} & 0 \\ 0 & e^{-i\phi_2} \end{pmatrix} \frac{1}{t_{23}} \begin{pmatrix} 1 & r_{23} \\ r_{32} & 1 \end{pmatrix}$$

Since the transmission coefficient is defined as $t \equiv 1/M_{11}$, multiplying the matrices through to solve for M_{11} and hence t gives:

$$t = \frac{t_{12}t_{23}e^{-i\phi_2}}{1 + r_{12}r_{23}e^{-2i\phi_2}}$$

This is the same result as derived from Airy summation. Hence the expressions for transmittance and loss which follow are equivalent.

2.3.3.c Analysis of Leakage Results

Solving for T and then using Eq. (2.7) to solve for loss gives results which are plotted in Fig. 13. For comparison, the results from the normalization factor analysis and from the three-layer leaky mode formula are plotted as well. As expected, there is an inverse exponential dependence on gap spacing, which is characteristic of tunneling

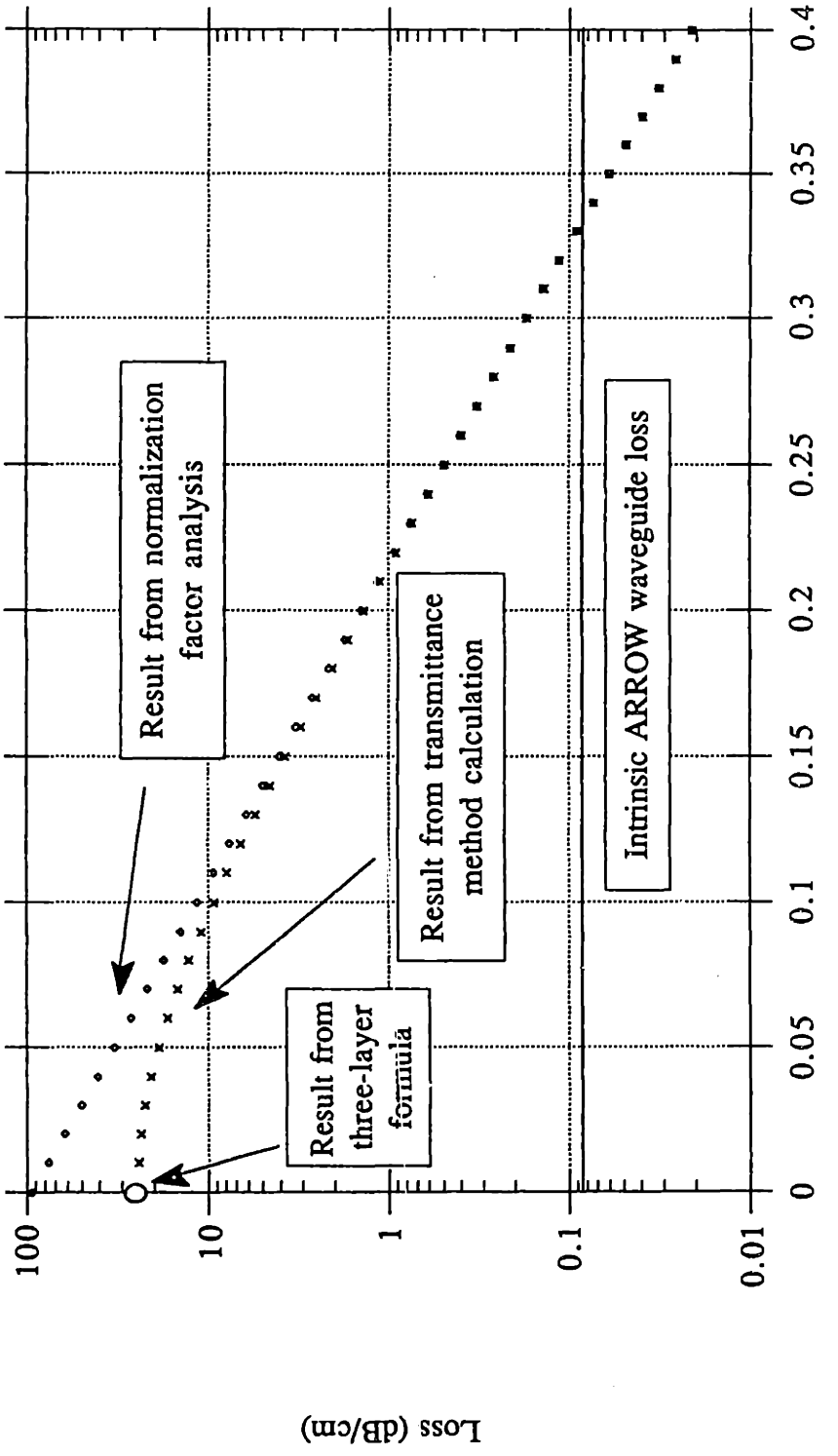

Fig. 13 Comparison of theoretical results

phenomena. Mathematically this is clear since as d gets large, the expression for the transmission coefficient is reduced to:

$$t \sim t_{12}t_{23}e^{-qd}$$

which shows the inverse exponential dependence. Inserting values for our structure into this formula gives the following expression for loss:

$$L = 94.7e^{-2qd} \qquad \text{(dB/cm)}$$

which is quite close to the expression derived from normalization factor analysis. From Fig. 13 it is also clear that for d > 0.2 μm the matrix method results tend toward the results obtained from the normalization factor analysis. However for d < 0.2 μm, the results tend toward those of the three-layer calculation. Also shown in Fig. 13 is a baseline loss which corresponds to the intrinsic ARROW waveguide loss into the substrate. This loss should not be changed significantly by interaction with the attenuator, and represents an effective minimum loss value for this design.

In summary, this section provides a solid theoretical foundation on which to base further study. In the following chapter, numerical simulation techniques are used to more accurately study this interaction. These computational methods open the door to understanding many more complex issues as well.

Chapter 3

Numerical Simulation Studies

Numerical simulation studies were performed in order to confirm the results obtained from theoretical analysis. First and most importantly, a more complete understanding of the interaction phenomenon was sought, as it forms the basis for device operation. In order to get an understanding of the important effects while keeping computation time to a minimum, two-dimensional vector beam propagation studies were used to determine the expected loss per unit propagation length as a function of gap spacing. This work is summarized in Section 3.1. From this information, the complete sensor structure was simulated by performing a numerical integration of expected loss over the entire optical path length of the device. This simulation work is reported in Section 3.2 and helps to explain how device dimensions influence sensor response. In order to understand how the choice of attenuator material affects sensor response, a study on how the real and imaginary components of the attenuator index affect loss was performed also using the two-dimensional beam propagation method. This is the subject of Section 3.3.

The two-dimensional approximation is expected to be fairly accurate, but the validity of this method can be checked more rigorously by performing a simulation of the full three-dimensional structure. Section 3.4 reports on the use of an eigen-solver

technique to calculate the expected attenuation loss as a function of gap spacing for varying ridge-etch depths. In the following two sections, three-dimensional vector beam propagation methods are used to analyze effects that pertain to the coupling of the electromagnetic wave from the input fiber to the optical waveguide. Section 3.5 reports on the effect of ridge-etch depth on the structure of the fundamental mode, which also has an effect on the efficiency of coupling into optical fibers. Section 3.6 discusses the radiative transition that occurs as a fiber input mode propagates down the longitudinal axis and settles down to a fully-developed ARROW mode. The length of this transition region is of some importance, since previous simulations have assumed a stable ARROW field structure in the active sensing area.

As described above, a variety of numerical simulation methods were used in order to understand the sensor response. Since the choice of an appropriate simulation method is important, a brief word on simulation techniques is in order. In general, simulation techniques can be classified by the two types of problems they try to solve: eigen-problems and propagation problems. Simulation methods that attempt to solve eigen-problems include the effective-index method, the variational method, and the finite-element method. Methods that are used to look at the propagation problem include finite-difference time domain (FDTD) methods and beam propagation methods. In general, propagation methods are used when one wants to have complete details of the optical propagation. However, they can be quite computationally intensive and are often replaced by eigen-solver techniques when only the eigenmodes or propagation constants of a structure are desired.

Initial studies for this work were conducted using the beam propagation method (BPM). BPM is more computationally efficient than FDTD methods, but it can only be applied to simple structures where reflections along the propagation direction are minimal. Conventional BPM represents the electromagnetic field as a superposition of basis

functions. Wave propagation is modelled in the spectral domain and the effect of the non-homogeneous media is modelled as a phase correction in the spatial domain. The fast fourier transform (FFT) is used to link the two domains during the computation. However, this method can still take up a significant amount of computational time. In order to improve efficiency, the Fresnel wave equation can be solved directly by finite difference techniques. This method is known as FD-BPM. Unfortunately, the application of these particular methods to our work is limited, since these conventional methods solve only the basic scalar wave equation. Since the ARROW structure is a polarization dependent structure, it is important to incorporate the vectorial nature of the electromagnetic wave in the simulation. A simulation technique capable of handling these ideas was developed by Chenglin Xu and Weiping Huang at the University of Waterloo in Ontario, Canada. This technique is known as the finite-difference vector beam propagation method (FD-VBPM), or more simply as VBPM. VBPM allows the distinction between TE and TM modes, and allows the calculation of cross-coupling between the two modes. A brief derivation of the equations that are solved is provided below. Further simulation details can be found in the literature [79-85].

The inhomogeneous vector Helmholtz equation for the electric field can be written as:

$$\nabla(\nabla \cdot \mathbf{E}) - \nabla^2 \mathbf{E} - n^2 k^2 \mathbf{E} = 0$$

This can be resolved into transverse and longitudinal components. However, knowledge of the transverse components is sufficient to describe the electric field completely, since the longitudinal component can then be calculated from Maxwell's equations. The transverse components of the field satisfy:

$$\nabla_t^2 \mathbf{E}_t + (n^2 k^2 - \beta^2)\mathbf{E}_t = \nabla_t \left(\nabla_t \cdot \mathbf{E}_t + \frac{\partial E_z}{\partial z} \right) \qquad (3.1)$$

From Gauss' Law, it can be written that:

$$\nabla \cdot (n^2 \mathbf{E}) = 0$$

which can be expanded as:

$$\nabla_t \cdot (n^2 \mathbf{E_t}) + \frac{\partial n^2}{\partial z} E_z + n^2 \frac{\partial E_z}{\partial z} = 0$$

In the problems solved in this thesis, the index distribution n(x,y) is assumed to be independent of z. Therefore:

$$\frac{\partial E_z}{\partial z} = -\frac{1}{n^2} \nabla_t \cdot (n^2 \mathbf{E_t}) \tag{3.2}$$

Substitution of Eq. (3.2) into Eq. (3.1), gives a vectorial Helmholtz equation in the desired form:

$$\nabla_t^2 \mathbf{E_t} + (n^2 k^2 - \beta^2)\mathbf{E_t} = \nabla_t \left[\nabla_t \cdot \mathbf{E_t} - \frac{1}{n^2} \nabla_t \cdot (n^2 \mathbf{E_t}) \right]$$

This equation can be written in matrix form as:

$$\begin{pmatrix} P_{xx} & P_{xy} \\ P_{yx} & P_{yy} \end{pmatrix} \begin{pmatrix} E_x \\ E_y \end{pmatrix} = \beta^2 \begin{pmatrix} E_x \\ E_y \end{pmatrix}$$

where the differential P-operators are defined as:

$$P_{xx}E_x = \frac{\partial}{\partial x}\left[\frac{1}{n^2}\frac{\partial}{\partial x}(n^2 E_x)\right] + \frac{\partial^2 E_x}{\partial y^2} + n^2 k^2 E_x$$

$$P_{yy}E_y = \frac{\partial^2 E_y}{\partial x^2} + \frac{\partial}{\partial y}\left[\frac{1}{n^2}\frac{\partial}{\partial y}(n^2 E_y)\right] + n^2 k^2 E_y$$

$$P_{xy}E_y = \frac{\partial}{\partial x}\left[\frac{1}{n^2}\frac{\partial}{\partial y}(n^2 E_y)\right] - \frac{\partial^2 E_y}{\partial x \partial y}$$

$$P_{yx}E_x = \frac{\partial}{\partial y}\left[\frac{1}{n^2}\frac{\partial}{\partial x}(n^2 E_x)\right] - \frac{\partial^2 E_x}{\partial y \partial x}.$$

This is the full vectorial form of the Helmholtz equation. Cross-coupling between the polarizations is given by P_{xy} and P_{yx}. If these terms are both zero, then the full vectorial equation reduces to the semi-vectorial form. If $P_{xx} = P_{yy}$, then there is no polarization dependence, and the probem reduces to the scalar wave equation.

Finally it is important to note that although VBPM is good at solving a variety of problems, it can be computationally intensive, especially for three-dimensional problems. Therefore, when complete details of propagation are not required, often an eigen-solver technique can be used instead. These are especially useful when one only needs to determine eigenmodes or the propagation constants of these modes. In this work, eigen-solver techniques are used to calculate the expected attenuator loss as a function of gap spacing for a variety of ridge-etch depths. This type of problem would require a significant amount of computational time using a VBPM technique due to its three-dimensional nature.

The following sections describe several aspects of the simulation work in further detail. Much of the simulation work reported here (Sections 3.1, 3.4 - 6) was performed in conjunction with Chenglin Xu and Weiping Huang of the University of Waterloo (Ontario, Canada). The effect of the real and imaginary part of the attenuator index on device performance (Section 3.3) was assessed with the help of Karl Kissa of the Charles Stark Draper Laboratory.

3.1 Effect of Gap Spacing on Attenuation Loss

A two-dimensional VBPM was used in order to study the effect of gap spacing on leakage into the attenuator. The computation window consisted of a 20 μm high by 1 mm long region that comprised the silicon attenuator, air gap, ARROW waveguide, and silicon

substrate as shown in Fig. 14. Light in the fundamental ARROW mode was injected into the waveguide at the left side of the structure and the power transmitted through to the right side of the window was calculated. As expected, it was found that for small gap spacings ($g < 0.3$ μm), loss was strongly dependent on gap spacing, whereas for larger gap spacings ($g > 0.4$ μm) there was little effect of gap spacing on loss. These results are shown and compared with the transmittance method calculation of Section 2.3.3 in Fig. 15. It can be seen that the curve can be broken into two regions. For gap distances lower than 0.3 μm, the loss is exponentially dependent on the gap spacing with a slight levelling off at very small gap spacings as predicted by the theoretical studies. For gap distances greater than 0.4 μm, the intrinsic loss into the substrate dominates the attenuator loss; therefore the total loss does not appear be a function of gap spacing. The result shown in Fig. 15 characterizes the loss mechanism used in device operation. With this information in hand, the expected performance of the entire sensor structure can now be determined.

3.2 Simulation of Complete Sensor Structure

In order to simulate the losses of the entire sensor structure, the response of the sensor in the active region as well as the outlying passive regions must be determined. This is shown schematically in Fig. 16. Regions I and III represent the outlying regions which are not modulated by diaphragm deflection. Region II is the active sensor area and the area of critical interest. Analysis of the complete sensor response was performed by numerically integrating the loss over all three regions. Thus, the interactions in regions I and III partially determine the baseline of how much light is transmitted through the entire structure, while the interaction in region II determines the degree of modulation of the

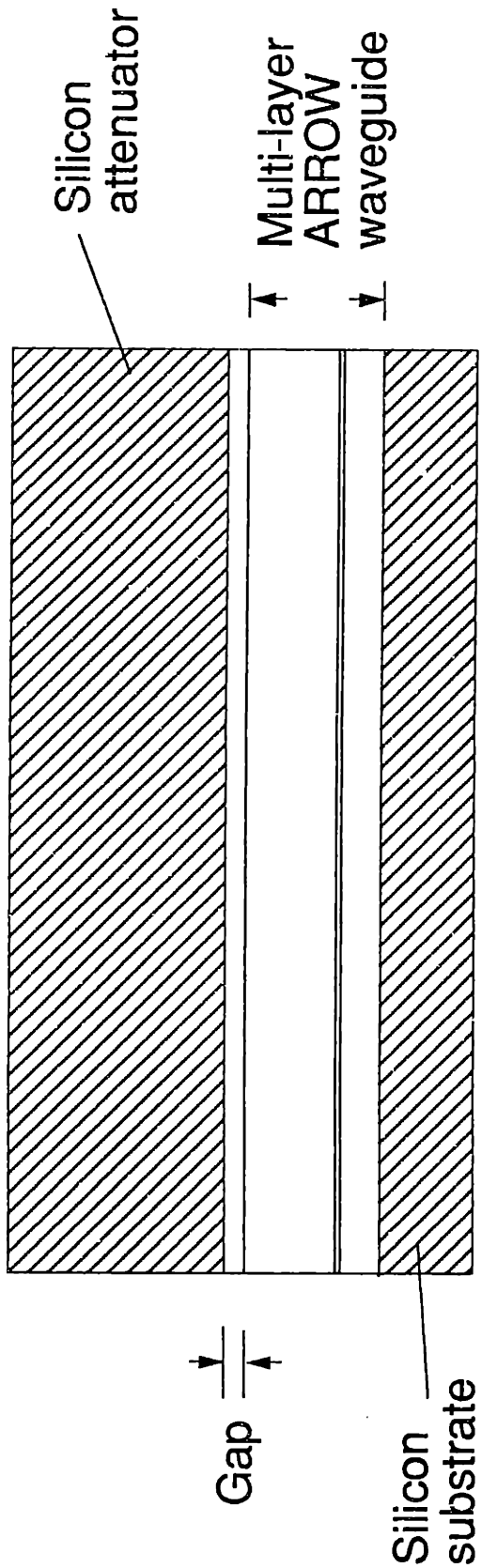

Fig. 14 Computation Window (20 μm x 1 mm) for Vector Beam Propagation Method (VBPM) Loss Simulation

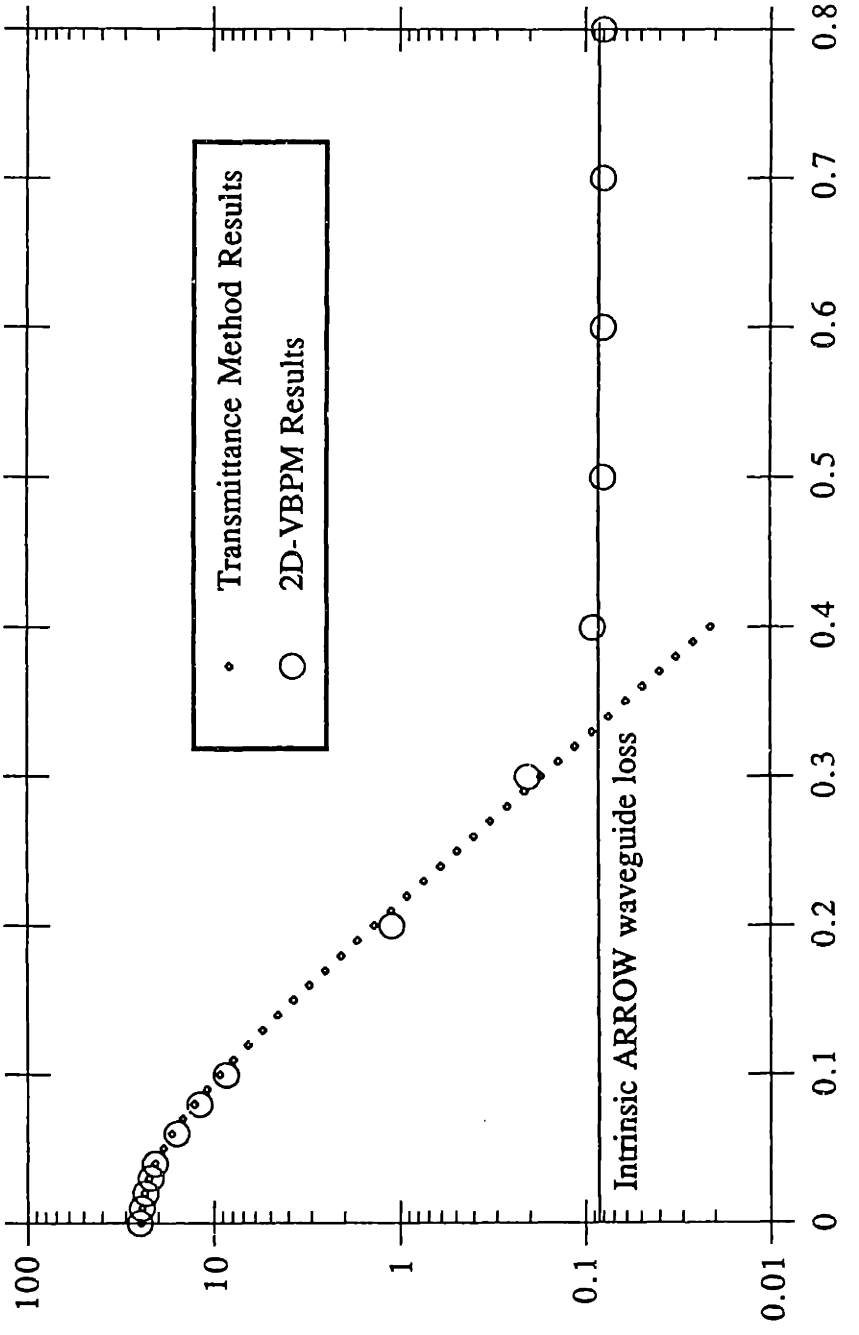

Fig. 15 Comparison of 2D-VBPM and Transmittance Method Results

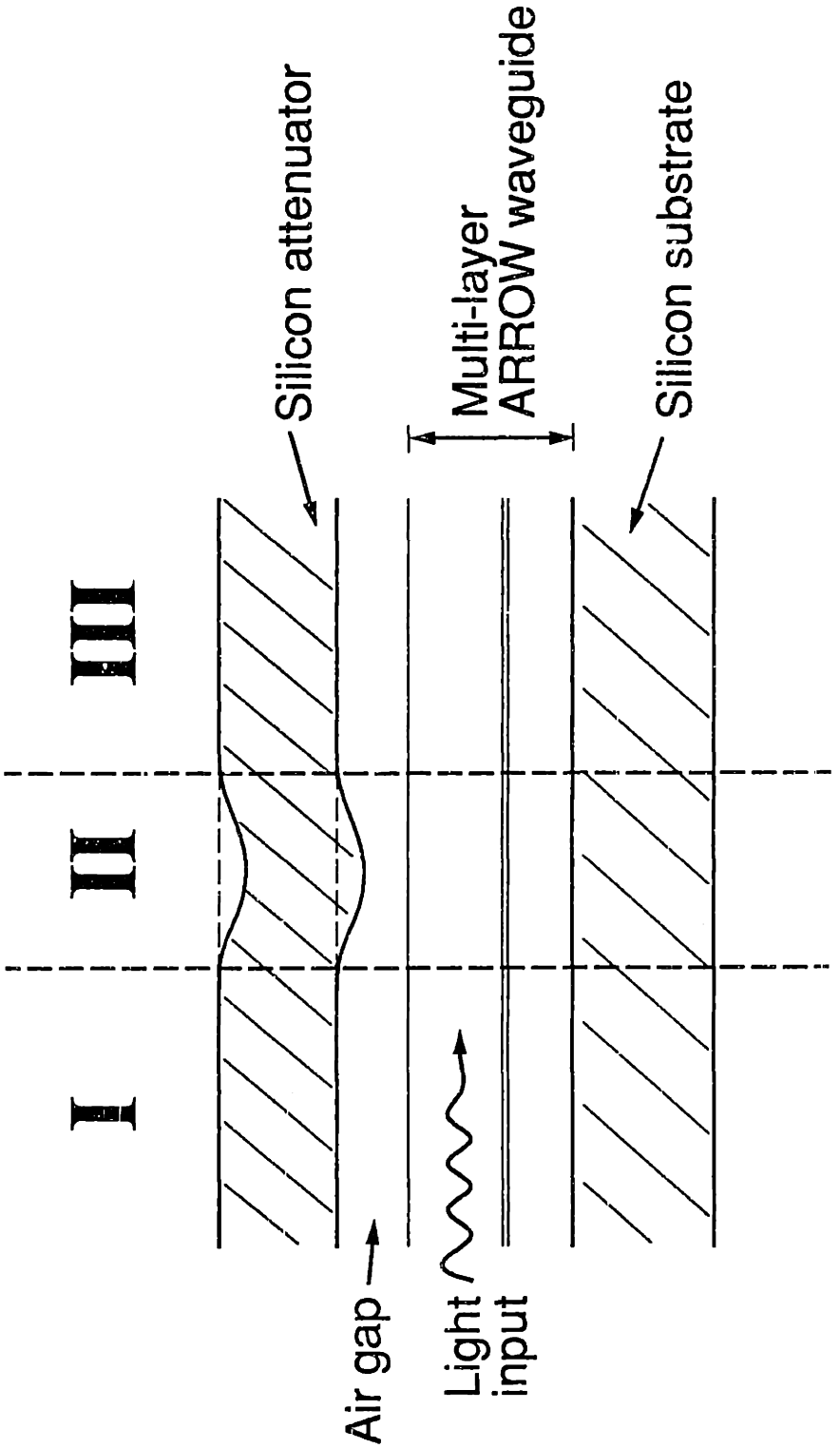

Fig. 16 Schematic of cross-section used for numerical integration

output response. A sample plot of simulated device response for different diaphragm sizes is shown in Fig. 17. As expected, as the gap spacing is decreased, the normalized transmitted output, which is defined as transmitted output power divided by input power, also decreases. If the gap is decreased down to the range of 0.1 μm, linearity in the sensor response can be achieved. This linearity does come at the expense of signal strength, but this loss of about two-thirds of the input power should pose no major obstacles in signal detection. These plots demonstrate that the design of an optical transducer to measure pressure and force should be theoretically possible. The more interesting questions now become whether alignment between components can be achieved with existing process technologies and whether or not interaction across such a microfabricated gap can proceed repeatably. These are process specific questions and will be addressed in the context of experimental testing in Chapter 5.

3.3 Effect of the Real and Imaginary Components of Attenuator Index on Loss

Sensor designs with different real and imaginary components of attenuator index could offer significant performance advantages over the silicon diaphragm attenuator previously presented. With this in mind, a study was undertaken with Karl Kissa of the Charles Stark Draper Laboratory to determine how the loss curves for the device would depend on the values of attenuator n and k. A plot of loss in dB/cm as a function of gap spacing for various values of n is shown in Fig. 18. The silicon used as the attenuator material in this work has a refractive index, n=3.883. On the basis of the work performed in Section 3.2, this index appears sufficient to ensure a reasonable sensor response. It can

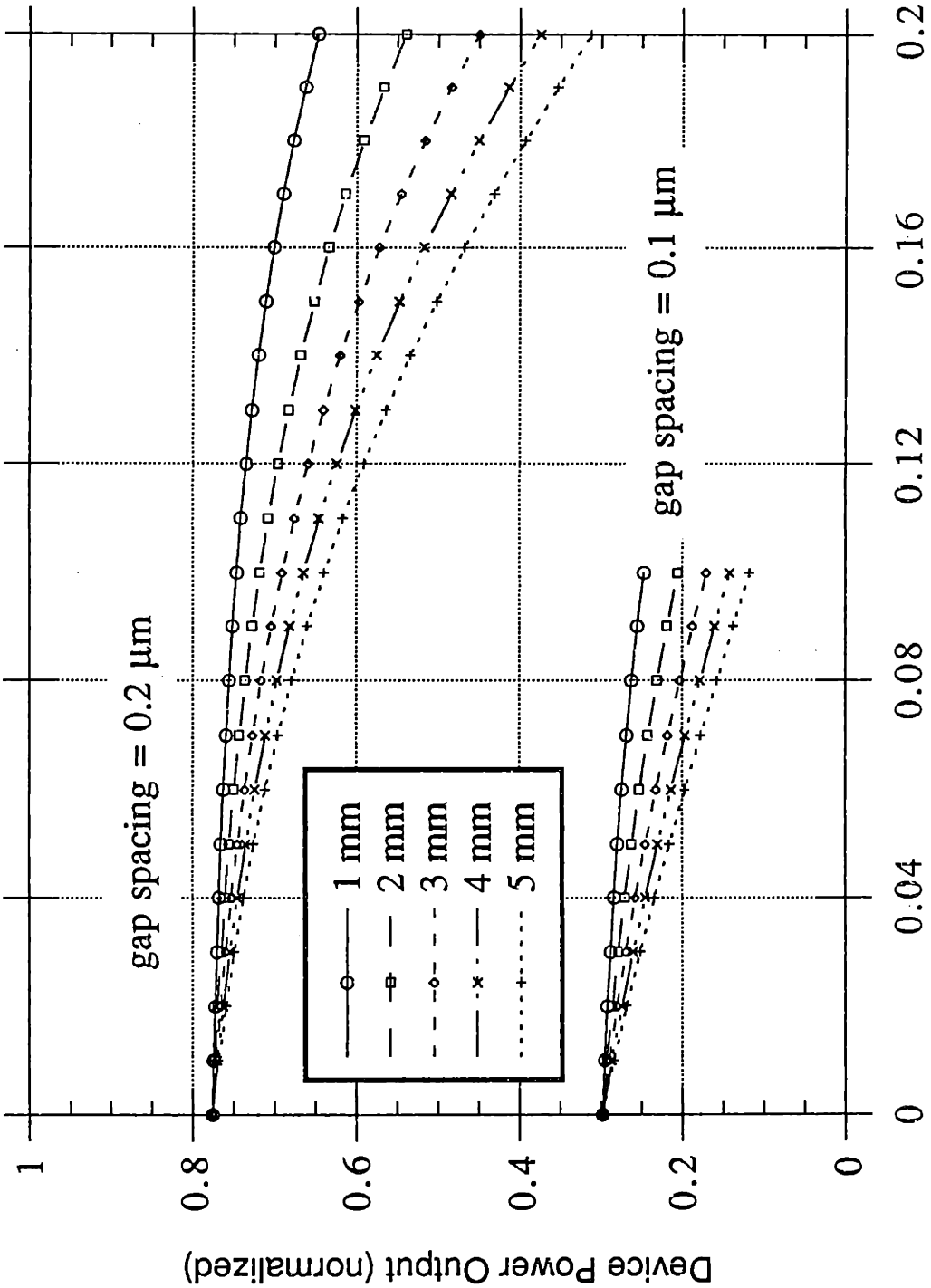

Fig. 17 Full ARROW Device Loss Simulation for Various Diaphragm Side Lengths (chip size = 1 cm)

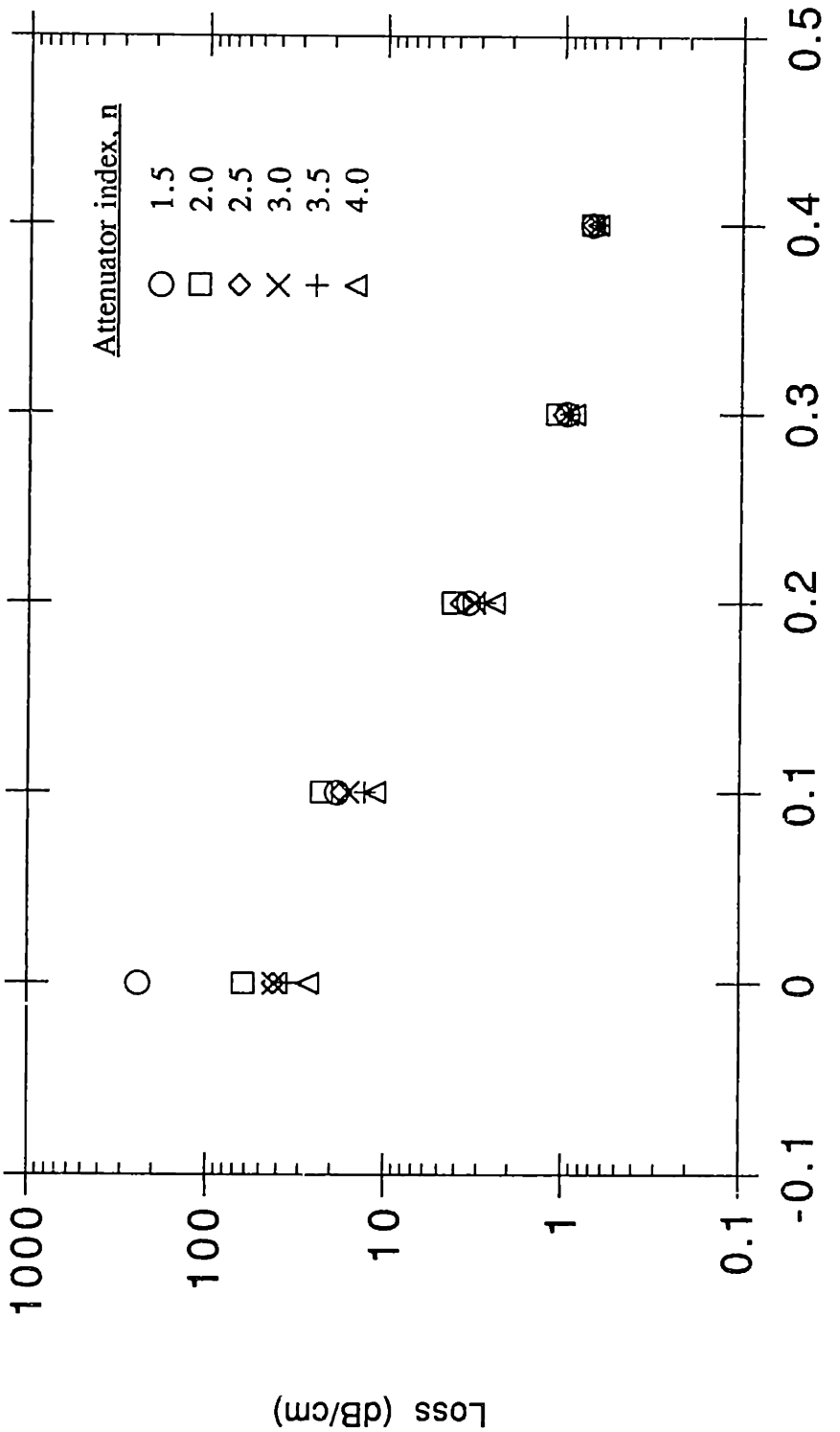

Fig. 18 Loss vs. gap spacing for various n

be seen that from n=2.0 to n=4.0 there is only a maximum variation of about a factor of 2 in expected losses. However, as n approaches the effective index of the waveguide (1.456), the expected loss gets very high. Therefore, if greater maximum loss per distance is required, a change could be made to an attenuator material with a much lower refractive index, such as glass (n ~ 1.5). It is important to note that changes in material do not extend the range of interaction significantly, since at gap spacings above 0.3 μm, the change in material has very little effect on attenuation response. Figs. 19 and 20 show transmission versus n and k respectively for different values of gap spacing. Fig. 19 shows that increasing n increases the transmission through the device. This is because as long as attenuator index is higher than the index of the waveguide core, leakage will be greater for attenuators with indices closer to that of the core. This is the same result as that predicted by the theoretical analysis in Section 2.3.2. Fig. 20 shows that increasing k also increases transmittance. Although k is often thought of as representing absorbance, the k-term actually increases the reflectivity of the attenuator when it is large, and hence decreases the loss seen by the structure. Therefore, a low value of k is desirable for enhanced interaction. This is the case for silicon (k = 0.019) as well as for other non-metal materials used in semiconductor processing.

3.4 Effect of Ridge-Etch Depth on Attenuation Loss

Ridge-etching can be expected to change the mode shape of the electric field in an ARROW waveguide and hence would also be expected to change the interaction with the attenuator. In the above two-dimensional simulations, this effect was assumed to be negligible. The validity of this assumption is investigated in this section. Since a full 3D

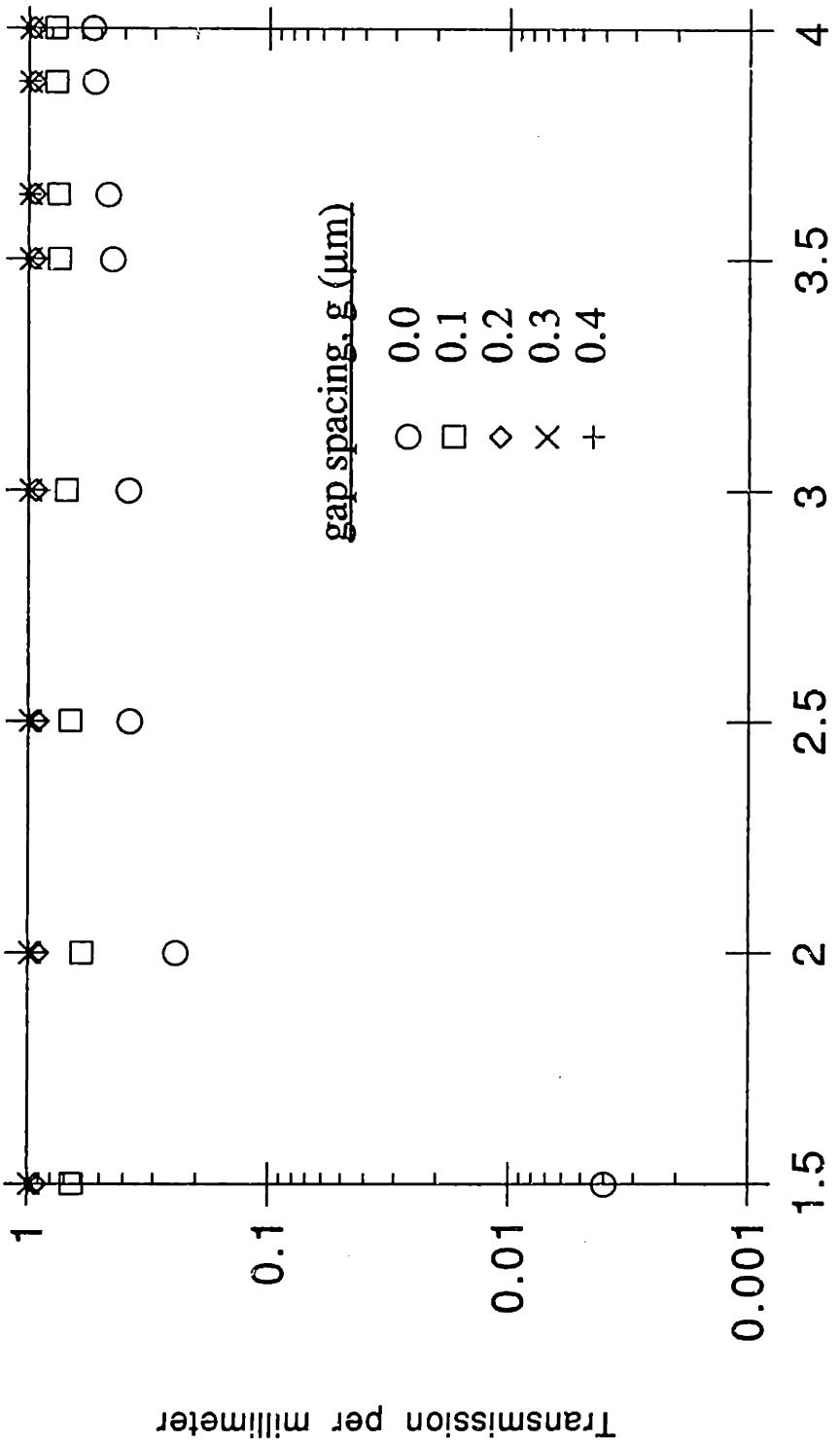

Fig. 19 Transmission vs. n for different gaps

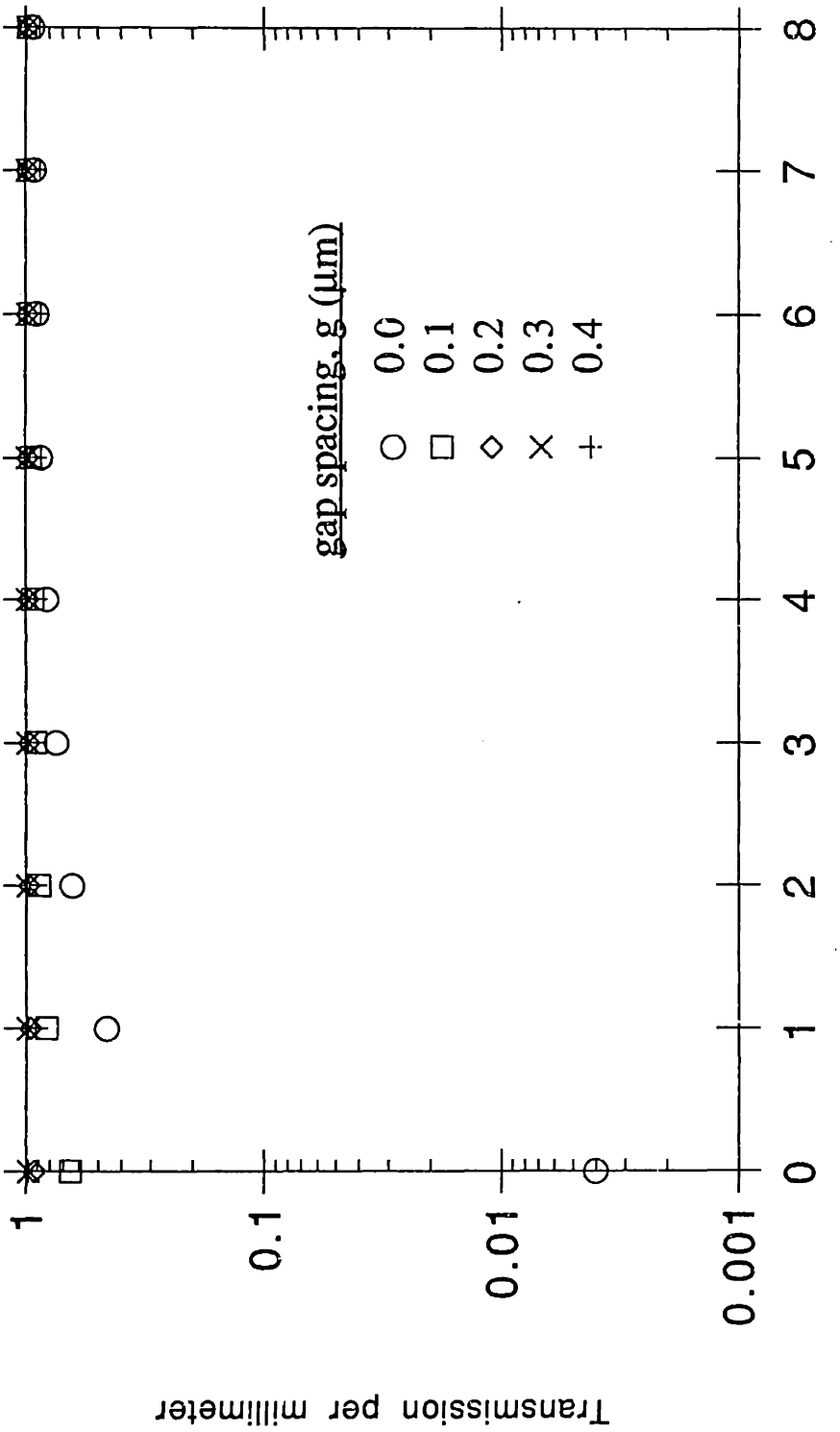

Fig. 20 Transmission vs. k for different gaps

simulation of the structure for an array of gap spacings and ridge-etch depths would be very computationally intensive, a more computationally efficient eigen-solver approach was used to determine the complex propagation constant of the desired structures. The imaginary portion of the propagation constant was then used to calculate the expected loss per distance for the fundamental mode of the structure. A plot of loss versus gap spacing for various etch-depths is shown in Fig. 21. The results for 3.0 μm and 4.0 μm etch depth are very close, while the 1.0 μm and 2.0 μm curves show some oscillatory divergences. In order to determine which etch-depths are satisfactory from a loss perspective, these points are re-plotted to show loss as a function of ridge-etch depth as shown in Fig. 22. The results are plotted for gap spacings from 0.0 μm to 0.5 μm in increments of 0.05 μm, and for ridge-etch depths from 0 to 4 μm. The graph shows that there is a great drop-off in expected loss in the region from 0 to 1 μm, which is a region that should be avoided in the design process. One might also guess that such a region would be poor for lateral confinement of the guided wave, and hence poor for coupling efficiency. In order to investigate what effect the ridge-etch might have on lateral confinement, the 3D-VBPM technique was used to look at details of the mode structure more carefully.

3.5 Effect of Ridge-Etch Depth on Fundamental Mode Structure

The depth of the ridge-etch is expected to greatly affect the optical coupling efficiency from fiber to waveguide. Since the coupled power can be approximated as the overlap integral between the fiber mode and the fundamental waveguide mode, the shape of the fundamental mode can be used as a criterion for the evaluation of expected coupling efficiency. In order to perform this evaluation, the propagation of the fiber input power

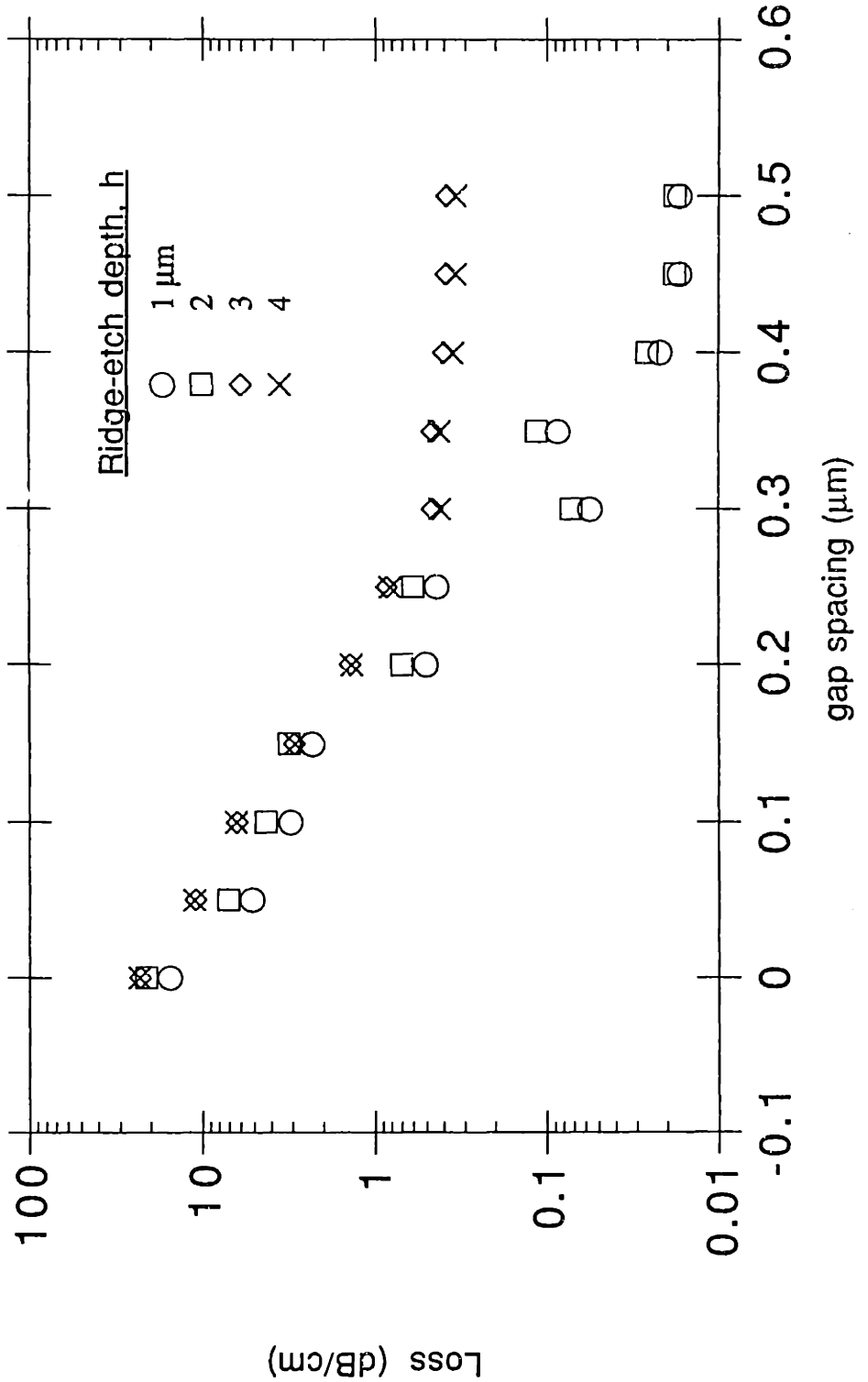

Fig. 21 Loss vs. gap spacing for different ridge-etch depths

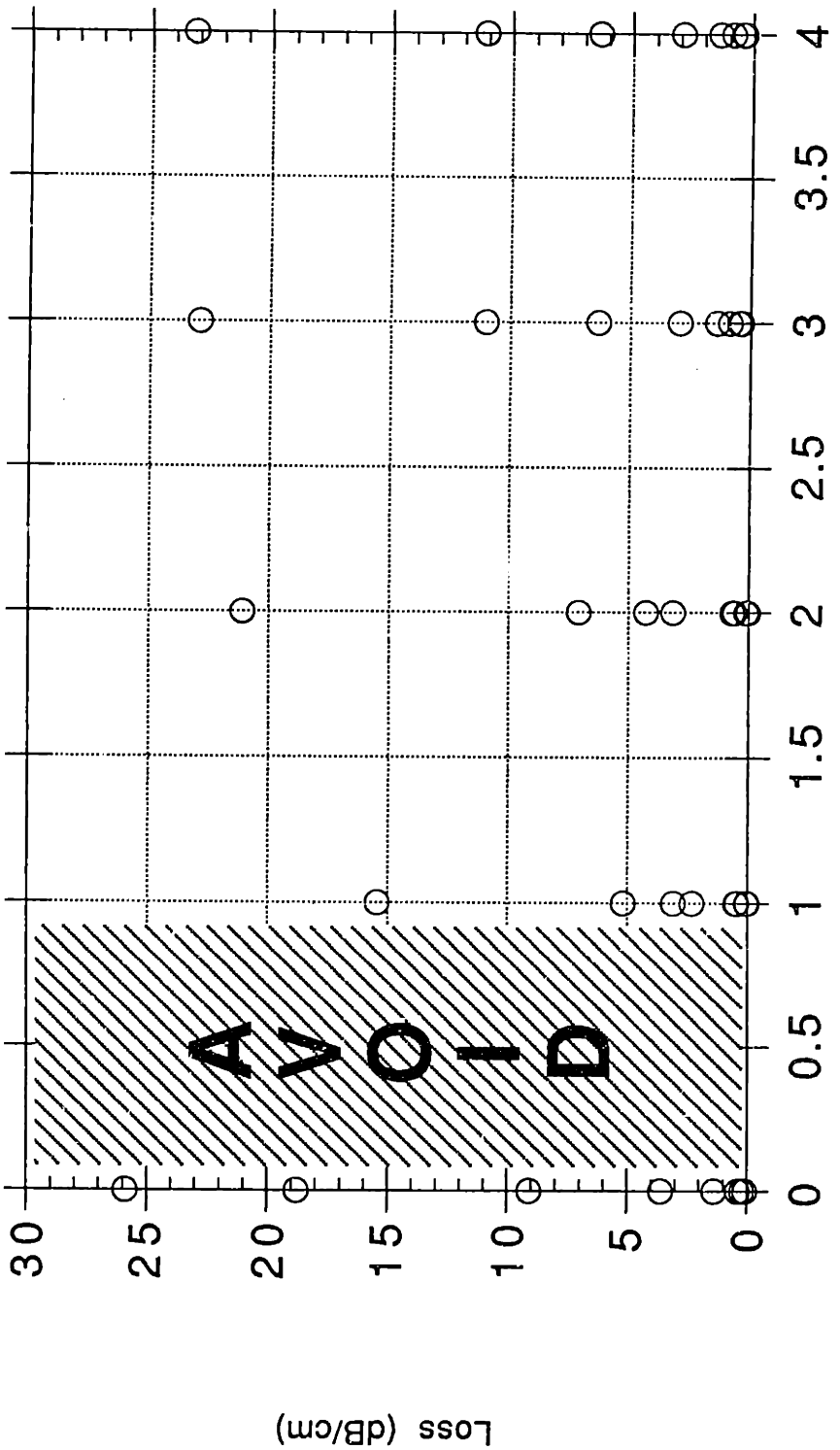

Fig. 22 Loss vs. ridge-etch depth

through the waveguide is simulated. Since higher order modes will be radiated away, the expected fundamental mode can be determined for any given ridge-etch depth. Modes with profiles that most closely resemble the known fiber input will have the greatest coupling efficiency. This effect was studied using a 3D-VBPM simulation with the geometry shown in Fig. 23. The ridge-etch depth, H, of 5-μm-wide waveguides was set to three different values: 0.5 μm, 1.0 μm, and 2.0 μm. A gaussian input beam, 4 μm wide in diameter and centered on the core center, was injected into the waveguide. This light was allowed to propagate for 2.0 mm and the output field was extracted at the z=2.0 mm plane. The results from this study are shown in the power contour plots of Fig. 24. Successive contours represent power differentials of 2 dB. As can be seen, there is extreme light spreading in the lateral direction for ridge-etch depths of less than 0.5 μm. Reasonably good confinement can be seen for ridge-etch depths greater than 1.0 μm. These results demonstrate that shallow ridge-etch depths allow lateral spreading of the beam, thus leading to a corresponding drop in the expected coupling efficiency. This study also appears to re-affirm the design considerations of Section 3.4, since lateral spreading of the beam due to shallow ridge-etch depths also results in decreased interaction strength with the attenuator.

3.6 Longitudinal Stability of Modes Launched Into Ridge-Etched ARROW Structures

The final simulation issue discussed here deals with the longitudinal stability of the mode structure. It is known that the conversion of the injected gaussian mode to the fundamental ARROW mode occurs through a process of radiation over some finite, non-zero distance. For reproducibility, it is important to be able to design the waveguiding

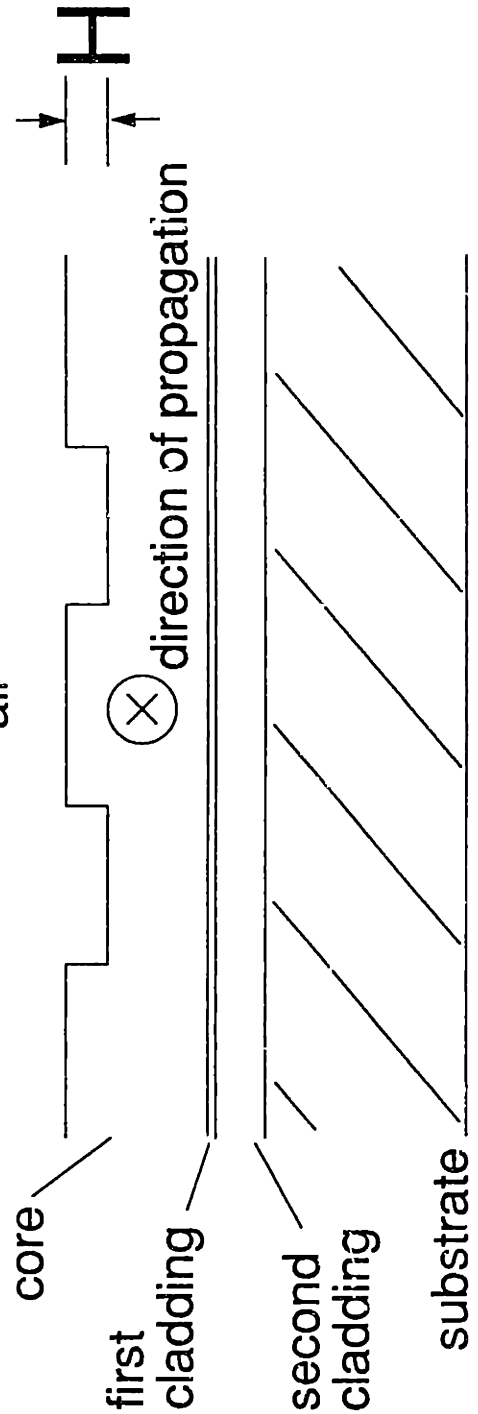

Fig. 23 Rib structure used for vector beam propagation method (VBPM) analysis

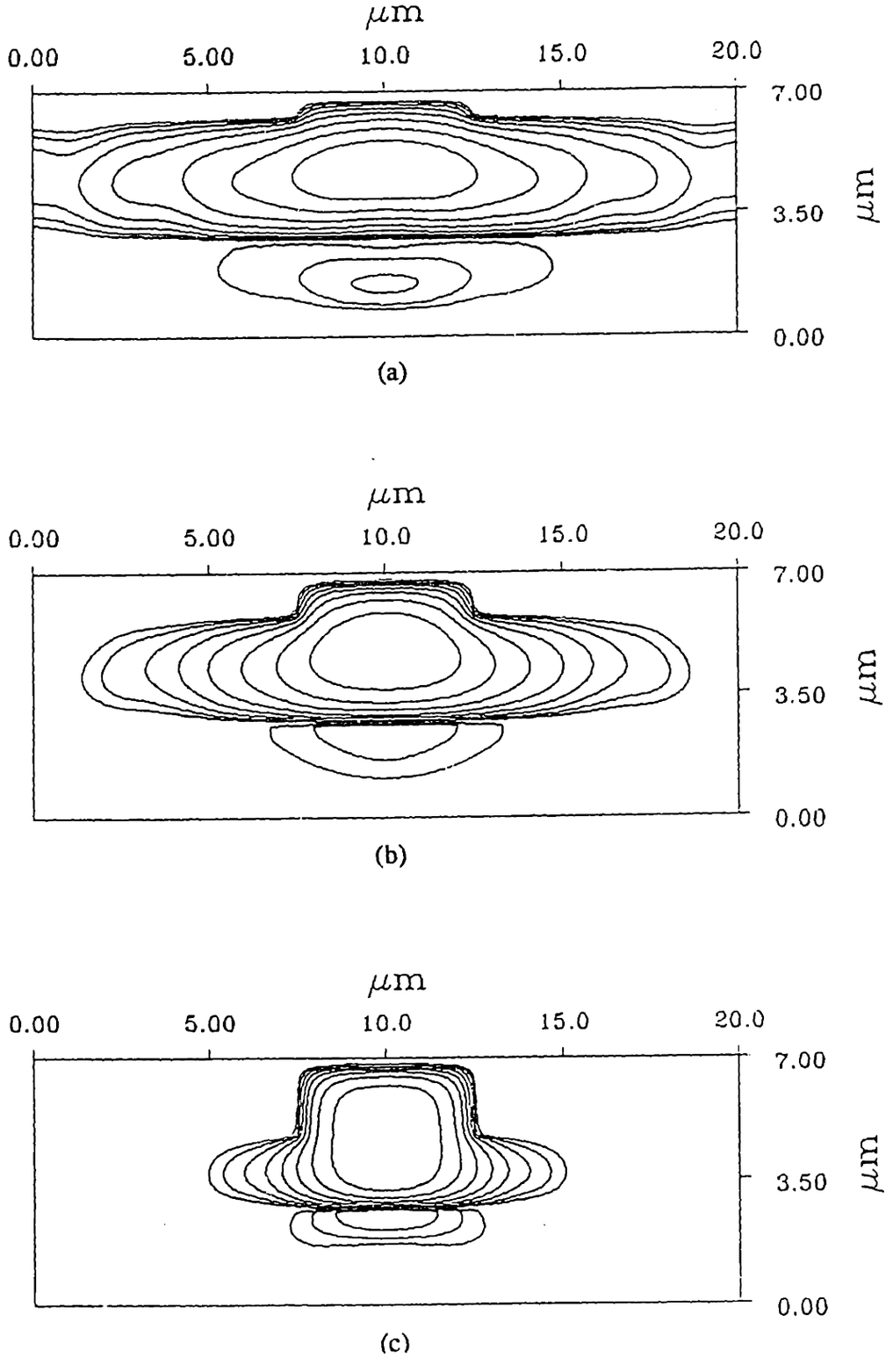

Fig. 24 Waveguide power cross-sections taken at z = 2.0 mm for varying rib heights, H, (a) H = 0.5 μm, (b) H = 1.0 μm, (c) H = 2.0 μm

structure so that radiative modes are completely stripped away by the time the electromagnetic wave reaches the active sensing area. To verify that this design criterion has been satisfied, a 3D-VBPM simulation was performed using the geometry shown in Fig. 25. A ridge-etched ARROW waveguide structure with a ridge-etch depth of 1.0 μm was extruded in the z-dimension. A gaussian beam was input at the center of the core and this wave was allowed to propagate through the entire structure. Power cross-sections were recorded at intervals of 0.4 mm out to a distance of 2.0 mm. The results of this test are shown in Fig. 26. The input gaussian can be seen at z=0.0 mm. The results for z=0.4 mm and z=0.8 mm still show quite a bit of radiation loss, whereas near z=1.2 mm the light begins to settle down to the expected ARROW mode pattern. At greater distances, the mode appears to have achieved stability. Hence, it seems desirable to design a transition region of at least 2 mm at the input in order to let the mode structure settle to the fundamental ARROW mode.

3.7 Summary of Simulation Results

1) The effect of gap spacing on attenuation loss has been studied. Leakage is only enhanced at distances below 0.4 μm. For larger distances, the leakage to the substrate dominates.

2) The entire sensor structure has been simulated for device response curves. As the gap spacing is driven down below 0.2 μm, linearity of the sensor response appears to increase. However, the baseline of transmitted light decreases as well.

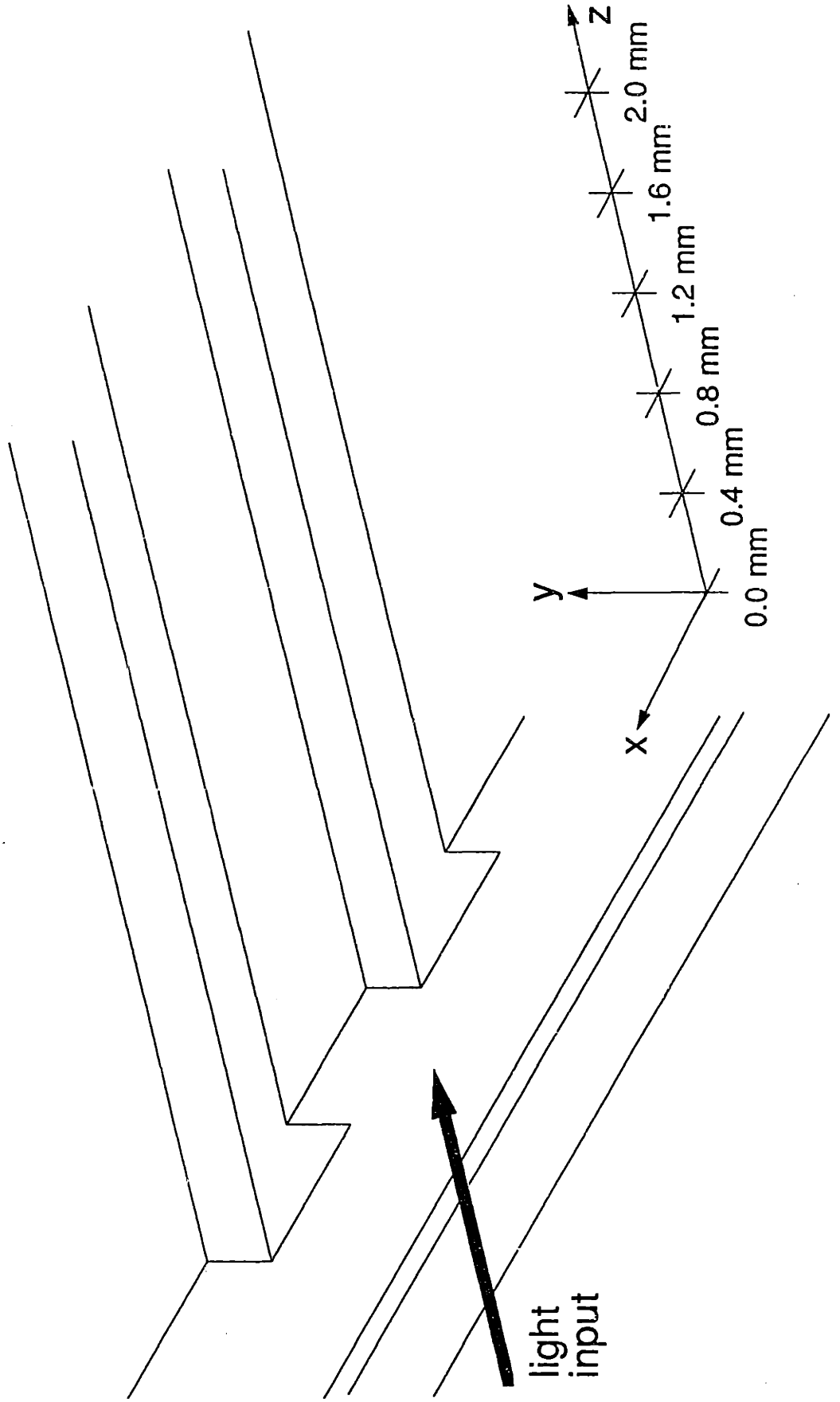

Fig. 25 Geometry used for longitudinal mode stability simulation

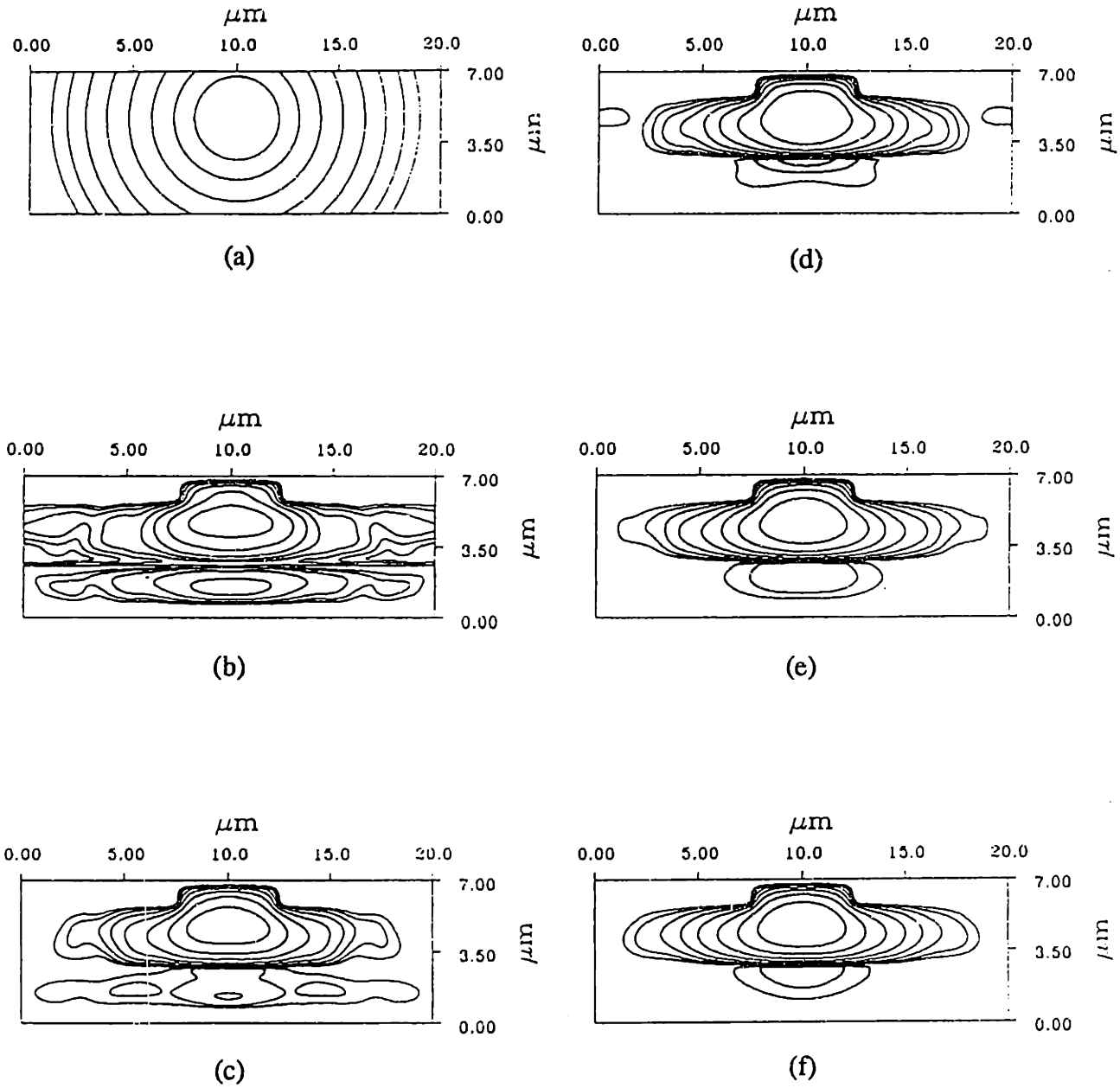

Fig. 26 Waveguide power cross-sections for rib height, H = 1.0 μm. Each contour represents 2 dB, (a) z = 0.0 mm, (b) z = 0.4 mm, (c) z = 0.8 mm, (d) z = 1.2 mm, (e) z = 1.6 mm, (f) z = 2.0 mm

3) The effects of the real and imaginary indices of the attenuator have been studied. Even if the real part of the index, n, is much higher than the effective index of the core, the leakage induced is still large enough to be satisfactory for sensor response. Leakage levels become even higher as n approaches the effective index from above. Large values of the imaginary part of the index, k, imply reflection of light away from the attenuator part, and appear to decrease device sensitivity. Thus, the leakage effect is found to be the predominant mechanism of loss used in the operation of this device. The impact of absorption is a higher order effect.

4) The ridge-etch depth is seen to affect the attenuation loss. Shallow ridge-etches result in broad beam spreading, which give rise to low levels of interaction with the attenuator, and hence low loss. It is important to use etch depths greater than 1.0 μm.

5) Alignment tolerances of the fiber to the waveguide appear good, assuming ridge-etch depths greater than 1.0 μm are used. Lateral spreading of the beam appears to cause both reduced coupling efficiency as well as reduced levels of interaction with the attenuator.

6) The radiative conversion of the fiber gaussian mode to the ARROW mode profile requires a transition distance on the order of 2 mm. Hence any sensor structures modelled based on the interaction of ARROW waveguides with a leakage-inducing attenuator should have at least a 2 mm transition region between the fiber input and the active sensing area.

Chapter 4

Fabrication

This chapter will discuss the various fabrication processes that were developed during the fabrication of the microsensor. As discussed in Section 1.3, the sensor is formed through the bonding of two separate wafers: a "waveguide wafer", which supports the ridge-etched waveguide structure, and a "diaphragm wafer", which forms the silicon light attenuator and includes the microfabricated gap spacer. Section 4.1 will detail the process sequence used to fabricate these individual components. Section 4.2 will discuss the wafer bonding technologies that were developed, including both direct wafer bonding and an aligned electrostatic bonding process that was developed using infrared techniques. Finally, Section 4.3 will discuss the preparative processes required to turn a bonded wafer into a set of chips for test.

4.1 Fabrication Sequence

As described above, the fabrication of the sensor device proceeds through the bonding of two separate wafers: a "waveguide wafer", which supports the ARROW structure, and a "diaphragm wafer", which forms the silicon light attenuator and includes

the microfabricated gap spacer. In this section, the processes that were used to fabricate these individual components are detailed. First, the fabrication process for the waveguide wafer is described.

The basic strategy used for waveguide fabrication was composed of two elements. First, the entire ARROW structure was built up in slab form; then a plasma etch was used to create a ridge to provide lateral confinement. Four-inch (100) double-side-polished silicon wafers were used as substrates for building the ARROW structure. The first step in slab ARROW fabrication was the thermal oxidation of the silicon substrate to form the second cladding layer. This was a conventional dry-wet-dry oxidation at 950° C, with a steam oxidation time of 24 hours bracketed by dry oxidations of 30 minutes. This run was performed in an atmospheric furnace tube of a computer-controlled cantilever-loading Bruce BDF-4 furnace system. Measurements from a film thickness measurement system (Nanometrics Nanospec/AFT) indicated accuracy to within 5% of the intended 2.0 μm oxide layer thickness with less than 1% variation across any wafer surface. Further runs could be used to improve the thickness accuracy of the second cladding layer. However, this was judged as unnecessary in light of the broad process latitude inherent in the device design.

The first cladding layer of silicon nitride was then deposited on top of the thermally grown silicon dioxide layer by using low-pressure chemical vapor deposition. The recipe used was based on a standard CMOS silicon nitride deposition, and was nominally run at 800° C with dichlorosilane and ammonia gas flowing in a 5:3 ratio. The time of deposition was adjusted to give a desired first-cladding-layer thickness of 1140 Å. Measurements taken using both a Gaertner ellipsometer and the Nanospec system mentioned above indicate that depositions were typically within 50 Å of the desired target thickness, which should be more than sufficient for device operation.

The last step in fabricating the slab ARROW structure was the low-pressure chemical vapor deposition of the silicon dioxide core. Low-temperature oxide (LTO) deposition was the technology chosen primarily for compatibility with existing integrated circuit capabilities. This deposition was performed by reacting silane with oxygen to produce silicon dioxide and hydrogen gas. In this case, nitrogen gas was also flowed in the furnace tube as a safety precaution. The deposition of LTO was followed by a densification step which gives the oxide layer additional stability. However, the total thickness of the oxide layer is typically decreased by about 10% during this densification process. Thus, in order to achieve a final thickness of 4.0 μm, an initial pre-densification target thickness of 4.4 μm was selected. Repeated deposition of layers up to the target 4.4 μm thickness proved somewhat costly, and complete optimization of the LTO layer was not performed. To ensure a uniform thickness distribution from wafer to wafer, the 4.4 μm layer was deposited in two separate runs of 2.2 μm each and the position of the wafers in each run was changed to even out non-uniformities inherent in the deposition process. The deposited silicon dioxide was then densified for 1 hour at 1000° C to give the layer additional stability. A scanning electron micrograph (SEM) of an ARROW structure built on silicon is shown in Fig. 27. After testing, it was discovered that the LTO surface suffered from problems of particulate contamination. These problems are discussed in further detail in Chapter 5.

The three layer structure described above represents the standard slab ARROW structure as reported in much of the literature. This slab structure was then modified by using a ridge-etch to achieve lateral confinement. This ridge-etch was performed by plasma etching two parallel longitudinal stripes in order to define the light carrying ridge in the middle. This type of lateral confinement comes at the expense of sidewall scattering. Thus, the total scattering loss will strongly depend on the quality of the sidewall surfaces.

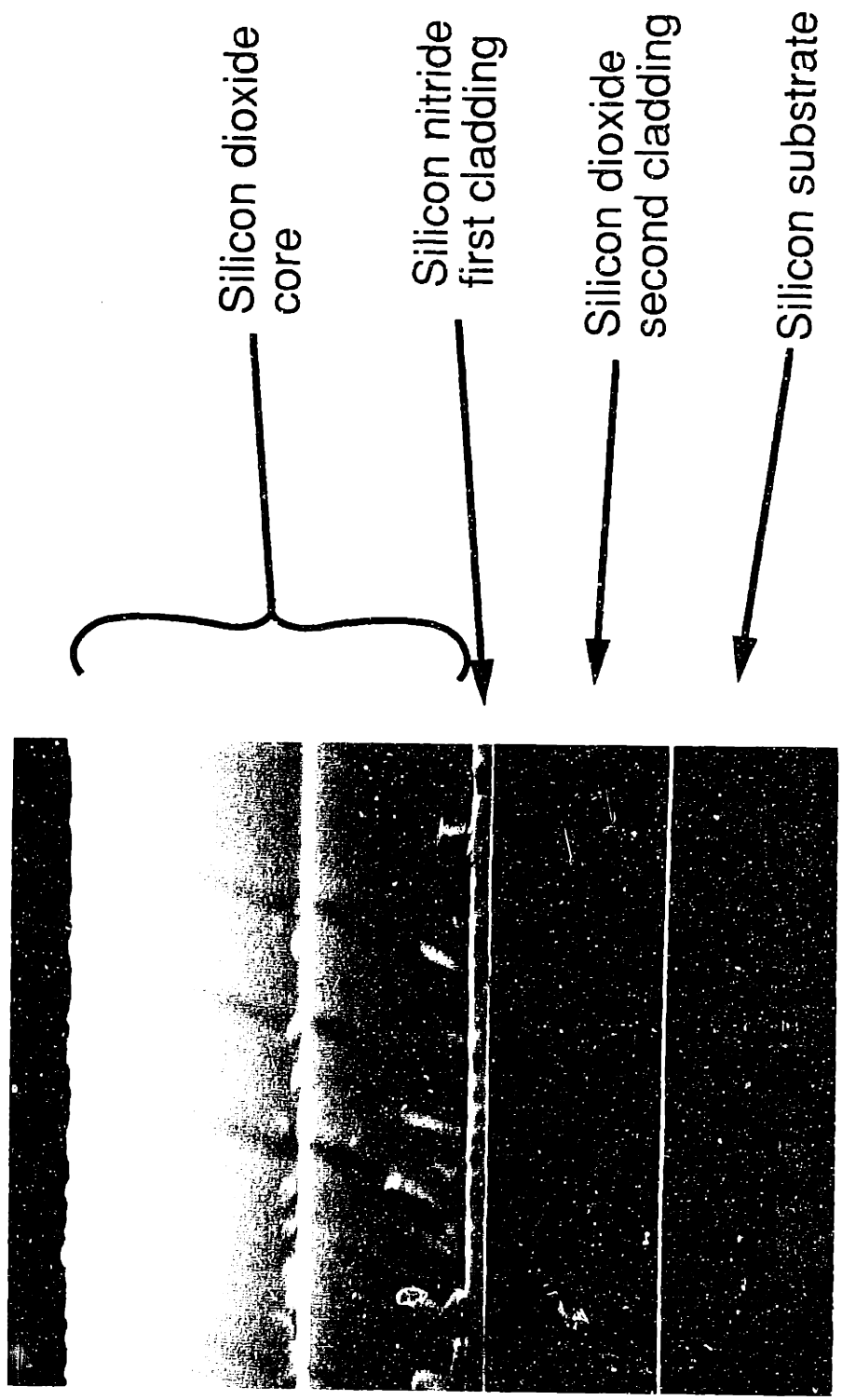

Fig. 27 Scanning electron micrograph of ARROW structure

Patterning was performed on a GCA Model 4800 DSW wafer stepper with 10X reduction. This method was chosen over contact alignment to reduce the transfer of feature roughness on the masks, which were generated by using a GYREX Model 1005A pattern generator. If the masks had been written by a more advanced technology (e.g. electron beam), it is possible that contact lithography would have been acceptable. However, the wafer stepper does have the added advantage of improved particulate control on the wafer surface. Photoresist was coated and developed on a GCA Model 1006 Wafertrac. Wafers were vapor-primed with hexamethyldisilizane (HMDS). In order to simplify future packaging, waveguides were stitched together across chip boundaries. This was accomplished by opening up the exposure aperture on the stepper, which is usually stopped down slightly to provide pattern isolation from chip to chip. The quality of stitching was checked through an optical microscope and appeared to be quite good. The only noticeable effect was a slight overexposure due to the double exposure of the stitched regions.

A dry-etch plasma process was used for silicon dioxide removal in a Lam Research plasma etcher (Model 594). Effort was aimed at making the sidewall geometry as smooth and nearly vertical as possible. It was observed that fluorine-deficient plasmas appeared to etch more anisotropically than conventional CF_4 plasmas. Fluorine deficient plasmas can be achieved by adding CHF_3 to a conventional oxide-etching gas mixture. It was found that adding CHF_3 to the plasma gas mixture also tended to increase etch rate until a point where a non-volatile residue appeared and etching essentially stopped. Data demonstrating this effect is shown in Fig. 28. An appropriate etching chemistry would require enough CHF_3 to provide anisotropic sidewalls and a reasonable etch rate, but must stay away from the point where the formation of the non-volatile residue halts the etching. Details of the final chemistry selected for etching are shown in Table 2.

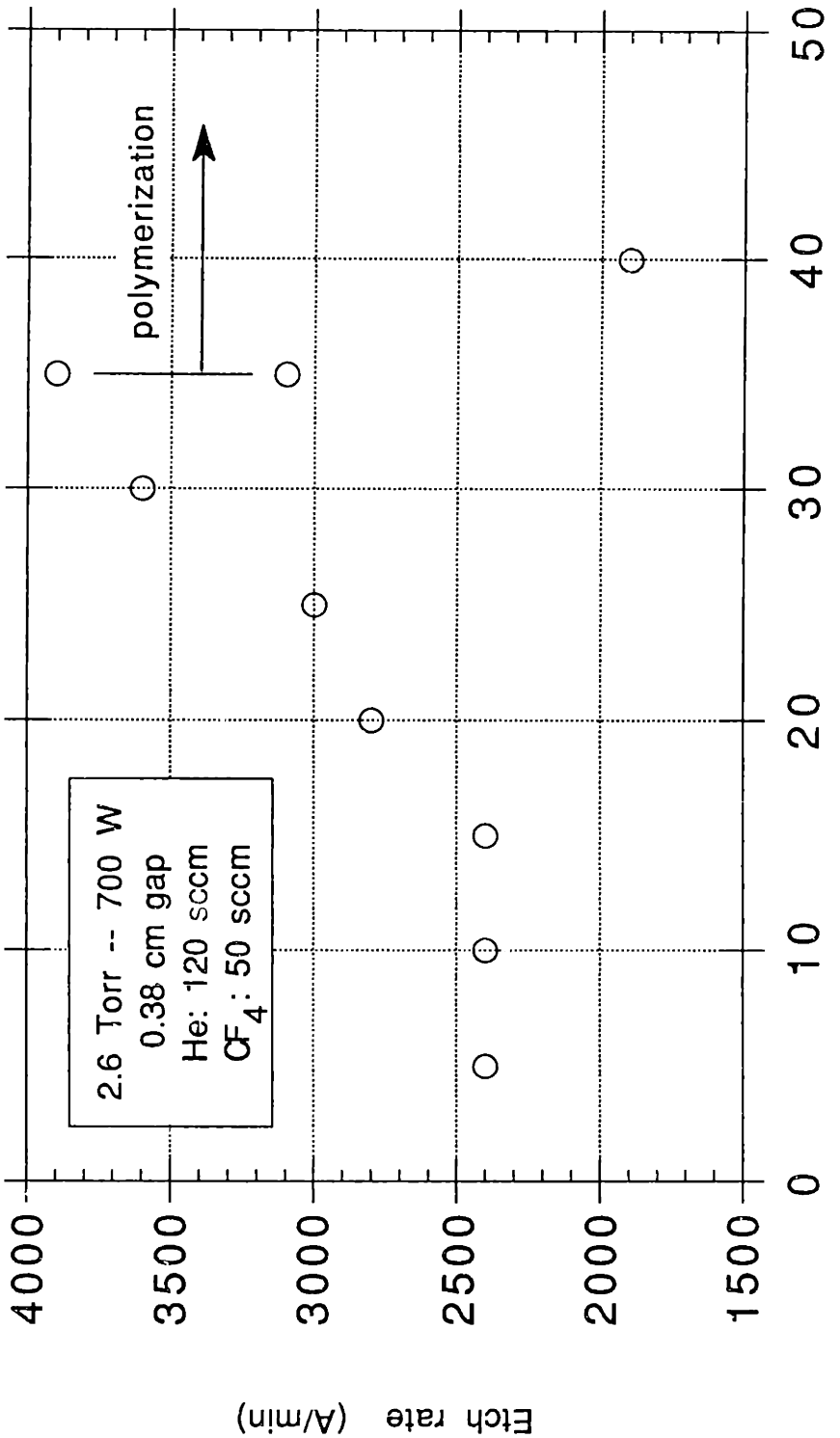

Fig. 28 Sample data for silicon dioxide etching demonstrating polymerization effect

Lam Research Model 594 Plasma Etcher

Pressure	2.0	Torr
Power	900	W
Gap	0.34	cm
He	150	sccm
CHF_3	30	sccm
CF_4	50	sccm

Table 2. Values of final etching parameters

After etching, wafers were ashed in a Drytek Megastrip 6 photoresist stripper. An SEM of etch results is shown in Fig. 29. Inspection of these wafers revealed vertical sidewalls; however, perturbations on the order of 0.1 μm were visible on the sidewall edges. This effect, in conjuction with the inherent leaky design of the waveguide on both wings, contributed to the additional loss seen by the entire structure. For applications where truly efficient light delivery is required, more work must be done on methods to achieve lateral confinement. There appears to be a trade-off involved since deeper etches will offer greater confinement, but also increase the loss due to sidewall scattering. However, since the sensor design described in this work is sensitive to relative loss and not absolute loss, the effect of these scattering losses should only change the baseline output level and not the basic sensor response.

Fig. 29 Scanning electron micrograph of plasma etching results

The fabrication process was continued with work on the second component, the diaphragm wafer. Initially, the diaphragm wafer is simply the support for the microfabricated gap spacer. After bonding the two components together, the structure is then ground down to the desired diaphragm thickness. Steam oxidation of a four-inch (100) double-side-polished wafer at 950° C was used to form the gap spacer, which was fabricated and measured to be 2000 Å thick. This oxide layer was patterned with diaphragms and waveguide access channels using lithographic techniques similar to those used in the processing of the waveguide wafer. Diaphragm wafers were then wet-etched in buffered hydrofluoric acid down to the silicon substrate in order to remove the silicon dioxide from the diaphragm and waveguide access channel regions. After photoresist removal, the diaphragm wafer was complete and ready for bonding with the waveguide wafer.

4.2 Wafer Bonding Technologies

After preparation of the two separate components, attention must be paid to the method in which these two parts are brought together. Since control of the gap spacing is important, the use of adhesives is inappropriate. The possibility of using some form of wafer-to-wafer bonding process was explored. Two major avenues of investigation were pursued: 1) direct wafer bonding, a process by which two wafers with extremely smooth surfaces may be fused together by using the appropriate surface preparations before placing the wafers into contact [86-90], and 2) electrostatic bonding, in which a field across the wafer-to-wafer interface is used to enhance the bonding process, and which is typically performed at elevated temperature [91-94]. These two methods will be discussed in the following sections.

4.2.1 Direct Wafer Bonding

Direct wafer bonding is a technique by which two smooth wafer surfaces can be bonded together by using appropriate surface preparations before placing the wafers into contact. For further details, the reader is referred to the literature [86-90]. The first objective in this study was to determine which sets of materials were acceptable for direct wafer bonding. Unpatterned wafers with at most one additional film were used for these experiments. The direct wafer bonding process used was as follows. Wafers were run through a standard RCA clean cycle comprised of an organic clean (5:1:1 H_2O:NH_3OH:H_2O_2) and rinse, an HF dip (50:1) and rinse, and an ionic clean (6:1:1 H_2O:HCl:H_2O_2) and rinse, followed by a spin-rinse and dry step. It is hypothesized that this process hydrates the surface of the wafer by tying up dangling silicon bonds with hydroxyl groups. Wafers were then immediately removed from the spin-rinse dryer and placed so that their polished sides were in intimate contact, using a specially designed jig to align the wafer flats to one another. The aligned wafers were then pressed into contact first at the center and then at the edges in order to remove any pockets of trapped gas. At this point, successfully bonded wafers would be fused together and could be inspected for voids under an infrared camera. Defects of greater than 0.25 microns in size could typically be seen as ringed fringe patterns in such an inspection system. In this manner, wafers with unacceptable defect densities could be discarded. It is hypothesized that at this stage, hydroxyl groups from the two wafers form hydrogen bonds across the interface. The high temperature anneal (1 hour, 1000° C) typically used after placing the wafers into contact is thought to release water from the interface leaving behind an oxygen bridge. These oxygen atoms can then diffuse away from the interface, leaving behind a robust wafer-to-wafer bond. In the studies performed for this work, all possible combinations of

the following four materials were successfully bonded: bare silicon, silicon dioxide, silicon nitride, and borophosphosilicate glass (BPSG). It was commonly reported in the literature that silicon and thermally grown silicon dioxide were easily used as substrates for direct wafer bonding. However, materials that were deposited using low pressure chemical vapor deposition (LPCVD) techniques, such as silicon nitride and BPSG, were not commonly thought to be amenable to wafer bonding at the time of these investigations. It is now understood that even small degrees of surface roughness can interfere with the potential a wafer has for direct bonding. Certain LPCVD techniques can potentially introduce more surface roughness than thermal oxidation processes and can lead to poor results. However, it was found that wafers with 1500 Å of Si_3N_4 could be repeatably bonded by direct wafer bonding techniques. In addition, some wafers of 6000 Å BPSG films were successfully bonded. In contrast to these results, all attempts to bond wafers fabricated using our process for low-temperature oxide (LTO) were unsuccessful. It is believed that this was the result of particulate formation during the deposition process, which damages the quality of the surface for bonding.

Direct wafer bonding was used to fabricate a prototype of a silicon-diaphragm light-attenuating sensor. This prototype was similar to the device reported in this thesis, but it used a standard silicon nitride slab waveguide in place of the ridge-etched ARROW waveguide structure. In this case, the index of the silicon dioxide was lower than the waveguide effective index. Thus direct radiation into the silicon was not a major concern. Hence, the microfabricated gap spacer layer was bonded directly to the silicon nitride waveguide and no access channels were fabricated. A scanning electron micrograph of this structure is shown in Fig. 30. Test structures using this principle were fabricated by etching away the upper silicon layer from the periphery of the wafer to expose the silicon nitride waveguide as shown in Fig. 31. As a preliminary demonstration of the feasibility of

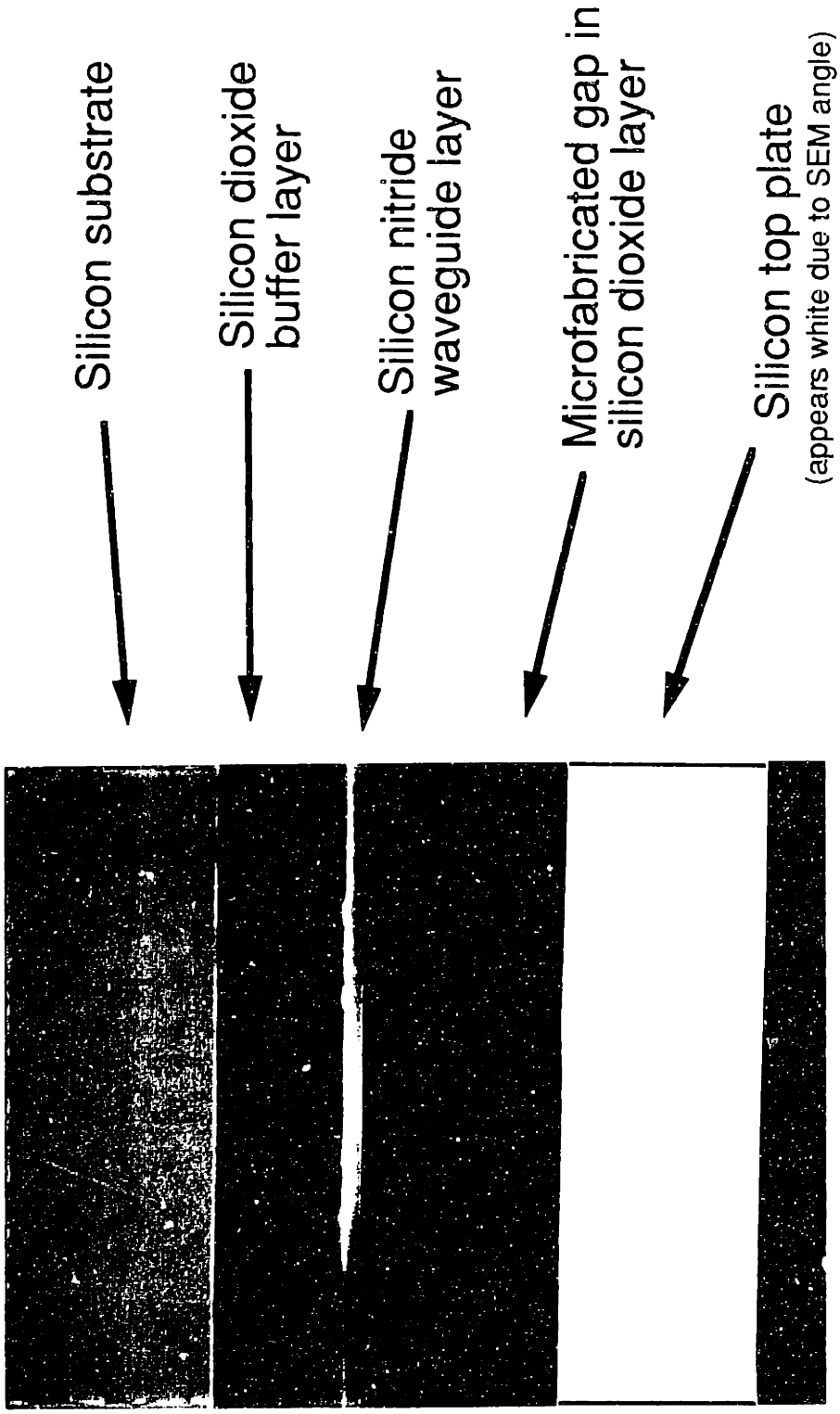

Fig. 30 Scanning electron micrograph of prototype silicon-diaphragm light-attenuator

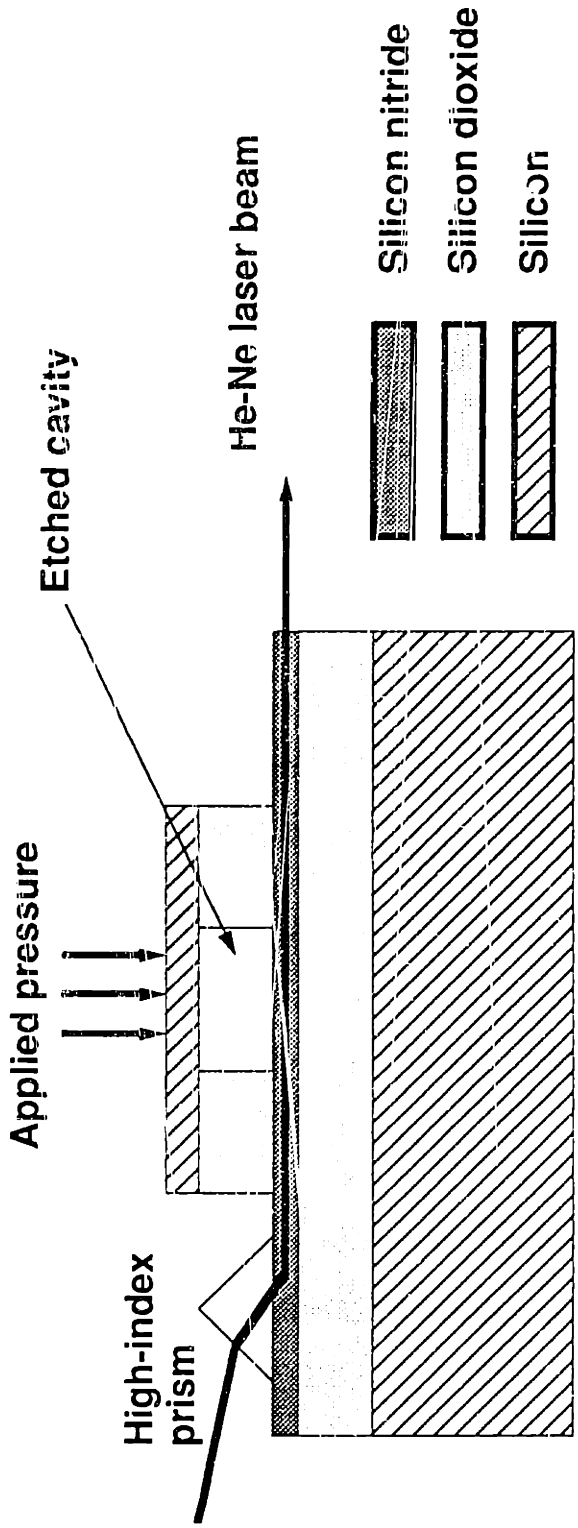

Fig. 31 Schematic of testing arrangement for direct wafer bonded structure

evanescent loss sensing, light was prism-coupled into the nitride layer and the output streak of the test structure was visibly modified by the application of pressure to the diaphragm.

4.2.2 Electrostatic Bonding

The use of the ARROW waveguide structure led this work away from direct wafer bonding, since the LTO films selected for the waveguide core were not amenable to this technique. The methodology initially explored for bonding the wafers together involved etching mating V-grooves at the periphery of the two corresponding wafers, using an optical fiber as a mechanical key for aligning the two components together. This idea is illustrated in Fig. 32. This technique was expected to give alignment tolerances in the 5 to 10 μm range, which would have been acceptable for the initial sensor designs. Although this mechanical alignment accuracy was achievable by manual techniques, the wafers could not be electrostatically bonded because of premature dielectric breakdown across the thin films. A schematic of the electrostatic bonding set-up is shown in Fig. 33. Wafers were sandwiched between two stainless steel pedestals on a hot plate (Thermolyne Inc., Cimarec 2). The wafer backsides were partially etched away with concentrated HF to expose the bare silicon for electrical contact. The apparatus was then heated up to 450° C. Voltage from a high voltage power supply was ramped up in increments of 10V every 30 seconds. For these samples, breakdown was seen repeatedly in the vicinity of 350V, which appeared premature for a dielectric gap spacing of greater than 6 μm. Two mechanisms were postulated for this breakdown phenomenon. The first possibility was the introduction of scratches into the wafer surfaces during the manual alignment procedure, which would create defects that could initiate dielectric breakdown. The second possibility was the breakdown path that exists through the air between the exposed silicon surfaces of the V-

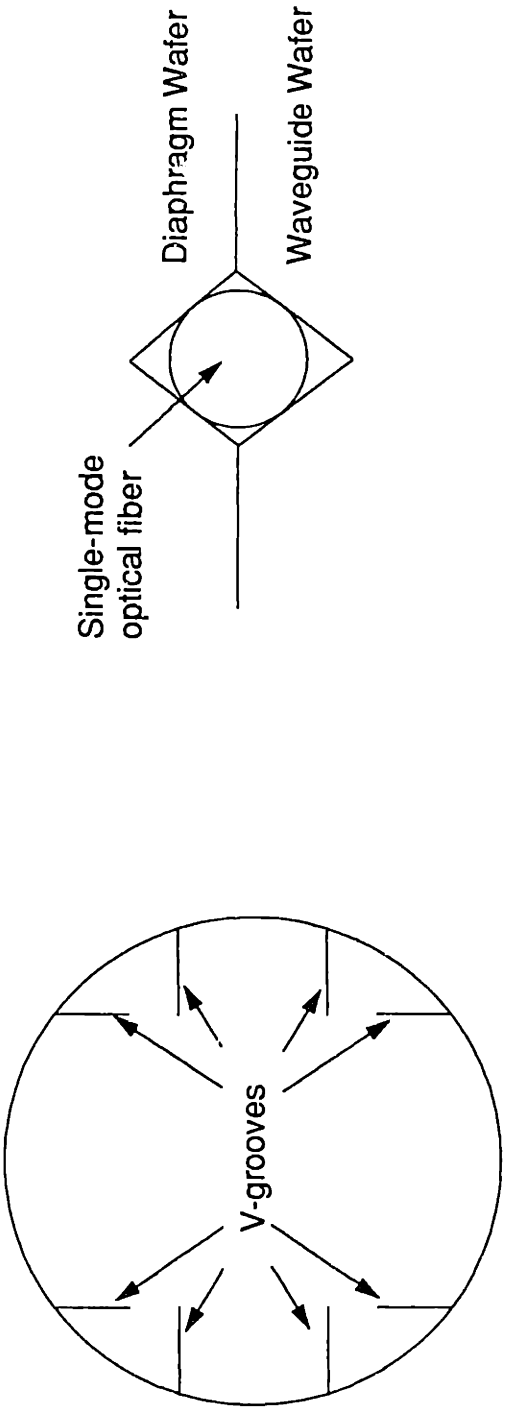

Fig. 32 Conceptual schematic illustrating the use of an optical fiber key with lithographically defined V-grooves, (a) V-grooves etched at periphery of wafer, (b) V-grooves of corresponding wafers mated using optical fiber key

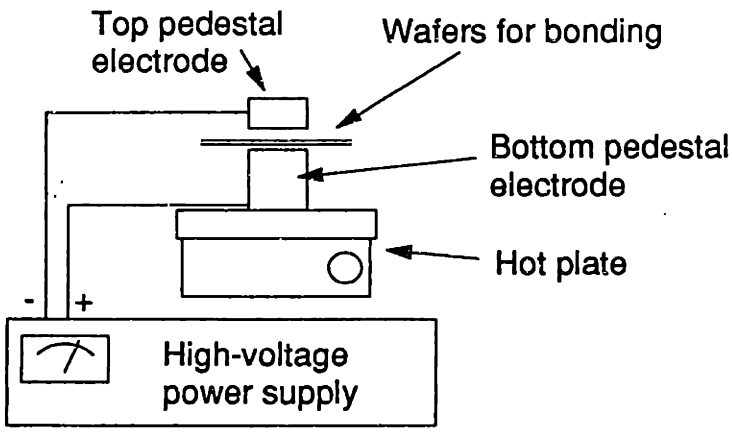

Fig. 33 Hot-plate based bonding apparatus

grooves. Experimental evidence showed that it was possible to bond manually aligned wafers without the fiber alignment V-grooves, and that these wafers were regularly capable of withstanding voltages in excess of 600V. Therefore, it was possible to use manual alignment procedures and not induce catastrophic breakdown. As a result of this observation, it was suspected that the breakdown occurred across the exposed air gap, which was commensurate with the Paschen's curve reported for breakdown dependence on gap spacing. This seems even more plausible given that higher electric fields are expected at the V-groove edges and given that there was some evidence of breakdown seen in scanning electron micrographs ot the V-groove regions. For these reasons, the V-groove alignment marks were removed from the device layout and a chuck was designed to facilitate infrared wafer-to-wafer alignment prior to electrostatic bonding.

A schematic representation of the ideas behind the infrared electrostatic bonding strategy is shown in Fig. 34. The two important components of this strategy are the infrared alignment system and the electrostatic bonding station. This work used a Karl Suss Model MA 4 contact aligner with IR alignment capability and the hot-plate-based bonding apparatus described above. However, as these two systems are not directly compatible with each other, a system was designed to transport wafers from the aligner to the bonding station without disturbing the quality of the alignment. In this method, the standard wafer-holding alignment chuck of the IR aligner was replaced by a horseshoe shaped removable chuck. In addition, the location where the exposure mask would ordinarily be placed was retrofitted with a wafer holder designed to hold the top wafer in place with vacuum pressure. After the wafers were aligned under IR illumination and placed into contact, they were clamped together and transported to the electrostatic bonding station. The horseshoe shape of the bottom chuck allowed placement of the wafers on the pedestal electrode followed by the subsequent removal of the chuck. After wafers were bonded on the apparatus, they were annealed in a high temperature furnace in a nitrogen ambient (1 hr. @ 1000° C). Some wafers delaminated during this process, apparently indicating that the thermal stresses experienced could outweigh the bonding forces generated by using this electrostatic method. It was found that the success rate of this bonding process was greatly improved by adding a thin (~400 Å) intermediary layer of BPSG, which reflows at elevated temperatures, and by applying a pressure load to the wafers to force them into contact. After this annealing cycle, wafers were once again inspected under an infrared microscope to verify the accuracy of alignment. Alignment accuracies of better than 2.0 μm across the entire wafer appear to be achievable with this process.

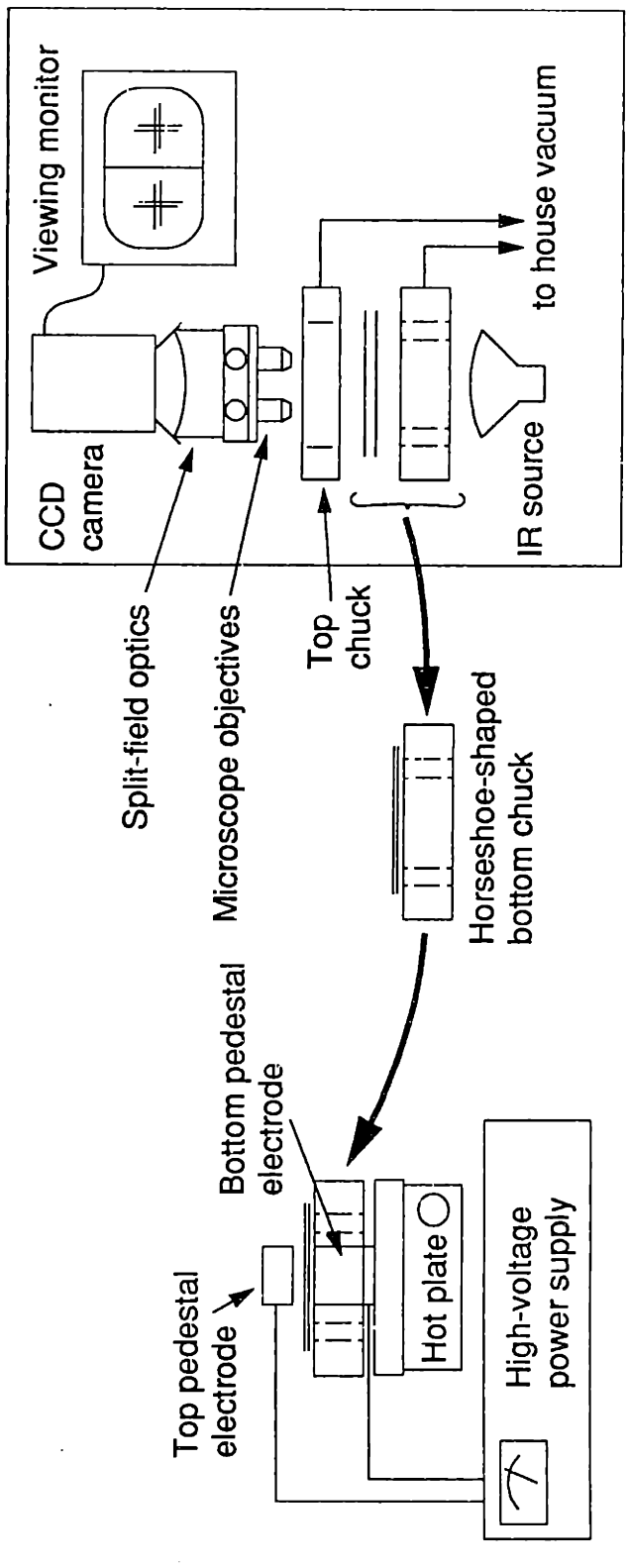

Fig. 34 Schematic of infrared electrostatic bonding strategy

4.3 Sensor Preparation

Fabrication to this point yields a bonded structure that has sixty functional sensing units per wafer. In order to test a sensing chip, it must first be selected and excised from the wafer. Second, the diaphragm thickness of the structure must be adjusted so that the sensor reads out over the desired pressure range. Finally, the end-faces of the sensor chip and the fiber tip must be prepared to be of optical quality. The steps of chip preparation are described in Section 4.3.1. Fiber tip preparation is the subject of Section 4.3.2.

4.3.1 Chip Selection

Chip selection was performed under an infrared camera, since the bonded wafer-pair shows only an unpatterned polished exterior. Each chip occupied an area of 1 cm by 1 cm and could be clearly imaged. The desired chip was then marked under IR illumination by using a tungsten carbide scribe. This chip was cut away from the remainder of the wafer using a Disco Model DAD-2H/5 die saw. Sensor chips were then sent to a grinding vendor (Ceramics Grinding Co., Waltham, MA) for thinning of the diaphragm area. The diaphragm portion of the chip was taken down to a thickness of approximately 100 μm using this method. Chips were then fine polished using standard polishing instrumentation. This grinding and polishing process is abrasive and can introduce roughness at the chip edges, as well as destroying the integrity of the entire structure if attempts are made to thin the diaphragm layer below 100 μm. Since the waveguide end-faces can often be damaged at this point, the preparation of the end-faces required edge trimming using the die saw, which was set to cut entirely through the chip. After edges were trimmed on the saw, manual polishing methods were used to bring the end-face

finishes to optical quality. A serial set of polishes using 15 μm, 3 μm, and 0.3 μm grit paper was used in this case. Inspection of the end-faces under the microscope was found to be critical to evaluation of surface finish. After this final polishing procedure and microscope inspection, chips were ready to be tested for optical modulation in response to pressure. A fully-prepared sample chip can be seen in Fig. 35.

4.3.2 Fiber Tip Preparation

In the conventional method, fibers are cleaved perpendicular to their propagation axis. However, butt-coupling from these types of end-faces is susceptible to mechanical obstruction if the sample end-face preparation is non-ideal. This problem can be alleviated by etching lenses at the fiber tip. The specific procedure described below offers two advantages: 1) the waist of the beam is moved away from the fiber end-tip, and 2) the cladding near the fiber-tip is etched back to a shape similar to that of a pencil point. Both of these results help to reduce the possibility of mechanical obstruction.

This fiber-lensing technique involves immersion of a jacket-stripped fiber in a bi-layer suspension of hydrofluoric acid (HF) and mineral oil. As the mineral oil has a lower density than the HF, it will separate out into a visible layer on top of the HF layer. However, since the HF is highly volatile, a diffusion gradient is set up in the lower region of the mineral oil at the interface to the HF. Since HF is being used to etch the glass of the optical fiber, the portions of the glass completely immersed in the acid will etch at a much faster rate than those exposed to the weaker concentrations of HF set up in the mineral oil gradient. After one hour of etching time, the optical fiber will be sharpened to a tip, closely resembling that of a sharpened pencil. This tip must be rounded off in some manner, since it is too sharp to provide proper lensing action for the fiber. The technique used in the

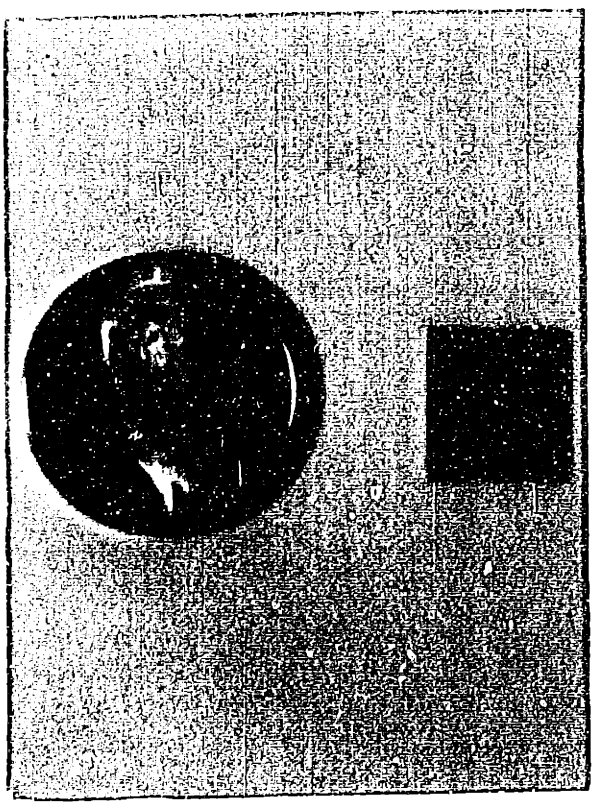

Fig. 35 Photograph of fully prepared sample chip

preliminary experiments of this work used the arc from a fiber fusion splicer to melt and round off the tip of the fiber. However, due to the difficulty in reproducing fringing fields from such an arc, this technique was not pursued further. Experiments reported in Chapter 5 were performed by end-firing a bare laser-beam at the input waveguide end-face of the sensor chip.

Chapter 5

Experimental Results

Prism coupling studies on slab waveguides were performed to compare the waveguiding behavior between standard waveguide and ARROW films. These slab measurements matched theoretical predictions and are described in Section 5.1. Three-dimensional waveguides were then formed by using the ridge-etch procedures described in Chapter 4. A number of studies were aimed at determining the suitability of these waveguides, including a study of the effect of separation on fiber-to-waveguide coupling, a study of transverse translation effects on fiber coupling to a fully packaged chip, and a study on waveguide loss characteristics. These studies are described in Section 5.2. Finally, Section 5.3 discusses how the interaction mechanism itself was investigated experimentally. Initially, there was difficulty in obtaining modulation of the chip signal with the 80 psi compressed-air loading scheme originally designed. Other experiments were performed to verify that the waveguide behavior was indeed as expected. First, light was extinguished experimentally on an ARROW waveguide by using a topically applied index matching fluid. Then a glass attenuator was used to enhance the leakage effect in order to see the optical modulation. Finally, a modified loading scheme was developed using a high-force piezoelectric actuator to drive the diaphragm into deflection. Using this

strategy, modulation of the optical output was seen and the behavior observed was attributed to particle contamination in the gap region. A brief analysis of the expected impact of particulate contamination is presented, as well as a possible model for simulating these interactions.

5.1 Prism Coupling Testing

Prism coupling was first described by Tien [95] and is now one of the primary diagnostic tools used in the characterization of optical waveguides [96,97]. A schematic of the prism-coupling method is shown in Fig. 36. This method consists of bringing a high-refractive index prism into close proximity with the dielectric film under test. In these tests, which were performed on a commercial instrument (Metricon PC-2000), this was accomplished by sandwiching the test sample between the prism and a coupling head that was driven by compressed air. Typically, a spot appears where the gap between sample and prism is very small, indicating the presence of evanescent coupling. A laser beam is directed at this spot through the prism, and its angle of incidence is varied by rotating the entire sample holding assembly. Reflected light is monitored as a function of incident angle using a large-area photodetector. Even though the incident beam impinges at angles greater than the critical angle for the prism-air interface, frustrated total internal reflection makes it possible for power to be transmitted to the waveguide below. The transmission of power depends on the phase-matching of the incident beam with the supported modes of the dielectric structure and can be seen as power dips in the reflected intensity versus angle curves. From the position of these dips in power, one can determine the effective index of the modes of interest as well as the thickness and index of a standard waveguiding film. A good discussion of prism coupling theory can be found in the text by Lee [97].

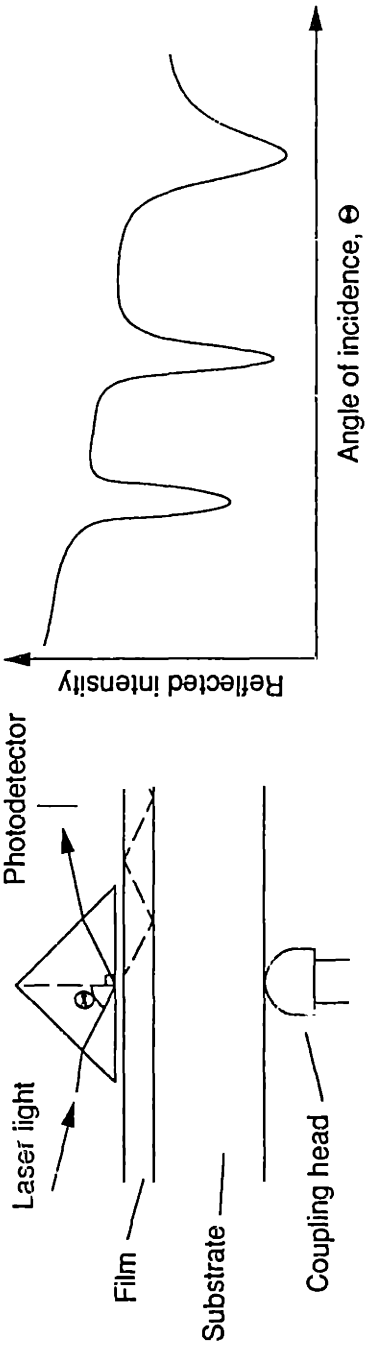

Fig. 36 Schematic of the prism-coupling method

In order to compare and contrast the characteristics of standard nitride waveguides with ARROW waveguides, prism coupling data from two samples are shown in Figs. 37 and 38. Fig. 37 shows a prism coupling scan from a standard waveguiding geometry consisting of 1500 Å of silicon nitride deposited on 1.4 μm of silicon dioxide. The sharp peak at the center corresponds to the guided mode and an effective index of 1.670 as predicted. Fig. 38 shows the corresponding scan from an ARROW waveguiding sample as described in the previous chapter. The small sharp peak at the left of the peak structure corresponds to an effective index of 1.455 and represents the fundamental ARROW mode. In both scans, the other power dips correspond to modes with lower values of effective index, i.e. oxide modes and higher order ARROW modes. For example, the strong dip adjacent to the fundamental mode in the ARROW waveguide scan indicates coupling to an oxide mode that is far removed from the prism surface. The measured effective index of the ARROW waveguide was much lower than that of the standard silicon nitride waveguide. This again demonstrates the advantages that ARROW structures have regarding index-matching to optical fibers. Waveguiding streaks were observed at the appropriate angles for both samples during prism-coupling, which confirms the fact that transfer of power will occur to the guiding layer under the proper conditions.

5.2 Experiments on Three-Dimensional ARROW Waveguides

Experiments were performed to quantitate the suitability of the ARROW waveguides for improving alignment as well as to determine the types of losses that might be expected from a three-dimensional ARROW structure.

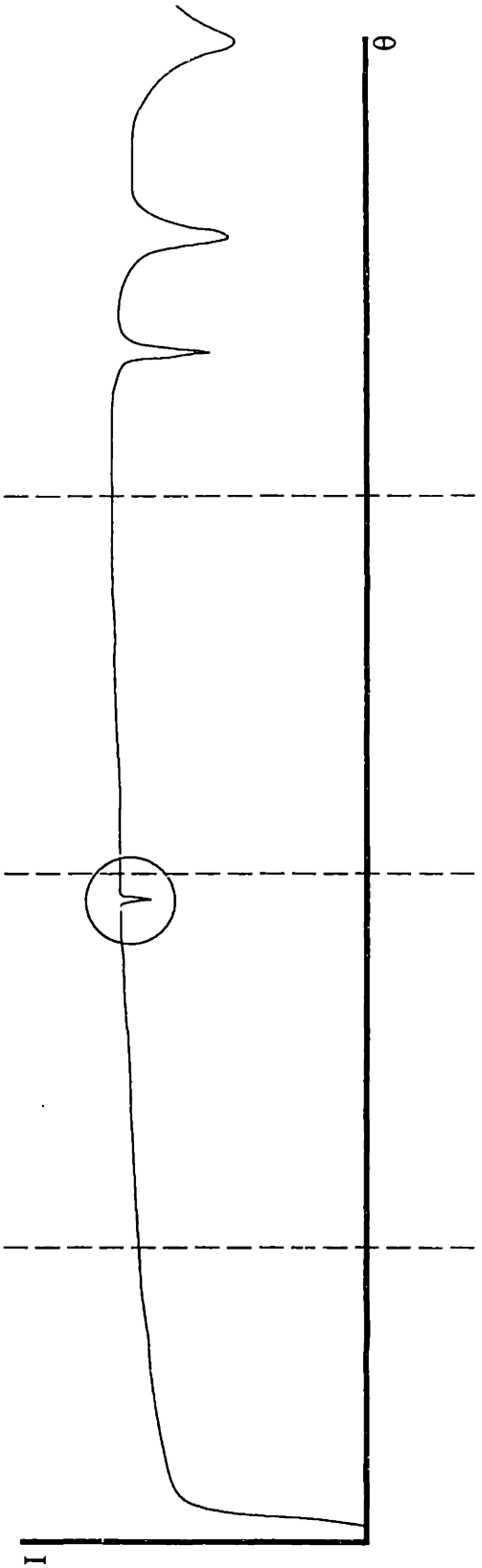

Fig. 37 Prism-coupling scan from standard waveguide

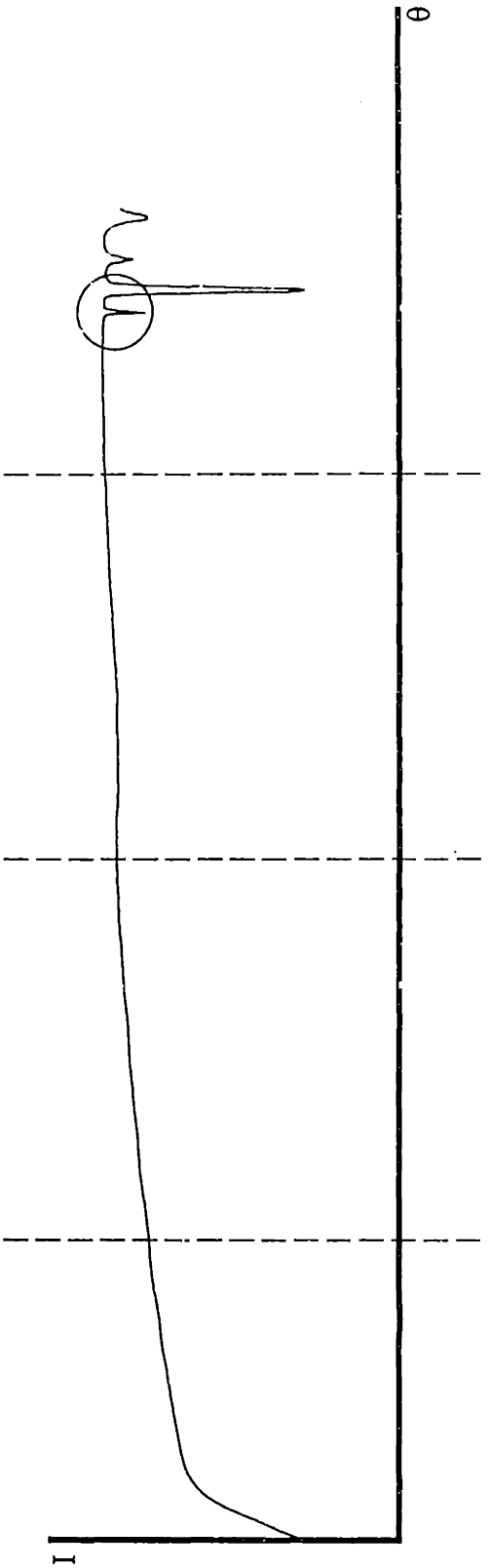

Fig. 38 Prism-coupling scan from ARROW waveguide

5.2.1 Fiber-to-ARROW Coupling

Two different types of coupling experiments were performed using independent experimental set-ups. In the first experiment, coupling efficiency from an optical fiber to an exposed ARROW waveguide was monitored as a function of separation distance between the two. A schematic of the experimental set-up is shown in Fig. 39. Data from this test is shown in Fig. 40. A half-width half-maximum of 40 μm is found, which is in good agreement with the predicted results from Section 2.2.

In the second experiment, a laser was used to end-fire light into an ARROW waveguide inside an assembled sensing chip as shown in Fig. 41. The chip was mounted on a piezoelectric actuator and its light throughput was monitored as it was translated in the direction transverse to the beam. The piezoelectric transducer was calibrated for free displacement versus applied voltage using measurements taken in a WYKO interferometer system. These results are shown in Fig. 42. A plot of transmission efficiency as a function of piezoelectric voltage is shown in Fig. 43. From this information, the full-width half-maximum for the coupling is determined to be approximately 4 μm, as expected from theory.

5.2.2 ARROW Waveguide Loss Testing

In low-loss ridge-etched waveguides, the surface roughness induced by etching is in a region of low field strength. However, since the ridge-etch used in this work introduces roughness into the waveguide sidewall which experiences strong interaction with the propagating wave, the total amount of loss incurred by such a structure is an issue of concern.

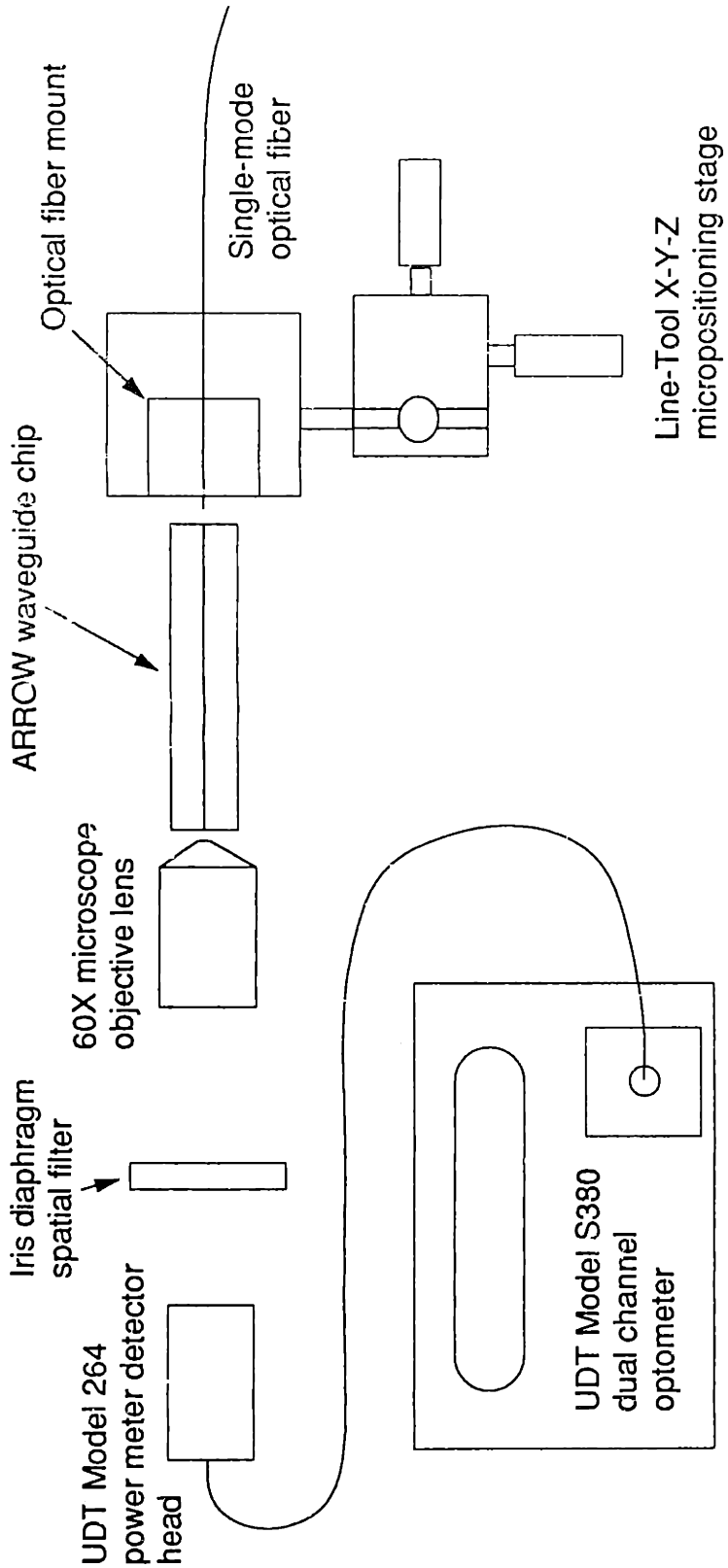

Fig. 39 Schematic of experimental set-up for fiber-to-waveguide separation testing

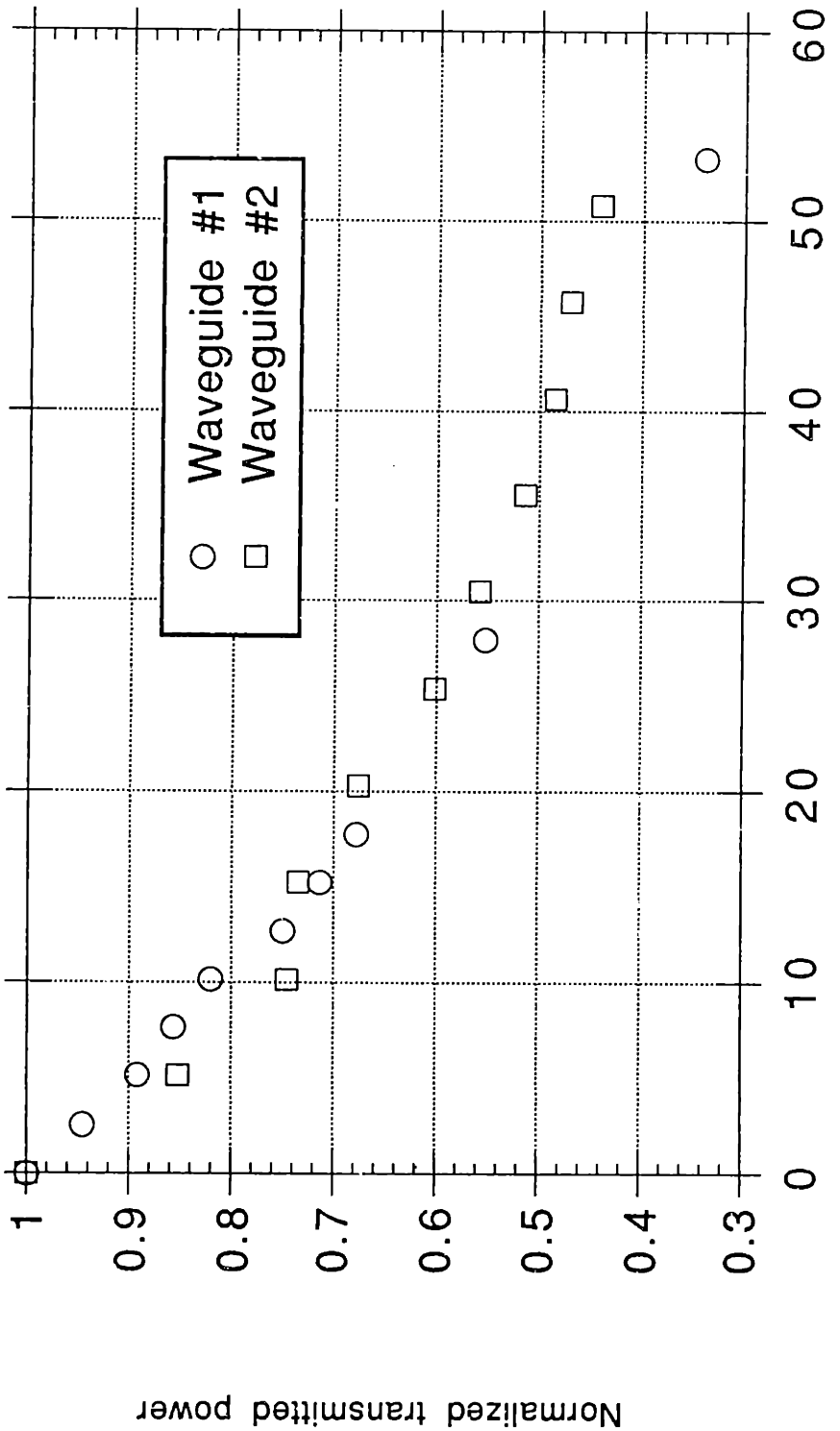

Fig. 40 Normalized transmitted power vs. fiber-to-waveguide separation

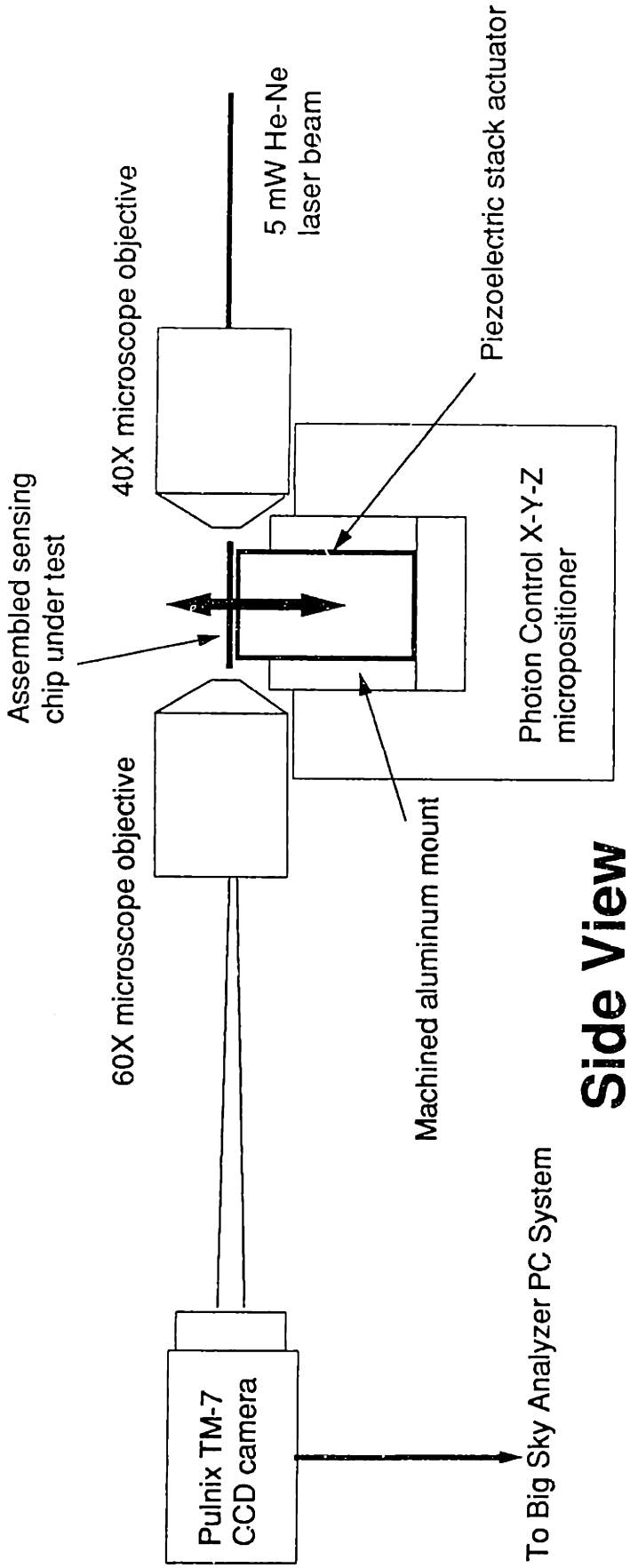

Fig. 41 Schematic of translation test set-up

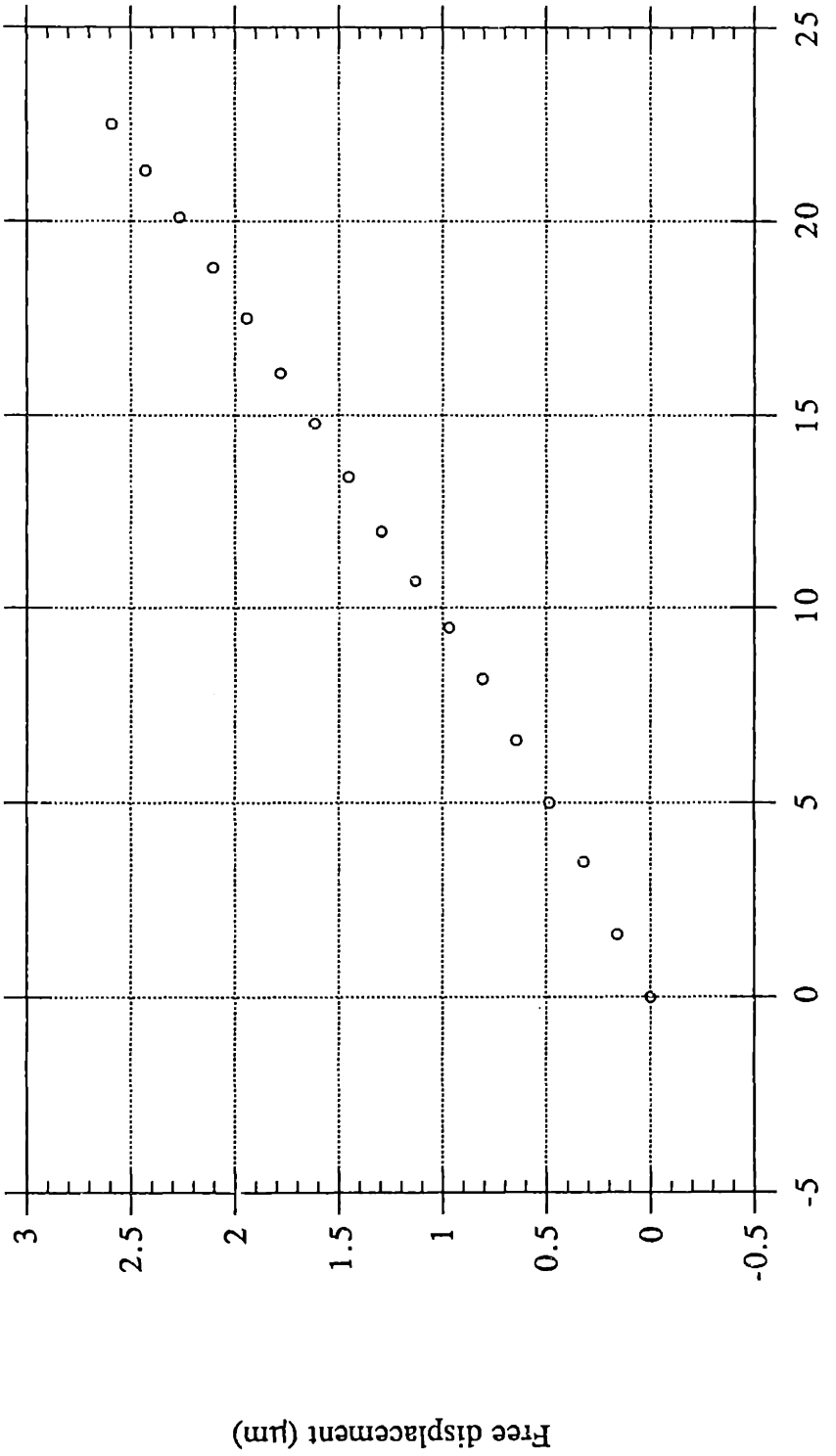

Fig. 42 Piezoelectric stack calibration

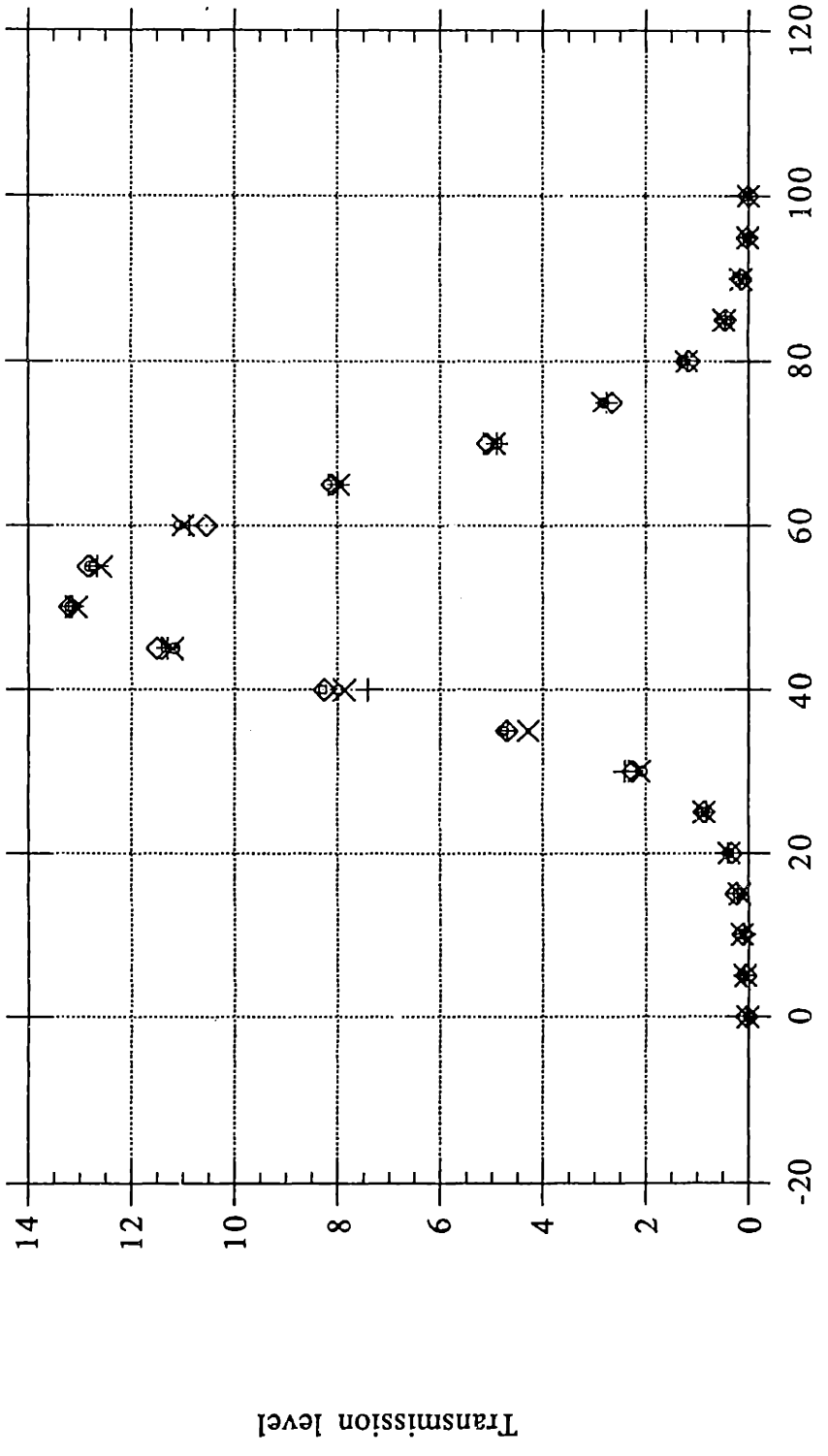

Fig. 43 Transmission of a piezoelectrically translated ARROW waveguide

Loss testing on the ARROW structures was performed by the cut-back method. These tests began with a measurement of transmsitted power through a waveguide sample 5 cm in length. The transmitted power was then remeasured as successive sections of waveguide, 0.5 cm in length, were cleaved off from the far end. Differences in power output were attributed to the sections of waveguide that were removed. This method required re-alignment of the optical fiber to the waveguide by throughput maximization and a visual verification of mode profile prior to taking each measurement. Verification of the ARROW mode was performed by expanding the near field patterns by approximately a factor of 500. The rounded spots observed indicated the presence of the ARROW mode. Coupling into the nitride mode has been shown to result in more elongated mode-patterns. Each measurement was converted to a loss value relative to the initial power throughput. These loss values are plotted as a function of multiples of cleave length in Fig. 44. An intrinsic loss of approximately 3 dB/cm is extracted from this plot. Variations in the data result from re-alignment error, waveguide surface imperfections, and end-face cleavage roughness. The worst case loss is estimated to be approximately 8 dB/cm. This indicates the presence of a high quality sidewall, and validates the plasma etching procedure used in device fabrication. While these loss levels are not adequate for long distance optical communication, they are certainly sufficient for the requirements of building an optical sensor.

5.3 Modulation of ARROW Waveguide Output

The experimental verification of 3D-ARROW waveguide behavior was discussed in the previous section. Here, experiments are discussed which deal with the modulation of

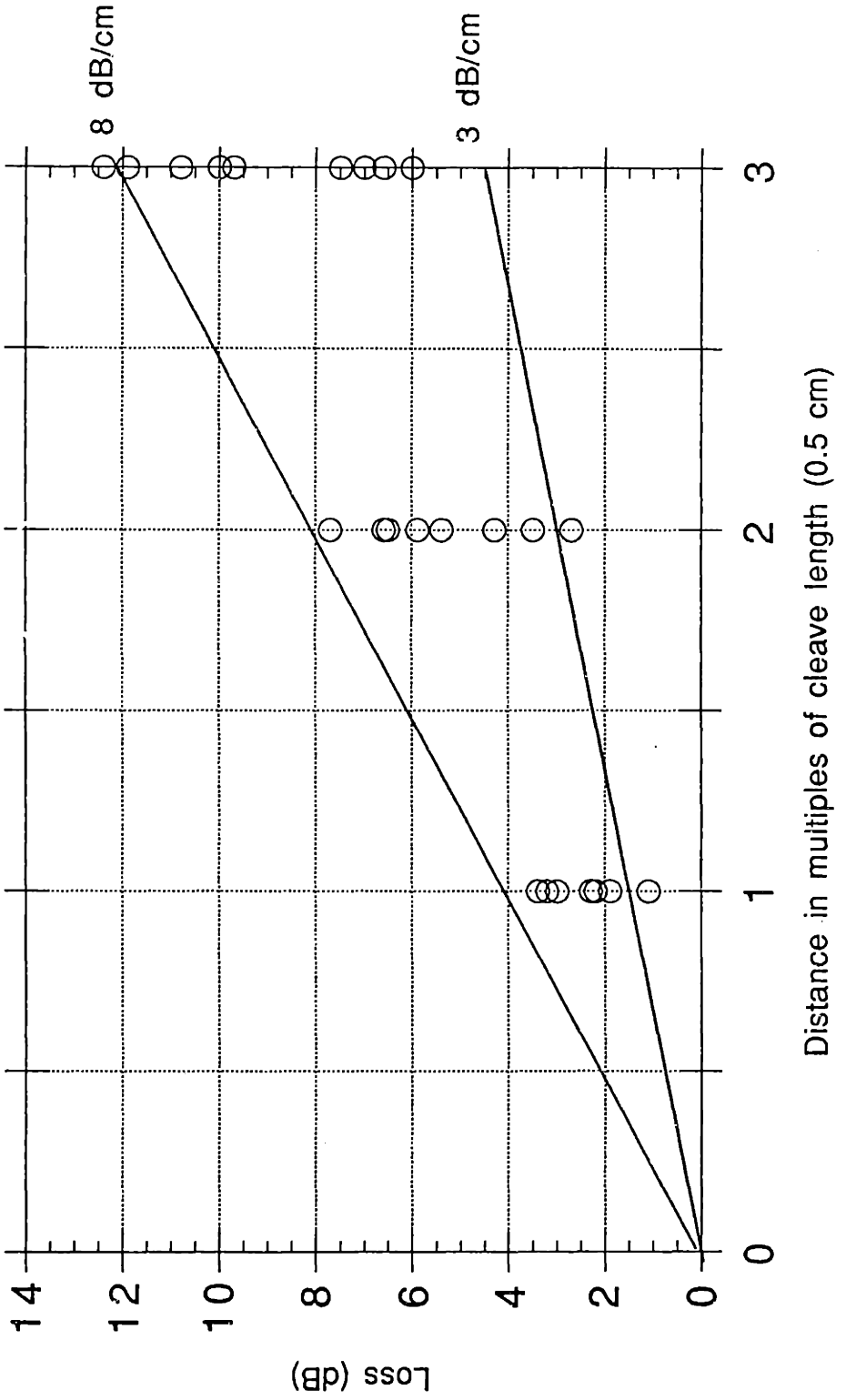

Fig. 44 Plot of waveguide loss vs. cleave length

the waveguide output by proximity-effect leakage enhancement. The optical set-up used for these experiments is shown in Fig. 45. Linearly polarized laser light (λ = 6328 Å) is launched from a 5 mW He-Ne laser source. Selection between TE and TM mode excitation is performed by passing this beam through a half-wave plate that has been rotated to select the desired orientation. This beam is then focussed down into the waveguide using a 40X microscope objective lens that has been mounted on a Line-Tool X-Y-Z micropositioning stage.

The waveguide chip is mounted on an aluminum mount designed to provide access for the microscope objectives used in input and ouput coupling. This mount is in turn mounted on a Photon Control X-Y-Z stage to allow accurate positioning of the waveguide relative to the incoming beam. The beam is coupled out from the far end of the chip using a 60X objective lens mounted on another Line-Tool X-Y-Z stage. Unwanted polarizations can be filtered out using a polarizing filter. The beam is then sent to a Pulnix TM-7 CCD camera which passes its data to a Big Sky Analyzer PC system. This system contains a frame grabber mounted in a 386-based PC-compatible computer and includes extensive beam diagnostic software. For checking quantitative measurements, the beam can be split out to a power meter detector head (UDT Model 264) attached to a dual channel optometer (UDT Model S380).

The sensor chip was designed for full scale operation over a 0 - 50 psi range. For this reason, a pneumatic loading scheme was designed so that compressed-air pressures of up to 80 psi could be delivered to the sensor chip. The design of this testing apparatus is shown in Fig. 46. House compressed-air was fed through a regulator valve and sent to both a calibrated pressure transducer (Omega Model PX603-100G5V) and a pressurization head which could be mounted directly over the sample chip under test. A drawing of this head is shown in Fig. 47. A Buna-N O-ring is used to seal the area around the diaphragm

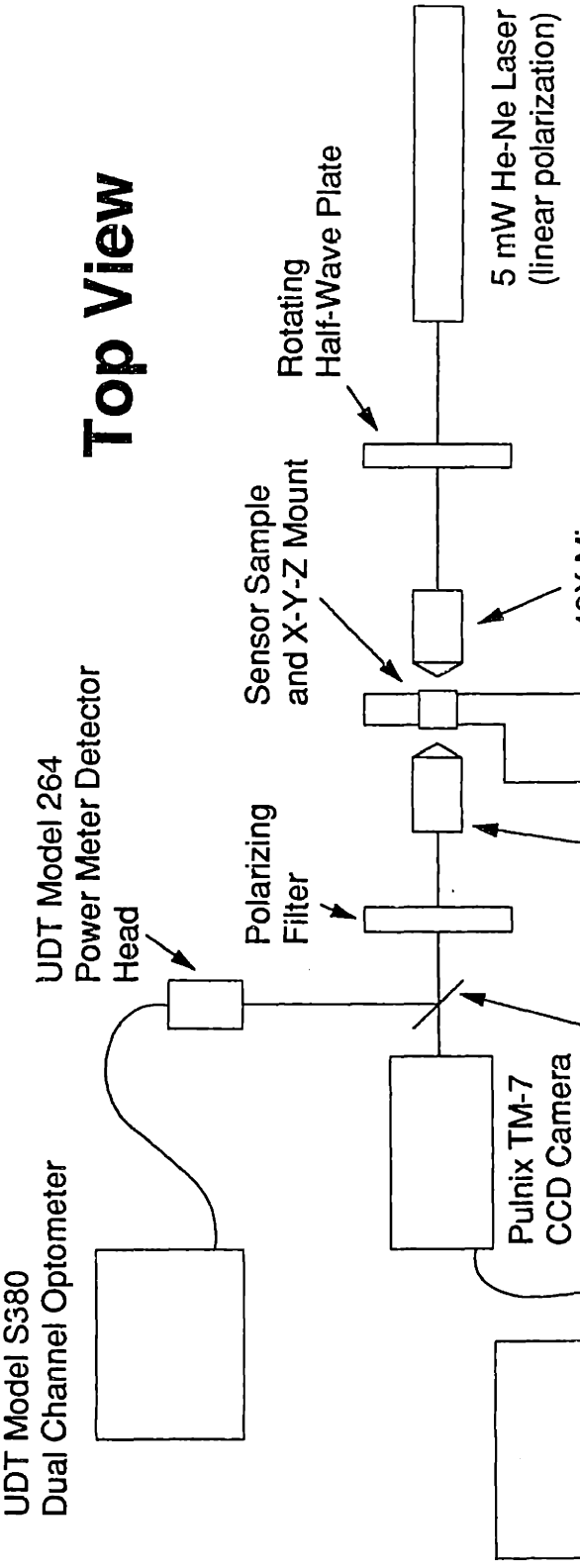

Fig. 45 Schematic of waveguide modulation test set-up

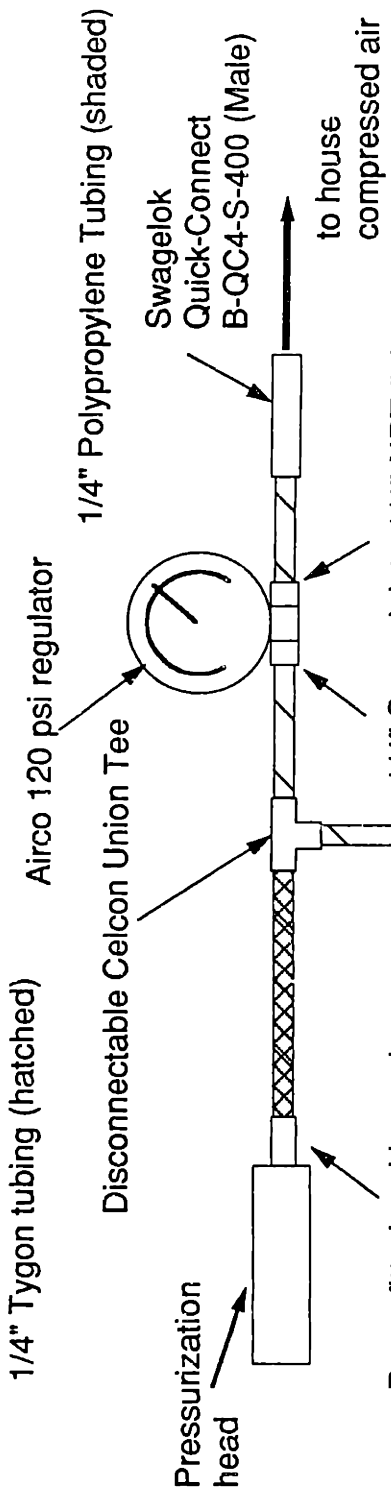

Fig. 46 Schematic of pneumatic testing apparatus

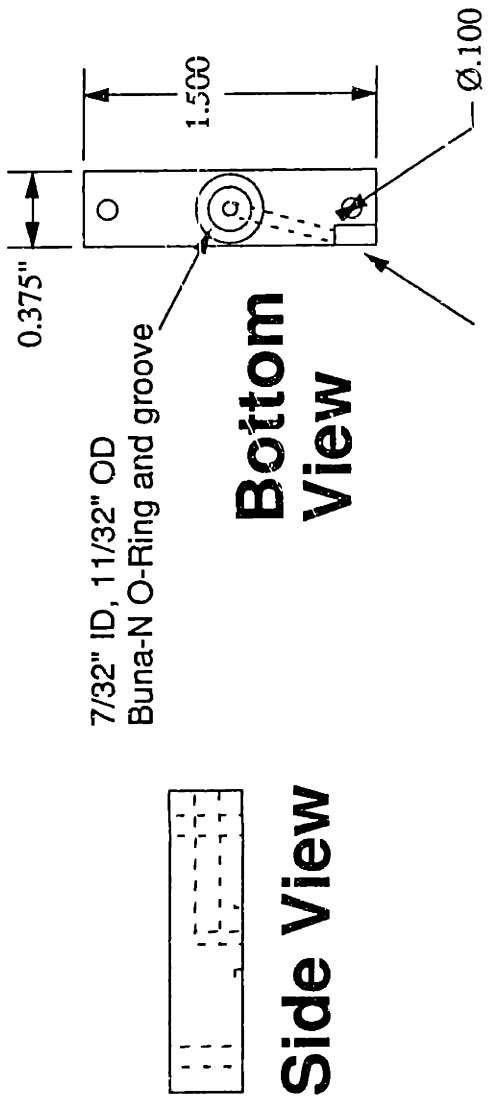

Fig. 47 Pressurization head design

as the pressurization head is clamped to the mount beneath the chip. Pressure is brought in to the head through a brazed Swagelok fitting. Pressure lines were made of flexible tubing to decouple any effects of line straightening or movement from the head itself. Unfortunately, no discernible shifts in waveguide output were detected up to the maximum allowable 80 psi.

However, experience with the silicon nitride waveguide devices described in Section 4.2.1 indicated that modulation should be possible using the leakage enhancement effect. This prompted brief studies into whether the ARROW structure as fabricated was itself the problem. To verify whether light could be forced to leak out of the waveguide using the application of a topically applied fluid, low index gels (n=1.5 and 1.6) were applied to the surface of the waveguide. It was observed that the light leaked out quickly at the first point where it encountered leakage enhancing fluid. This ruled out the possibility that the light might be tightly confined within the core and would not be suspectible to change by outside perturbations. Since the loss of light from the guide was confirmed using these techniques, this avenue was not pursued further. Additional work on the use of fluids to remove light from a waveguide core has been reported by Sorin [30].

Since the chip as designed offered only a limited range of attenuation, one way to make the modulation effect more observable would be to enhance the interaction of the attenuator with the waveguide. To this end, a glass attenuator was introduced which was supported above the waveguide by two 16 μm aluminum shims at the edges of the chip and parallel to the waveguide as shown in Fig. 48. This design allowed for a much longer interaction length between the two components as well as a heightened leakage effect due to the low index of refraction of the glass attenuator (n = 1.5). Since pneumatic loading was no longer appropriate, the loading scheme was replaced with a piezoelectric actuator which was capable of delivering high force. The drawback of this scheme is that unlike the

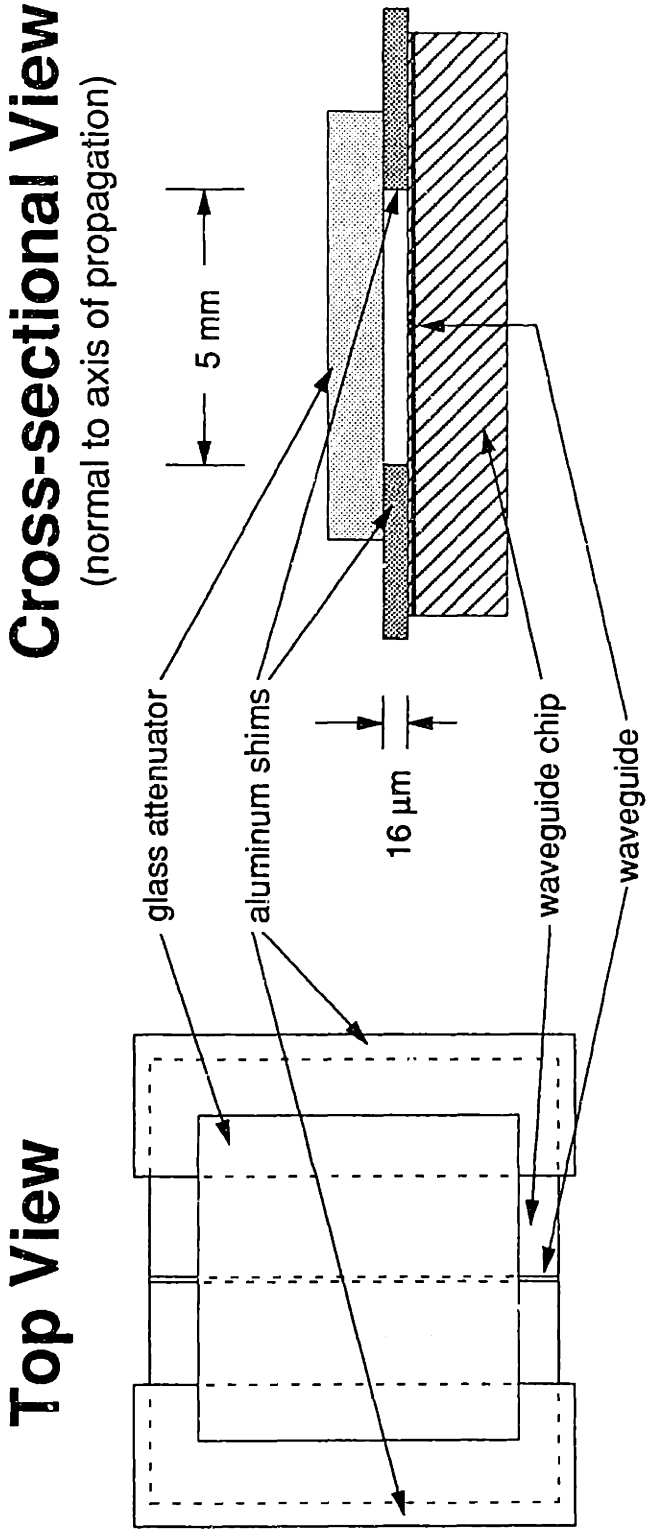

Fig. 48 Glass attenuator experimental set-up

pneumatic method where one knows the pressure and force being applied to all areas of the chip, the piezoelectric element is difficult to accurately localize, both in the x-y plane and in the z-dimension. To circumvent this problem, multiple data sets were taken for each experiment. The flat initial portion indicating no applied load was used as a reference. Data sets that lacked this reference marker were ignored. Those showing the greatest interaction were assumed to be closest to being optimally positioned to effect modulation of the waveguide output.

Initial experiments with the glass attenuator used the loading scheme shown in Fig. 49. In this design, a piezoelectric stack was coupled to a mounted ball bearing which was used to drive the diaphragm into deflection. The initial position of the stack was set using a set screw that could be fixed into position using a locking nut mechanism. Using this ball bearing approach, data sets such as Fig. 50 were obtained. It is important to note the different regions of operation which are illustrated in this figure: at low voltages (0 - 20 V) there is a flat region which serves as a reference marker, at intermediate voltages (20 - 40 V) there is a sharp drop in transmitted power corresponding to expected sensor operation, at high voltages (> 40 V) the ball bearing is driven elastically to create a greater contact area, but the degree of attenuation slows down dramatically. It is important to note that although optical modulation was achieved, it was not possible to get complete extinction of the optical signal with the ball-bearing loading scheme described above. Modelling of the test structure using mechanical simulation methods demonstrated the problem. Since the glass was only being loaded by a point source, the free edges of the glass were far removed from the waveguide surface. Since strong leakage is only expected for gap spacings of less than 0.05 μm, the effective distance of interaction was very small. An optical simulation of the entire structure showed that a complete extinction was not expected for this geometry.

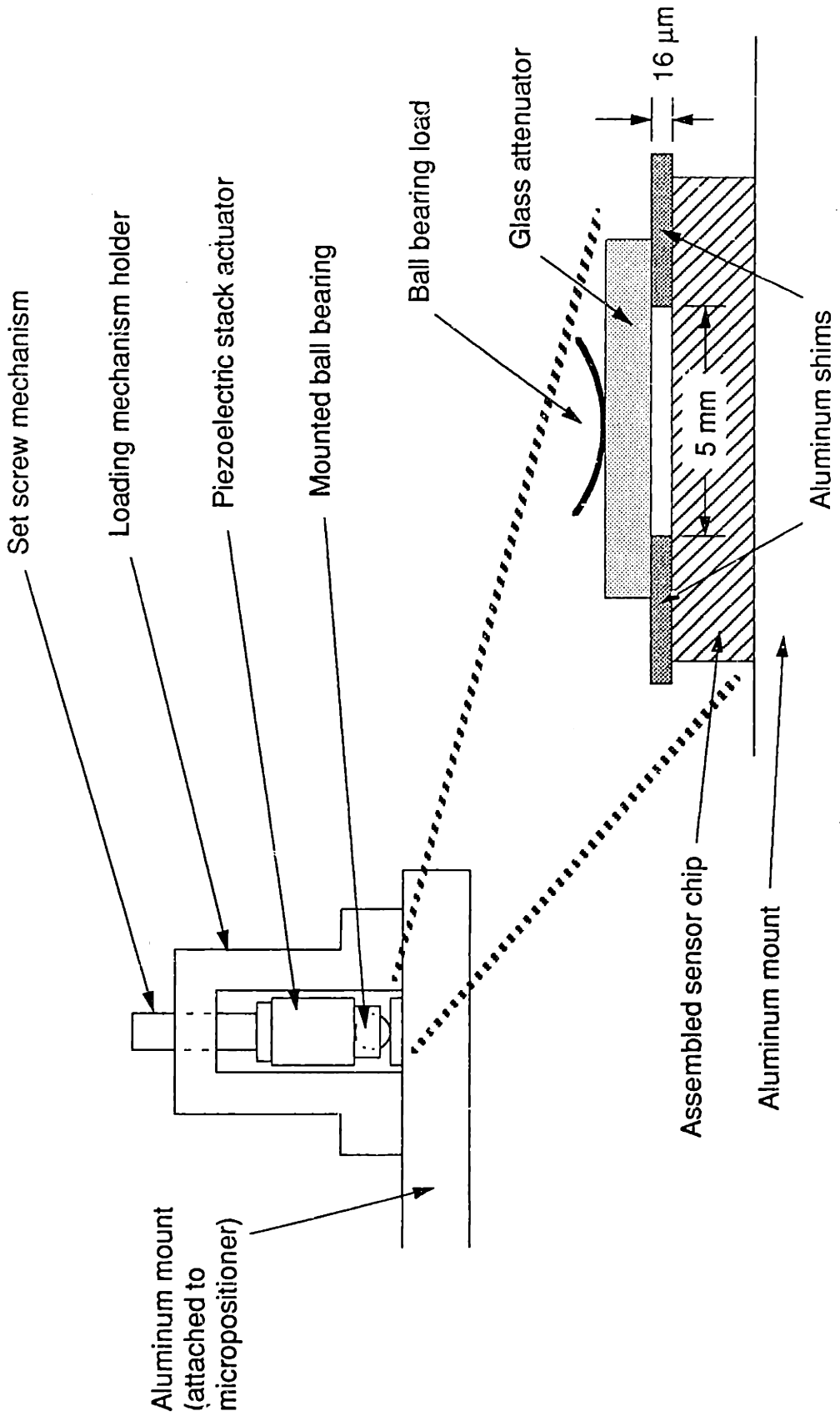

Fig. 49 Piezoelectric stack actuator loading scheme for glass attenuator testing

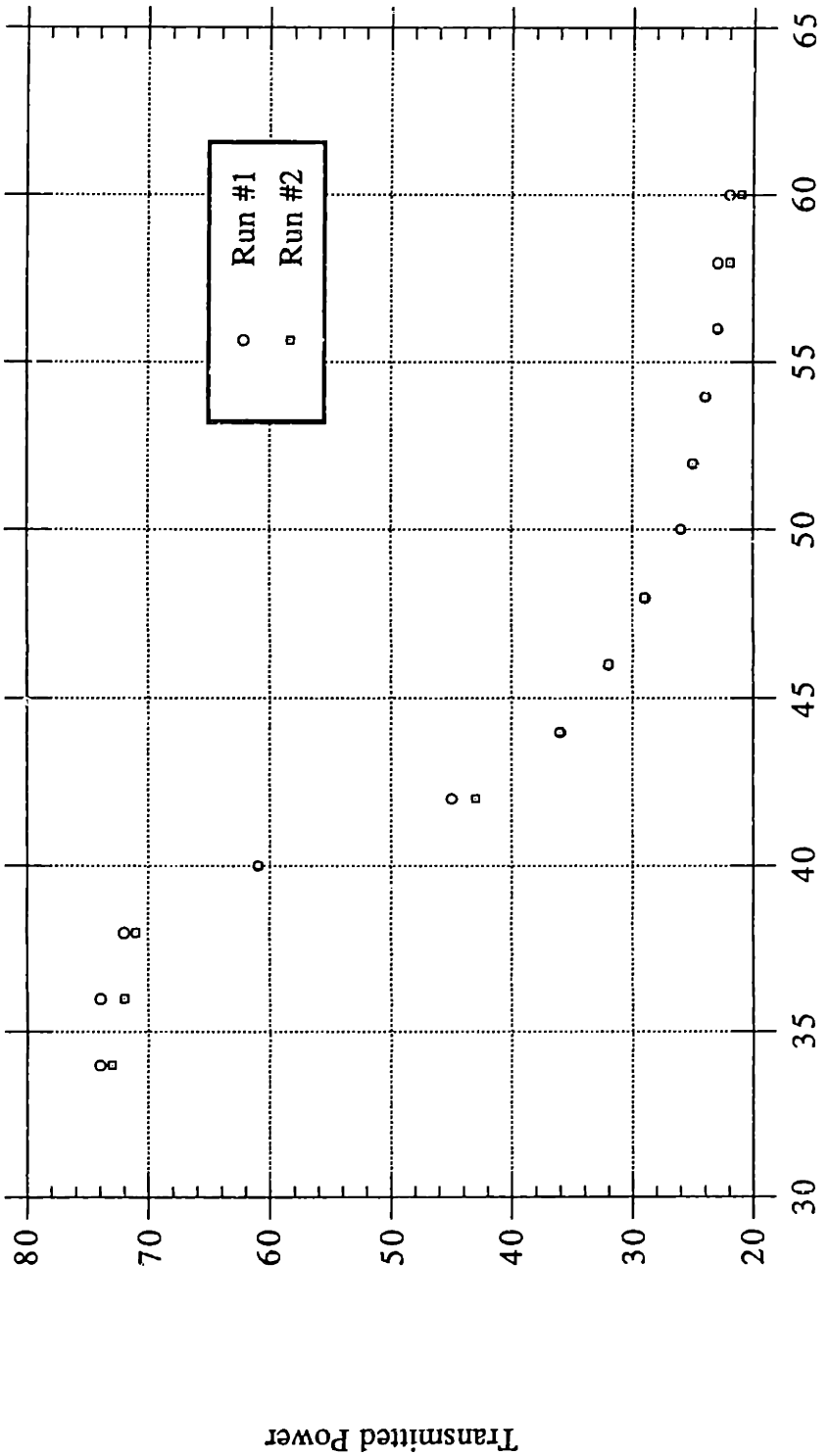

Fig. 50 Effect of piezoelectric actuation on transmitted power

This hypothesis was tested by replacing the ball-bearing point with a triangular-prism edge loading scheme. This scheme effectively used the entire length of the glass as a line of contact, thus enhancing the interaction between the two components greatly. As can be seen in Fig. 51(a), the optical power was fully attenuated using this method, but not without considerable force applied from the piezoelectric stack. Fig. 51(b) shows the results of a calculation of the effective separation between the glass attenuator and the ARROW waveguide. This calculation uses an interaction model based on the simulation results of Section 3.3 and the assumption of perfect edge-loading. It can be seen that the change in effective separation with respect to piezoelectric voltage is much slower than anticipated. This observation led to the initial hypothesis that particles and surface roughness in the gap region were inhibiting the interaction between the two components.

However, there was hope that a chip assembled under clean room conditions would not show these particle contamination effects, and fully packaged chips were tested to see if they would be free from these problems. Chips were tested using the piezoelectrically driven ball-bearing set-up described above. As expected, applying voltage to the piezoelectric stack resulted in decreased intensity at the sensor output as shown by the contour plots in Fig. 52. These plots demonstrate that the understanding of the basic sensor behavior in terms of simple light attenuation is valid. A plot of total transmitted power as a function of applied voltage is shown in Fig. 53. Although not as pronounced as the case for glass, there are once again three distinct regions: a region which corresponds to free piezoelectric displacement, a region which corresponds to deflection of the diaphragm until it makes contact with the ARROW waveguide, and a region which corresponds to the elastic bending of the components under high load. It is important to note, however, that the voltage required to bring the diaphragm into contact with the waveguide appears to be much higher than that predicted by the basic theory. This fact,

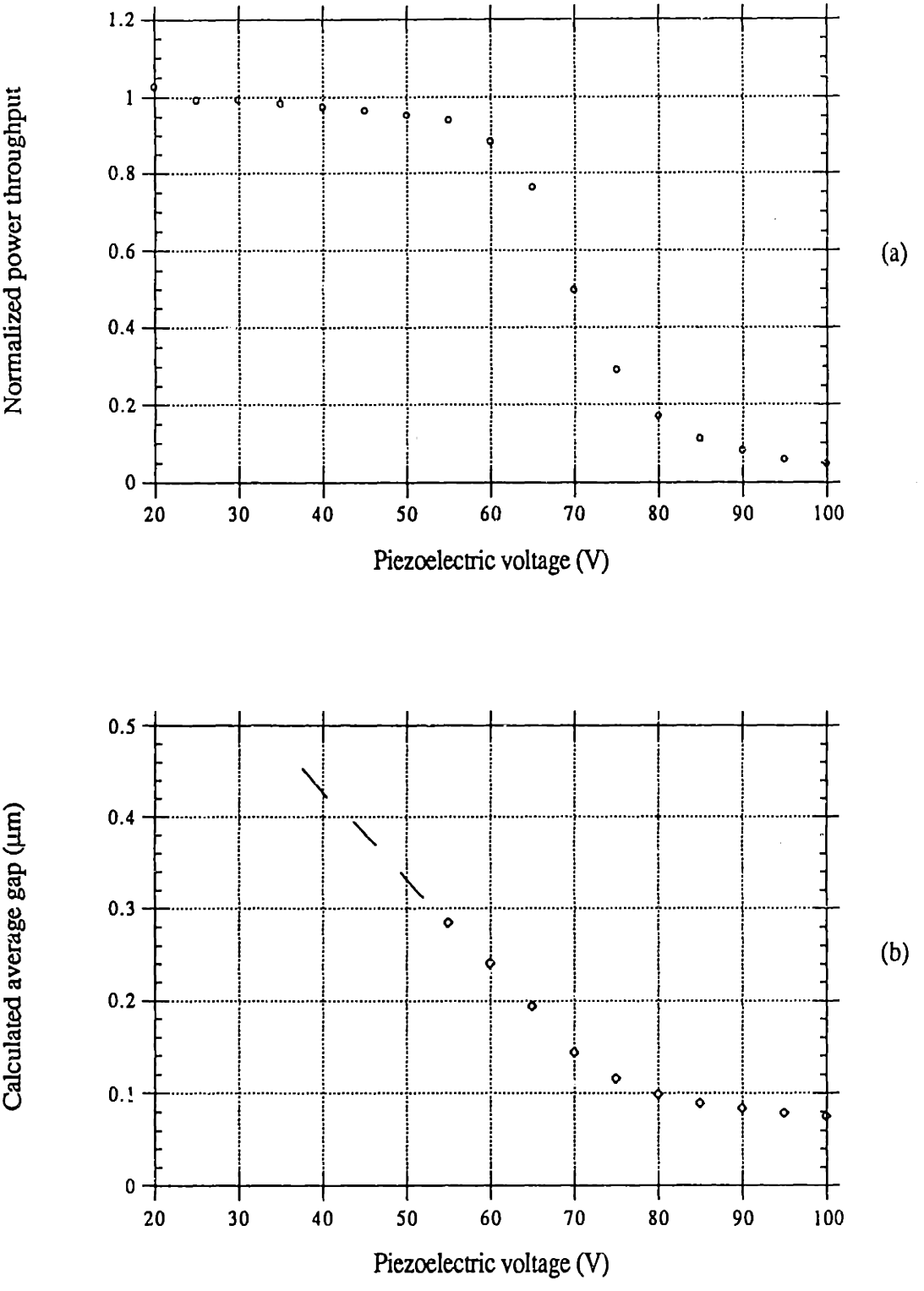

Fig. 51 Effect of triangular-prism edge loading, (a) throughput power vs. voltage, (b) calculated average gap vs. voltage

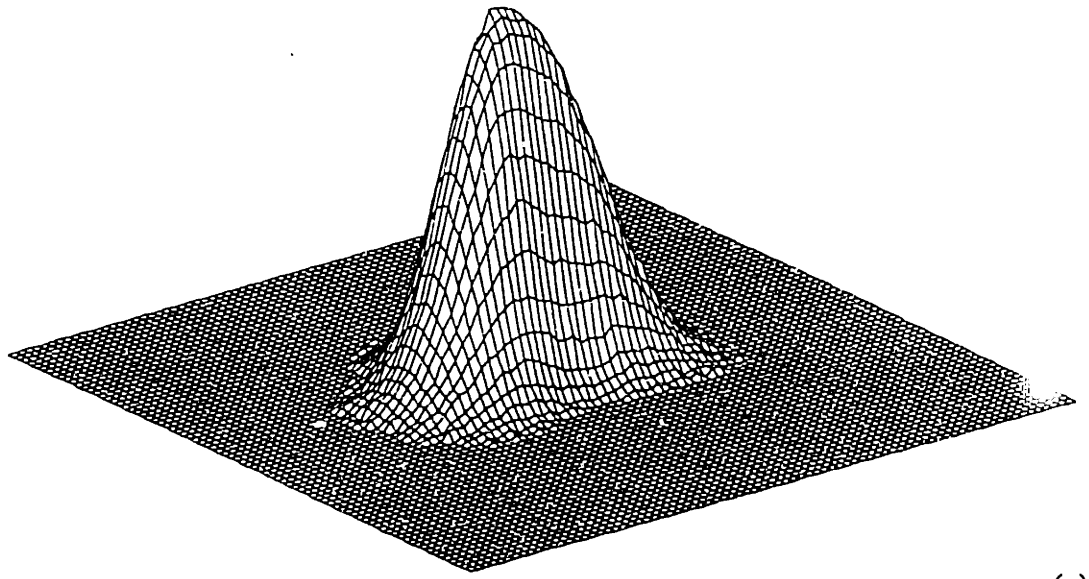

(a)

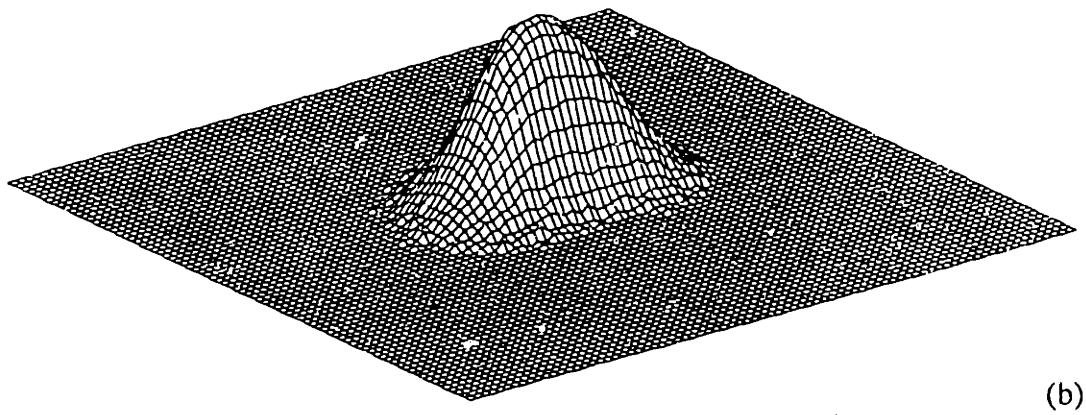

(b)

Fig. 52 3D-mesh plots of waveguide output, (a) V = 0 V, (b) V = 100 V

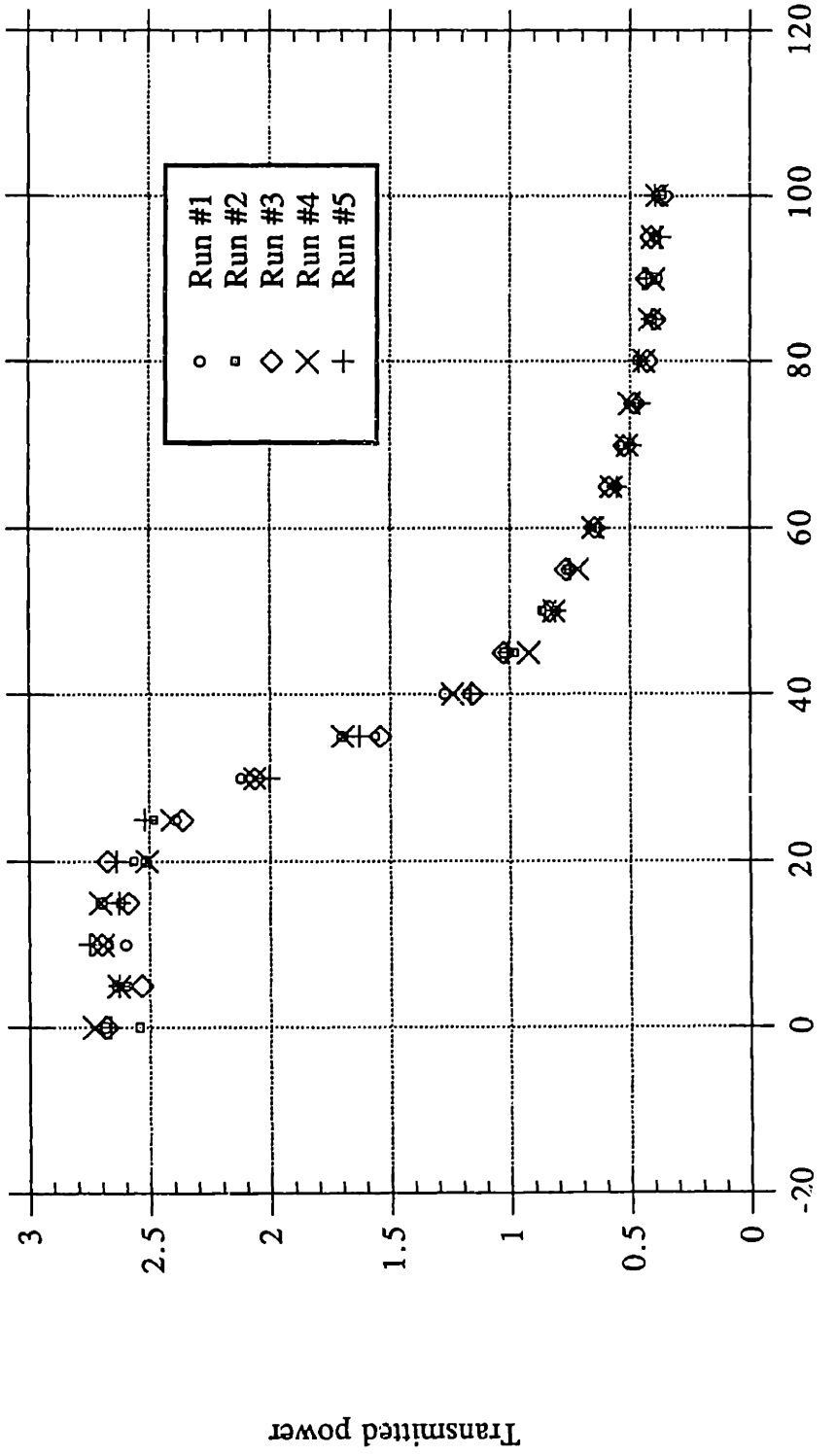

Fig. 53 Transmitted power vs. applied voltage for assembled sensor chip

combined with the fact that attenuation strengths at high-force levels are compatible with simulation results, implies some sort of scaling error along the horizontal axis. Hence, the difference between the experimental and simulation results is most likely due to a mechanical effect and not a misunderstanding of the optical interaction. Although the diaphragm is expected to exert a force back on the piezoelectric stack which tends to reduce its displacement, the actual resistance appears to be much greater than that which would be predicted from a simple mechanical model. It is hypothesized that this increase in reaction force seen by the piezoelectric stack could be due to trapped particles, which inhibit the free displacement of the diaphragm part.

In order to rule out other mechanical effects, a number of observations were noted:

1) Performing the entire test after replacing the ball-bearing point load with a large area (1 cm x 1 cm) loading plate removed the optical modulation effect completely. This rules out most effects due to translation of the testing structure, since the outer parts of the structure should be effectively seeing the same load in either case.

2) A mechanical indicator sensitive to sub-micron tip displacement was used at various points throughout the testing structure during actuation of the piezoelectric element. No substantial changes in position were measured.

3) To eliminate the possibility that the entire chip was translating upon piezoelectric loading, the coordinates of the output beam were recorded while voltage was applied. Since the magnified output beam showed no significant movement on a CCD camera which

was capable of resolving beam motion on the order of 0.25 μm, it was concluded that chip translation was not a major effect.

4) The waveguide access channels were designed to allow trapped gas between the two silicon wafers to escape. To eliminate the possibility that these channels had inadvertantly sealed, resulting in a significant back pressure, calculations were performed to determine the possible effect of trapped gas within the cavity. Using standard formulas for the trapped gas, the worst-case effect was still two orders of magnitude too low to explain the data.

5) Diaphragms were removed from some of the test chips, and the area underneath appeared relatively clear. Thus the structure did not become sealed shut during processing and was free of any large scale obstruction.

In addition to the elimination of the factors described above, a number of observations were made which directly support the particle hypothesis. Particle counts on slab ARROW wafers were measured using an automatic wafer inspection system (Aeronca Electronics, WIS 150). This system monitors the laser light reflected from a wafer surface for scattering and can detect particles larger than 0.1 μm in size. Typical measurements fell in the range of 2000-4000 particles per wafer, which translates to an average of 1.6 - 3.2 particles per active sensor area. Additional evidence for particulates, which have apparently reflowed to form columnar structures between the diaphragm and waveguide wafers, has been found in scanning electron micrographs such as Fig. 54. From measurements taken on wafers at intermediate steps in the fabrication process, it appears that these particulates come from the LTO deposition step.

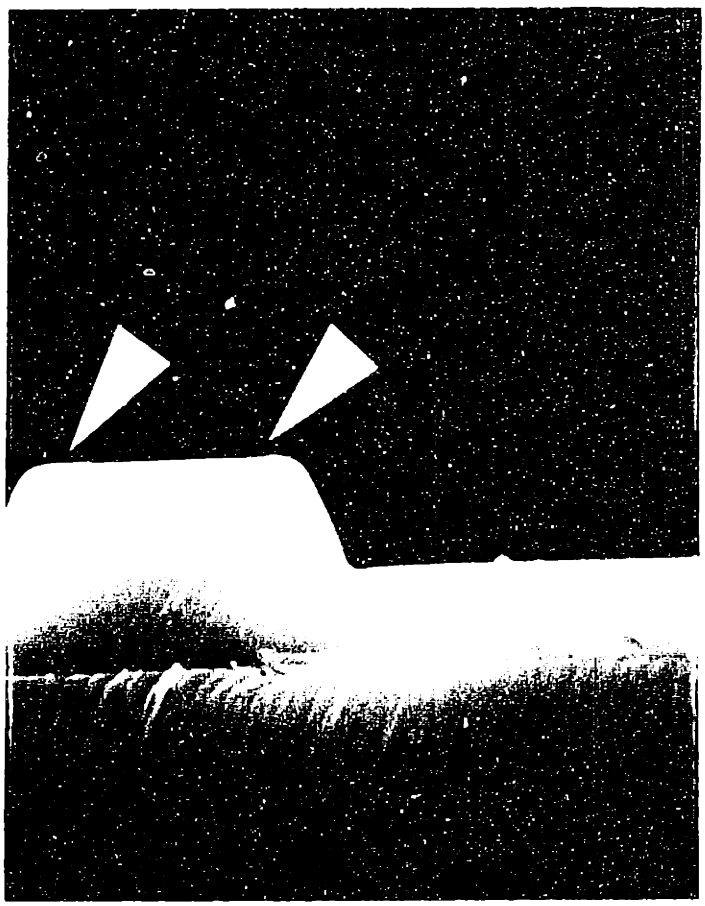

Fig. 54 Scanning electron micrograph showing columnar structures between waveguide ridge and silicon attenuator

Low temperature deposition of silicon dioxide depends on a reaction between silicon dioxide and oxygen at the wafer surface to form the desired layer. In our experiments, a distributed feed LPCVD reactor was used for the deposition process. The distributed feed was required due to the substantial depletion of reactants in the furnace tube. However, in addition to the surface reaction, a homogeneous gas-phase nucleation process typically occurs as well, and this contributes to particulate contamination in the LTO films. It is the finding of this work that LTO films may not be the best choice for use in evanescent optical waveguiding sensors due to this particulate problem. Other silicon dioxides formed by processes run at higher temperature, such as tetraethyl orthosilicate (TEOS) decomposition near 800° C or the reaction of dichlorosilane and nitrous oxide at 900° C have been shown to offer better film quality, and may be more suitable for use in sensor design.

In order to more completely analyze the particulate problem, mechanical simulations were performed using the COSMOS and ProEngineer software packages to determine the effect a particle has on the shape of diaphragm deflection. A particle obstruction was modelled as an immovable boundary condition at that point. Pressure was then applied to the computer generated model of a 2 x 2 mm silicon diaphragm fixed over a 1 μm gap, and the expected deflection over the centerline path was extracted. It is this centerline deflection that represents the path that the optical waveguide will interact with. Results are shown in Fig. 55. For a particle modelled by an immovable point midway between the diaphragm center and corner, little effect on deflection is seen. The effect corresponds to roughly a 20% reduction in the expected response versus applied pressure. In Fig. 56, the effect of moving a single obstruction point along the diagonal axis is shown. As the particle approaches the center, there is a strong effect on the diaphragm displacement, as expected. Thus it is expected that if the particle contamination problem is low, the effect on many of

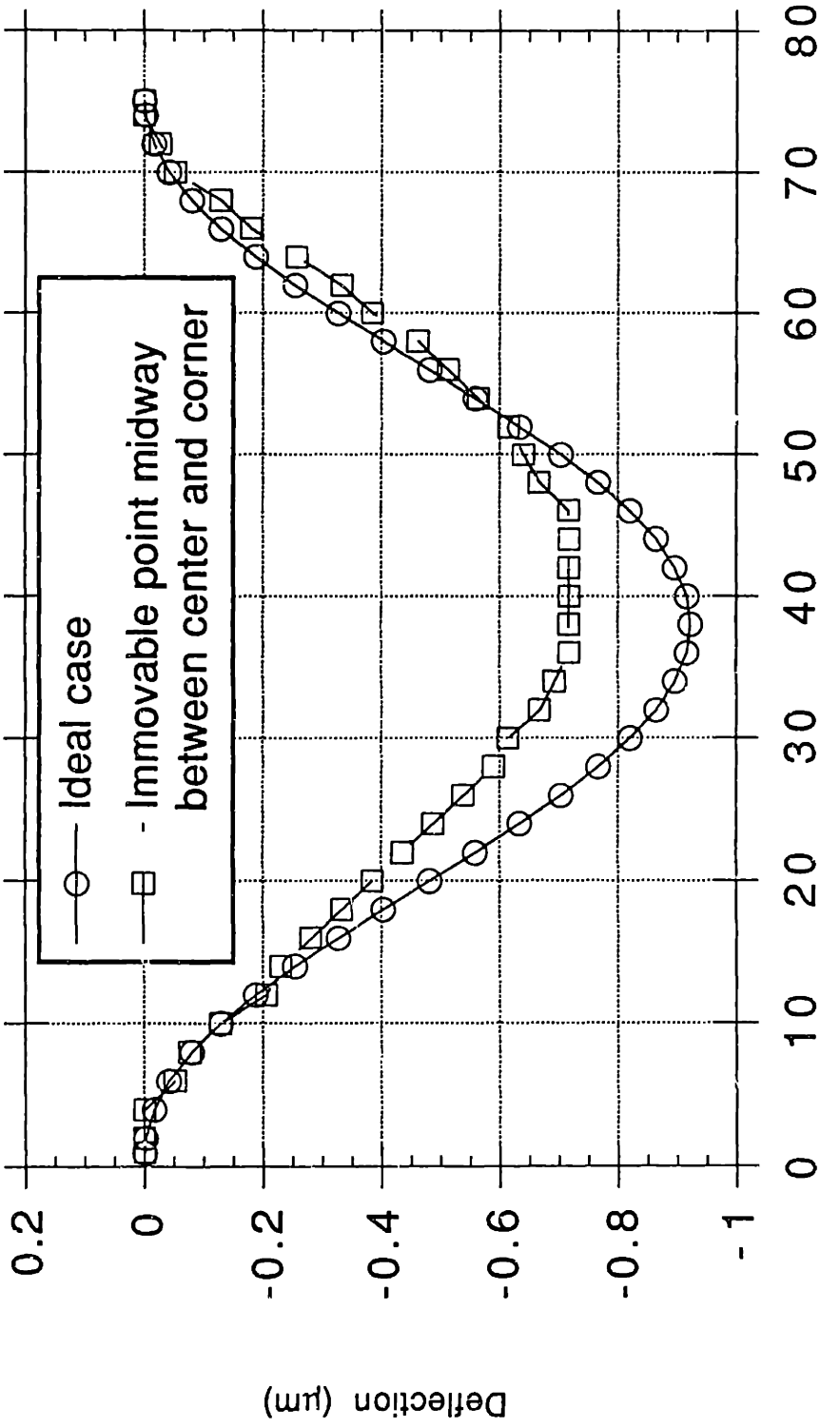

Fig. 55 Simulation of centerline deflection seen by waveguide

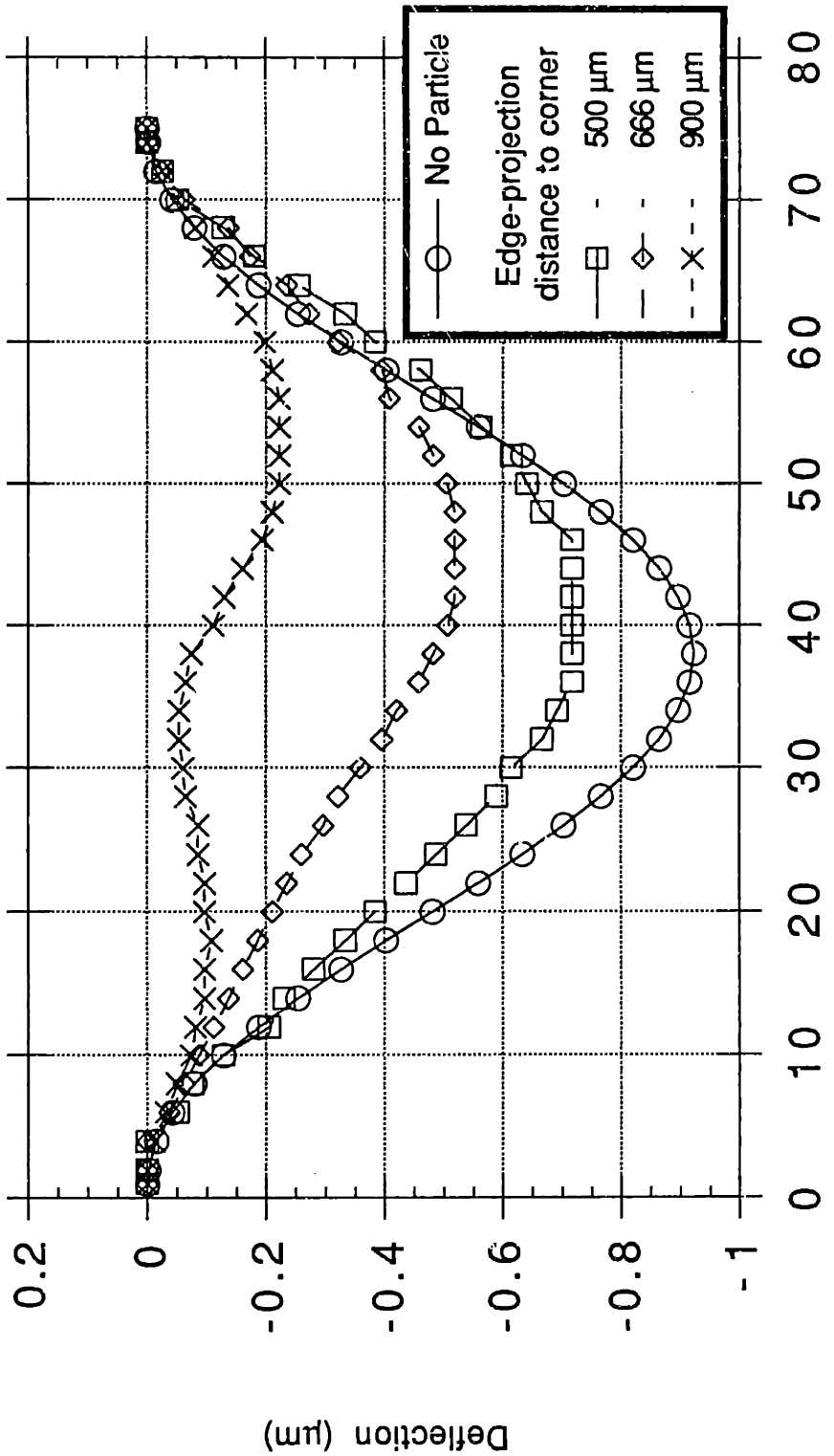

Fig. 56 Effect of single obstruction point along diagonal axis

these devices should be minimal. However, if there is a high concentration of particles involved, sensor operation will be hampered severely. The particle count measurements from the wafer inspection system indicate that this is potentially a serious effect. The above analysis suggests modelling the effect of particulates as a high effective spring constant acting back on the diaphragm in response to applied load. A curve-fit to the experimental data can be performed using this model in conjunction with VBPM results and is shown in Fig 57. Although the fit uses a somewhat arbitrary point of zero reference and a fitting parameter corresponding to the effective spring constant, it does provide evidence for the plausibility of this hypothesis.

In summary, particulate contamination was observed on the surface of the ARROW wafers under study and also in scanning electron micrographs of assembled sensor chips. The source of these particles was identified as the low-temperature silicon dioxide deposition step. Mechanical modelling demonstrates that the effect of these particles can explain the experimentally observed response of the sensor to piezoelectric loading. The effect of these particles can be modelled as a high effective spring constant acting back on the diaphragm in response to applied load. This has the effect of dramatically changing the sensor response (from 50 to 15000 psi full-scale). A number of experimental and theoretical checks have been performed that are consistent with this hypothesis. Process suggestions to reduce particulate count are described here; other methods which may be useful in circumventing the particulate problem are outlined in the following chapter.

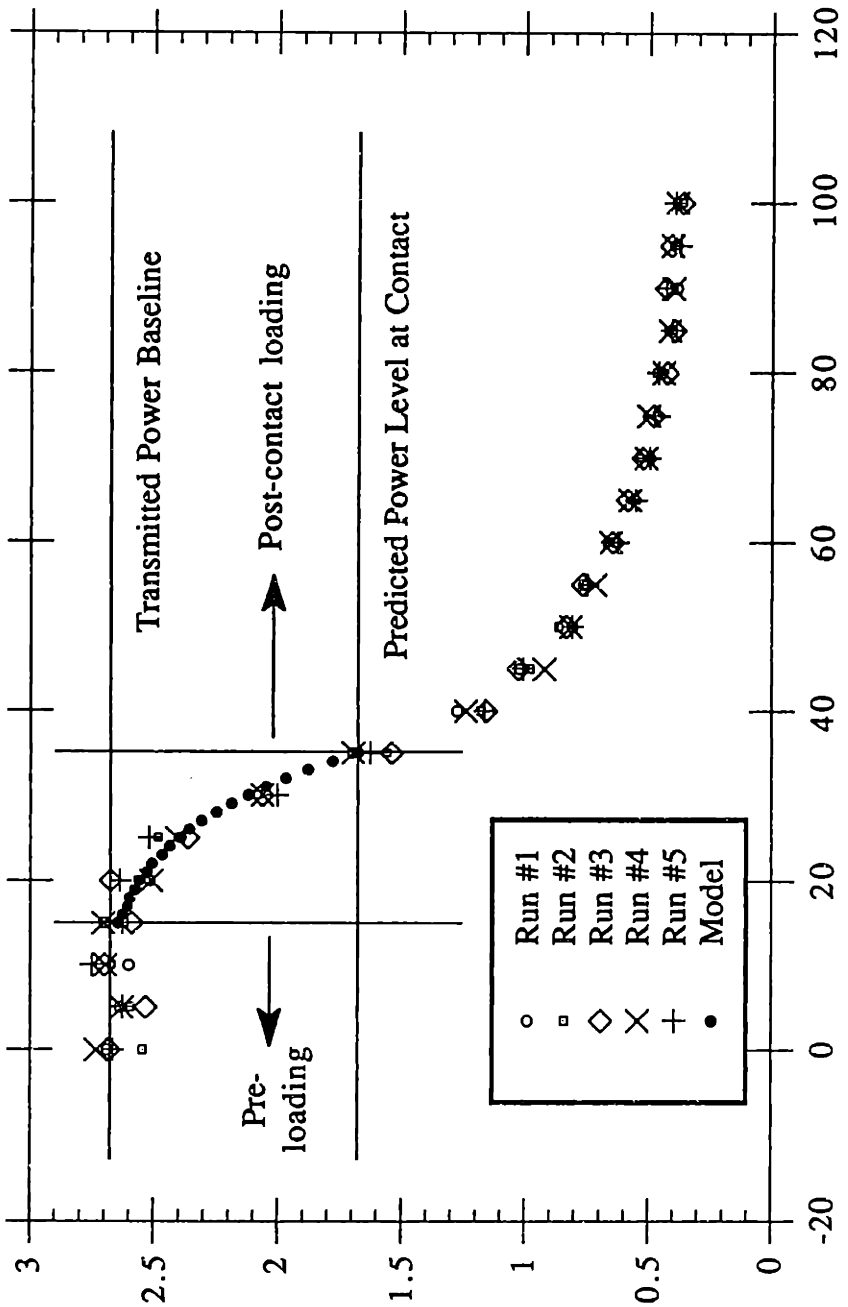

Fig. 57 Linear effective spring constant model fitted to experimental results

Chapter 6

Conclusions

In this work, the ARROW waveguide structure was investigated and implemented in a microfabricated pressure transducer design. The first goal was to more fully understand the waveguiding characteristics of the ARROW structure and to determine whether ARROW waveguides had any advantages over standard waveguiding geometries. A second goal was to study the interaction of an ARROW waveguide with a leakage enhancing microstructure, and to determine whether a sensor could be built based on such an evanescent loss principle. A final goal was to use simulation tools to aid in device design and to compare the experimental results with various simulation predictions. Each one of these issues will be described further below. In addition, a brief discussion of future design considerations will follow.

6.1 Review of Basic Findings

ARROW waveguides were found to offer good process latitude and general ease of fabrication. Fabrication of the full ARROW structure requires only one extra process step over the standard waveguide process. In return for this one extra step, ARROW

waveguides provide much better coupling efficiencies with optical fibers. Theoretical modelling also demonstrated improvements in longitudinal and transverse alignment tolerances, with a corresponding degradation in angular tolerance. Transverse and longitudinal coupling tolerances were also studied experimentally and were both found to be quite good.

It has been demonstrated that evanescent loss effects can be used to detect the interaction between a waveguide and a leakage-inducing attenuator. Experiments have shown that an assembled sensor chip can respond measurably to pressure applied from a piezoelectric load. The extent of attenuation and the output mode-shapes observed appear to agree with simulated predictions. However, the issue of entrapped particles must be addressed before this technique can be implemented reliably. Since this sensor design has the most intense interactions at very small gap spacings, the issue becomes of critical importance. These particles appear to be process specific and may be reduced in number. Unfortunately, it was found that even the use of an LTO process in conjunction with clean room assembly of the two components was not sufficient to completely eliminate the problem. The effect can be modelled as a strong linear spring constant in the region from no-deflection to the expected point of contact between the two components. This has the effect of dramatically changing the range of full-scale operation. Although this model can be used to fit experimental data, it is of limited use in the prediction of sensor response.

First order theoretical and numerical simulation models were successful in discovering the salient features of device operation, with the exception of the particulate problem described above. Propagation characteristics were analyzed using a wide variety of numerical methods. The interaction of the attenuator with the waveguide was analyzed by varying both gap spacing and the real and imaginary components of the attenuator index in 2D-VBPM simulations. Mode stability and profile were analyzed using a 3D-VBPM

method. The effect of ridge-etch depth on the interaction effect was assessed using an eigen-solver technique. Numerical simulation work was important in clarifying gaps in understanding and identifying possible weak assumptions in the theoretical modelling. The VBPM methods used were quite successful, although full three-dimensional simulations were often time consuming and may be replaced in some cases by eigen-solver techniques.

6.2 Future Design Considerations

With the review of basic findings complete, the discussion in this section centers around methods to improve the design of the sensor and the future scalability of this technology to smaller dimensions. Improvement of device performance centers around finding a method to solve the particulate problem, thus improving the quality of the interaction between the waveguide and the attenuator. For example, if the particulate problem remains unsolved, scaling the diaphragm thickness will have little effect on the full-scale range of device operation. One way to address the particulate problem is to improve the surface quality of the core layer, which should greatly improve the leakage interaction. This can be accomplished by using a different chemistry, such as TEOS decomposition or the reaction of dichlorosilane and nitrous oxide, to achieve core depositions of higher quality. In addition, surface polishing after core deposition may improve performance. However, this is a non-trivial procedure, as SiO_2 is a relatively difficult material to polish. Attention must also be paid to the overall thickness of the core under oxide polishing conditions.

While these methods should reduce the particulate count in the spacer layer gap region, they appear unlikely to completely eliminate the problem. Another possibility is to accept the existence of a small number of particles and to use a multimode waveguide or

many single-mode waveguides in a star configuration to attempt to spread out the effect of any particulates that do remain in the gap. An even more promising approach may be to attempt to increase the range of interaction between the waveguide and attenuator. This might be achieved by etching perturbations such as gratings into the waveguide surface, or by the use of hollow-core waveguides which have long distances of interaction in air. In addition to extending the range of the evanescent tail, one can also attempt to increase sensitivity by increasing the strength of the interaction between the two components. There are three ways to achieve this: 1) increase the effective interaction length, which can be accomplished by simply enlarging the device, but may also be accomplished by adding reflectors at the waveguide end-faces to increase the number of passes through the interaction region, 2) use a low index material such as glass to further enhance the expected leakage, and 3) change the spatial profile of the beam so that it extends further away from the core region. With these ideas in mind, a new design might incorporate the following features: a polished core layer, a glass attenuator, very deeply etched ridges, and reflecting end-faces to increase the effective path length. These types of changes can be made regardless of whether one is using ARROW or standard waveguiding geometries.

Another topic of interest is the scalability of this technology to smaller dimensions. The concerns here are primarily those of mode structure. It was shown already that the small mismatch between the fiber input and ARROW waveguide modes required a stabilization region on the order of 2 mm. For devices on the order of 1 cm in length, such as those tested in this work, higher-order modes are radiated away and do not appear to be a major problem in alignment. However, the situation can be expected to change as device dimensions are pushed further down. For smaller devices, where the structure itself does not have the time to filter out unwanted modes, accurate mode coupling is essential. This poses an interesting difficulty when dealing with the ARROW waveguide, since it can

support higher-order modes even though they experience much higher degrees of loss. Usually these modes are ignored, since the next higher mode, which exhibits the next lowest loss, experiences over 80 times the loss of the fundamental. However, if the fundamental mode shows only 0.09 dB/cm loss, then this corresponds to only a 7.3 dB/cm loss figure for the next higher mode. As chip dimensions go down below 1 cm, the loss over the chip length is no longer significant and this higher-order mode can enter into the measurement. Thus, as chip dimensions are driven downward, the requirements on modal discrimination become much more stringent. It is possible that it will be desirable to design slightly less than optimal waveguides for fundamental mode propagation in order to obtain higher losses for the higher order modes. This can be achieved by designing cladding layers that are poorer reflectors and by designing waveguide sidewall etches that induce more scattering, since higher-order modes will interact more strongly with the waveguide sidewalls. In addition, the use of an absorbing layer such as polysilicon for the first cladding layer could prove beneficial.

If undesired modes are not removed, they can pose problems during alignment. Thus, as ARROW devices are scaled down, the advantages in coupling efficiency and alignment tolerance may not necessarily outweigh the introduction of these other modes. As long as there is sufficient available input power, even a standard waveguide with high insertion loss might be a more acceptable alternative.

6.3 Concluding Remarks

The ARROW waveguide represents an important class of waveguiding structures and has many potential advantages. Although silicon nitride waveguides appear to offer a partial fix to the problem of particulate contamination in general-purpose evanescent-

sensors, the ARROW structure has advantages that should not be overlooked. The ARROW structure may have its greatest advantages in applications where high coupling efficiency is required. This will include important applications involving low available input power, and systems configured for higher levels of sensor integration. In addition, if the problems with particulates can be solved, the general use of ARROW waveguides with microstructures for evanescent sensing will most likely be worth the extra effort. It is hoped that this work opens the door for many more studies to come.

References

[1] H. Kogelnik, "An introduction to integrated optics," *IEEE Trans. on Microwave Theory and Techniques*, vol. MTT-23, no. 1, pp. 2-16, Jan. 1975.

[2] R. G. Hunsperger, *Integrated Optics: Theory and Technology*, Springer Series on Optical Sciences, vol. 33, Springer-Verlag, Berlin, 1984.

[3] T. Tamir (ed.), *Guided Wave Optoelectronics*, Topics in Applied Physics, vol. 7, Springer-Verlag, Berlin, 1988.

[4] D. G. Hall, "Survey of silicon-based integrated optics," *Computer*, pp. 25-32, Dec. 1987.

[5] J. T. Boyd, R. W. Wu, D. E. Zelmon, A. Naumann, H. A. Timlin, and H. E. Jackson, "Guided wave optical structures utilizing silicon," *Opt. Eng.*, vol. 24, no. 2, pp. 230-234, Mar./Apr. 1985.

[6] K. E. Petersen, "Silicon as a mechanical material," *Proc. IEEE*, vol. 70, no. 5, pp. 420-457, May 1982.

[7] K. E. Bean, "Anisotropic etching of silicon," *IEEE Trans. Electron Devices*, vol. ED-25, no. 10, pp. 1185-1193, 1978.

[8] R. Jebens, W. Trimmer, and J. Walker, "Micro actuators for aligning optical fibers," *Proc. IEEE Micro Electro Mechanical Systems Workshop*, pp. 35-39, Salt Lake City, Utah, Feb. 1989.

[9] C. H. Henry, G. E. Blonder, and R. F. Kazarinov, "Glass waveguides on silicon for hybrid optical packaging," *J. Lightwave Tech.*, vol. 7, no. 10, pp. 1530-1539, Oct. 1989.

[10] C. H. Henry, R.F. Kazarinov, H. J. Lee, K. J. Orlowsky, and L. E. Katz, "Low loss Si_3N_4-SiO_2 optical waveguides on Si," *Appl. Opt.*, vol. 26, no. 13, pp. 2621-2624, July 1, 1987.

[11] W. Stutius, and W. Streifer, "Silicon nitride films on silicon for optical waveguides," *Appl. Opt.*, vol. 16, pp. 3218-3222, 1977.

[12] M. del Guidice, F. Bruno, T. Cicinelli, and M. Valli, "Structural and optical properties of silicon oxynitride on silicon planar waveguides," *Appl. Opt.*, vol. 29, no. 24, pp. 3489-3496, Aug. 20, 1990.

[13] H. J. Lee, C. H. Henry, K. J. Orlowsky, R. F. Kazarinov, and T. Y. Kometani, "Refractive-index dispersion of phosphosilicate glass, thermal oxide, and silicon nitride films on silicon," *Appl. Opt.*, vol. 27, no. 19, pp. 4104-4109, Oct. 1, 1988.

[14] T. Miyashita, S. Sumida, and S. Sakaguchi, "Integrated optical devices based on silica waveguide technologies," *Integrated Optical Circuit Engineering VI*, SPIE vol. 993, pp. 288-294, 1988.

[15] S. K. Clark and K. D. Wise, "Pressure sensitivity in anisotropically etched thin-diaphragm pressure sensors," *IEEE Trans. Electron Devices*, vol. ED-26, no. 12, pp. 1887-1896, Dec. 1979.

[16] T. Ishihara, K. Suzuki, S. Suwazono, M. Hirata, and H. Tanigawa, "CMOS integrated silicon pressure sensor," *IEEE J. Solid-State Circuits*, vol. SC-22, no. 2, pp. 151-155, Apr. 1987.

[17] H. Tanigawa, T. Ishihara, M. Hirata, and K. Suzuki, "MOS integrated silicon pressure sensor," *IEEE Trans. Electron Devices*, vol. ED-32, no. 7, pp. 1191-1195, July 1985.

[18] V. Mosser, J. Suski, J. Goss, and E. Obermeier, "Piezoresistive pressure sensors based on polycrystalline silicon," *Sensors and Actuators A*, vol. 28, pp. 113-132, 1991.

[19] H. Guckel, "Surface micromachined pressure transducers," *Sensors and Actuators A*, vol. 28, pp. 133-146, 1991.

[20] C. D. Fung and W. H. Ko, "Miniature capacitive pressure transducer," *Sensors and Actuators*, vol. 2, pp. 321-326, 1982.

[21] Y. S. Lee and K. D. Wise, "A batch-fabricated silicon capacitive pressure transducer with low temperature sensitivity," *IEEE Trans. Electron Devices*, vol. ED-29, no. 1, pp. 42-48, Jan. 1982.

[22] W. H. Ko, M. H. Bao, and Y. D. Hong, "A high sensitivity integrated-circuit capacitive pressure transducer," *IEEE Trans. Electron Devices*, vol. ED-29, no. 1, pp. 48-56, Jan. 1982.

[23] J. T. Kung, H.S. Lee, and R.T. Howe, "A digital readout technique for capacitive sensor applications," *IEEE J. Solid-State Circuits*, vol. 23, no. 4, pp. 972-977, Aug. 1988.

[24] D. J. Warkentin, J. H. Haritonidis, M. Mehregany, and S. D. Senturia, "A micromachined microphone with optical interference readout," *Transducers '87, Tech. Dig.*, Tokyo, pp. 291-294, June 1987.

[25] A. M. Young, J. E. Goldsberry, J. H. Haritonidis, R. L. Smith, and S. D. Senturia, "A twin-interferometer fiber-optic readout for diaphragm pressure transducers," *Tech. Dig. IEEE Solid-State Sensor and Actuator Workshop*, pp. 19-22, Hilton Head Island, S.C., June 1988.

[26] M. Watanabe, M. Katagiri, and M. Hijikigawa, "Fiber optic digital force sensor based on double cavity configuration," *Transducers '87, Tech. Dig.*, Tokyo, pp. 208-211, June 1987.

[27] T.S.J. Lammerink and S. J. Gerritsen, "Fiber-optic sensors based on resonating mechanical structures," *Fiber Optic Sensors II*, SPIE vol. 798, pp. 67-71, 1987.

[28] B. E. Jones and G. S. Philp, "A fibre optic pressure sensor using reflective techniques," *Proc. Int'l. Conf. on Optical Techniques in Process Control*, The Hague, Neth., pp. 11-25, June 1983.

[29] W. R. Seitz, "Chemical sensors based on fiber optics," *Anal. Chem.*, vol. 56, no. 1, pp. 16A-34A, 1984.

[30] W. V. Sorin, "Evanescent field devices using single-mode optical fibers," Ph. D. Thesis, Stanford University, 1986.

[31] A. N. Chester, S. Martellucci, and A. M. Verga Scheggi (eds.), *Optical Fiber Sensors*, NATO ASI Series E., no. 132, Martinus Nijhoff Publishers, Dordrecht, 1987.

[32] S. Valette, S. Renard, J. P. Jadot, P. Gidon, and C. Erbeia, "Silicon-based integrated optics technology for optical sensor applications," *Sensors and Actuators*, vol. A21-23, pp. 1087-1091, 1990.

[33] D. Peters, K. Fischer, and J. Muller, "Integrated optics based on silicon oxynitride thin films deposited on silicon substrates for sensor applications," *Sensors and Actuators*, vol. A25-27, pp. 425-431, 1991.

[34] M. F. Sultan, "Planar polymer light guide networks: application to differential position sensors," *Fiber Optic and Laser Sensors VI*, SPIE vol. 985, Boston, pp. 327-337, Sept. 1988.

[35] K. E. Burcham, G. N. De Brabander, and J. T. Boyd, "Micromachined silicon cantilever beam accelerometer incorporating an integrated optical waveguide," *Integrated Optics and Microstructures*, SPIE vol. 1793, Boston, pp. 12-18, 1992.

[36] M. Ohkawa, M. Izutsu, and T. Sueta, "Integrated optic pressure sensor on silicon substrate," *Appl. Opt.*, vol. 28, no. 23, pp. 5153-5157, Dec. 1, 1989.

[37] J. J. Isaac, R. M. De La Rue, and K. K. Wong, "An integrated optical pressure sensor in III-V semiconductor material," *Fibre Optic Sensors*, IOP Short Meetings Series No. 7, pp. 105-108, IOP Publishing Ltd., Glasgow, July 1987.

[38] A. Nathan, Y. Bhatnagar, A. Vadekar, and W. Huang, "Fabrication of a silicon Mach-Zehnder interferometer for mechanical measurands," *Integrated Optics and Microstructures*, SPIE vol. 1793, Boston, pp. 19-26, 1992.

[39] R. Kersten, "Integrated Optical Sensors," in *Optical Fiber Sensors*, A. N. Chester, et. al. (eds.), NATO ASI Series E, no. 132, Martinus Nijhoff Publishers, Dordrecht, 1987.

[40] A. A. Boiarski, J. R. Busch, B. S. Bhullar, R. W. Ridgway, and V. E. Wood, "Integrated-optic sensor with macro-flow cell," *Integrated Optics and Microstructures*, SPIE vol. 1793, Boston, pp.199-211, 1992.

[41] W. Lukosz and P. Plinka, "Integrated optical nanomechanical light modulators and microphones," *Sensors and Materials*, vol. 3, no. 5, pp. 261-280, 1992.

[42] W. Lukosz and P. Plinka, "Integrated optical interferometer as a light modulator and microphone," *Sensors and Actuators A*, vol. 25-27, pp. 337-340, 1991.

[43] W. Lukosz and P. Plinka, "Nanomechano-grating-coupler-modulator and integrated optical microphone," *Proc. 5th European Conf. on Integrated Optics*, Paris, SPIE vol. 1141, pp. 201-207, 1989.

[44] D. Botez, L. J. Mawst, G. Peterson, and T.J. Roth, "Resonant optical transmission and coupling in phase-locked diode laser arrays of anti-guides: the resonant optical waveguide array," *Appl. Phys. Lett.*, vol. 54, no. 22, pp. 2183-2185, May 29, 1989.

[45] T. L. Koch, W. T. Tsang, and P. J. Corvini, "Spectral dependence of propagation loss in InP/InGaAsP antiresonant reflecting optical waveguides grown by chemical beam epitaxy," *Appl. Phys. Lett.*, vol. 50, no. 6, pp. 307-309, Feb. 9, 1987.

[46] T. L. Koch, E. G. Burkhardt, F. G. Storz, T. J. Bridges, and T. Sizer, "Vertically grating-coupled ARROW structures for III-V integrated optics," *IEEE J. Quant. Elec.*, vol. QE-23, no. 6, pp. 889-897, June 1987.

[47] T. L. Koch, P. J. Corvini, W. T. Tsang, U. Koren, and B. I. Miller, "Wavelength selective interlayer directionally grating-coupled InP/InGaAsP waveguide photodetection," *Appl. Phys. Lett.*, vol. 51, no. 14, pp. 1060-1062, Oct. 5, 1987.

[48] T. L. Koch, U. Koren, G. D. Boyd, P. J. Corvini, and M. A. Duguay, "Antiresonant reflecting optical waveguides for III-V integrated optics," *Elec. Lett.*, vol. 23, no. 5, pp. 244-245, Feb. 26, 1987.

[49] M. A. Duguay, Y. Kokubun, T.L. Koch, and L. Pfieffer, "Antiresonant reflecting optical waveguides in SiO_2-Si multilayer structures," *Appl. Phys. Lett.*, vol. 49, no. 1, pp. 13-14, July 7, 1986.

[50] T. Baba, Y. Kokubun, and H. Watanabe, "Monolithic integration of an ARROW-type demultiplexer and photodetector in the shorter wavelength region," *J. Lightwave Tech.*, vol. 8, no. 1, pp. 99-104, Jan. 1990.

[51] M. Cantin, C. Carignan, R. Côté, M. A. Duguay, R. Larose, P. LeBel, and F. Ouellette, "Remotely switched hollow-core antiresonant reflecting optical waveguide," *Opt. Lett.*, vol. 16, no. 22, pp. 1738-1740, Nov. 15, 1991.

[52] J.-L. Archambault, R. J. Black, S. Lacroix, and J. Bures, "Loss calculations for antiresonant waveguides," *J. Lightwave Tech.*, vol. 11, no. 3, pp. 416-423, Mar. 1993.

[53] T. Baba and Y. Kokubun, "Dispersion and radiation loss characteristics of antiresonant reflecting optical waveguides - numerical results and analytical expression," *IEEE J. Quant. Elec.*, vol. 28, no. 7, pp. 1689-1700, July 1992.

[54] T. Baba and Y. Kokubun, "Scattering loss of antiresonant reflecting optical waveguides," *J. Lightwave Tech.*, vol. 9, no. 5, pp. 590-597, May 1991.

[55] T. Baba and Y. Kokubun, "High efficiency light coupling from antiresonant reflecting optical waveguide to integrated photodetector using an antireflecting layer," *Appl. Opt.*, vol. 29, no. 18, pp. 2781-2792, June 20, 1990.

[56] T. Baba and Y. Kokubun, "New polarization-insensitive antiresonant reflecting optical waveguide (ARROW-B)," *IEEE Phot. Tech. Lett.*, vol. 1, no. 8, pp. 232-234, Aug. 1989.

[57] T. Baba, Y. Kokubun, T. Sakaki, and K. Iga, "Loss reduction of an ARROW waveguide in shorter wavelength and its stack configuration," *J. Lightwave Tech.*, vol. 6, no. 9, pp. 1440-1445, Sept. 1988.

[58] J. C. Grant, J. C. Beal, and N.J.P. Frenette, "Solving certain leaky waveguides with lossless, simply bounded finite element modeling," *IEEE Phot. Tech. Lett.*, vol. 2, no. 12, pp. 890-892, Dec. 1990.

[59] W. Jiang, J. Chrostowski, and M. Fontaine, "Analysis of ARROW waveguides," *Opt. Comm.*, vol. 72, no. 3,4, pp. 180-186, July 15, 1989.

[60] Y. Kokubun, T. Baba, T. Sakaki, and K. Iga, "Low-loss antiresonant reflecting optical waveguide on Si substrate in visible-wavelength region," *Elec. Lett.*, vol. 22, no. 17, pp. 892-893, Aug. 14, 1986.

[61] J. M. Kubica, "Numerical analysis of InP/InGaAsP ARROW waveguides using transfer matrix approach," *J. Lightwave Tech.*, vol. 10, no. 6, pp. 767-771, June 1992.

[62] J. Kubica, D. Uttamchandani, and B. Culshaw, "Modal propagation within ARROW waveguides," *Opt. Comm.*, vol. 78, no. 2, pp. 133-136, Aug. 15, 1990.

[63] M. Mann, U. Trutschel, C. Wächter, L. Leine, and F. Lederer, "Directional coupler based on an antiresonant reflecting optical waveguide," *Opt. Lett.*, vol. 16, no. 11, pp. 805-807, June 1, 1991.

[64] T. Sakamoto and Y. Kokubun, "Monolithic integration of photodetector and ARROW-type interferometer for detecting phase difference between two optical paths," *Jap. J. Appl. Phys.*, vol. 29, no. 1, pp. L96-L98, Jan. 1990.

[65] R. A. Soref and K. J. Ritter, "Silicon antiresonant reflecting optical waveguides," *Opt. Lett.*, vol. 15, no. 14, pp. 792-794, July 15, 1990.

[66] U. Trutschel, M. Mann, F. Lederer, C. Wächter, and A. D. Boardman, "Nonlinear switching in coupled antiresonant reflecting optical waveguides," *Appl. Phys. Lett.*, vol. 59, no. 16, pp. 1940-1942, Oct. 14, 1991.

[67] M. S. Wartak, J. Chrostowski, W. Jiang, and B. A. Syrett, "Chromatic dispersion in ARROW waveguides," *Opt. Comm.*, vol. 76, no. 3,4, pp. 217-219, May 1, 1990.

[68] A. M. Young, C. Xu, W. Huang, and S. D. Senturia, "Design and analysis of an ARROW-waveguide-based silicon pressure transducer," *Integrated Optics and Microstructures*, SPIE vol. 1793, Boston, pp. 42-53, 1992.

[69] D. Marcuse, "Loss analysis of single mode fibre splices," *Bell Syst. Tech. J.*, vol. 56, p. 703, 1977.

[70] A. K. Ghatak and K. Thyagarajan, *Optical Electronics*, Cambridge University Press, Cambridge, p. 415, 1989.

[71] R. Ulrich, "Theory of the prism-film coupler by plane-wave analysis," *J. Opt. Soc. Am.*, vol. 60, no. 10, pp. 1337-1350, Oct. 1970.

[72] A. K. Ghatak, K. Thyagarajan, and M. R. Shenoy, "Numerical analysis of planar optical waveguides using matrix approach," *IEEE J. Lightwave Tech.*, vol. LT-5, no. 5, pp. 660-667, May 1987.

[73] A. K. Ghatak, "Leaky modes in optical waveguides," *Opt. and Quant. Electronics*, vol. 17, pp. 311-321, 1985.

[74] K. Thyagarajan, S. Diggavi, and A. K. Ghatak, "Analytical investigations of leaky and absorbing planar structures," *Opt. and Quant. Electronics*, vol. 19, pp. 131-137, 1987.

[75] M. R. Ramadas, E. Garmire, A. K. Ghatak, K. Thyagarajan, and M. R. Shenoy, "Analysis of absorbing and leaky planar waveguides: a novel method," *Opt. Lett.*, vol. 14, no. 7, pp. 376-378, Apr. 1, 1989.

[76] H. A. Haus and D.A.B. Miller, "Attenuation of cutoff modes and leaky modes of dielectric slab structures," *IEEE J. Quant. Elec.*, vol. QE-22, no. 2, pp. 310-318, Feb. 2, 1986.

[77] D. B. Hall and C. Yeh, "Leaky waves in a heteroepitaxial film," *J. Appl. Phys.*, vol. 44, no. 5, pp. 2271-2274, May 1973.

[78] P. Yeh, *Optical waves in layered media*, John Wiley & Sons, Inc., New York, 1988.

[79] Y. Chung and N. Dagli, "An assessment of finite difference beam propagation method," *IEEE J. Quant. Elec.*, vol. 26, no. 8, pp. 1335-1339, 1990.

[80] W. P. Huang and C. L. Xu, "Simulation of 3-D optical waveguides by a full-vector beam propagation method," *IEEE J. Quant. Elec.*, vol. 29, no. 10, pp. 2639-2649, Oct. 1993.

[81] W. P. Huang, C. L. Xu, and S. K. Chaudhuri, "A finite-difference vector beam propagation method for three-dimensional waveguide structures," *IEEE Phot. Tech. Lett.*, vol. 4, no. 2, pp. 148-151, Feb. 1992.

[82] W. P. Huang, C. L. Xu, S. T. Chu, and S. K. Chaudhuri, "The finite-difference vector beam propagation method: analysis and assessment", *J. Lightwave Tech.*, vol. 10, no. 3, pp. 295-305, 1992.

[83] W. P. Huang, C. L. Xu, S. T. Chu, and S. K. Chaudhuri, "A vector beam propagation method for guided-wave optics," *IEEE Phot. Tech. Lett.*, vol. 3, no. 10, pp. 910-913, Oct. 1991.

[84] M. S. Stern, "Semivectorial polarised finite difference method for optical waveguides with arbitrary index profiles," *IEE Proc.*, vol. 135, pt. J, no. 1, pp. 56-63, Feb. 1988.

[85] C. L. Xu, W. P. Huang, and S. K. Chaudhuri, "Efficient and accurate vector mode calculations by beam propagation method," *J. Lightwave Tech.*, vol. 11, no. 7, pp. 1209-1215, July 1993.

[86] J. Lasky, S. Stiffler, F. White, and J. Abernathey, "Silicon-on-insulator (SOI) by bonding and etch-back," *Tech. Dig. Int'l. Electron Devices Meeting*, p. 684, Dec. 1985.

[87] W. P. Maszara, G. Goetz, A. Caviglia, and J.B. McKitterick, "Bonding of silicon wafers for silicon-on-insulator," *J. Appl. Phys.*, vol. 64, no. 10, pp. 4943-4950, Nov. 15, 1988.

[88] J. Haisma, G.A.C.M. Spierings, U.K.P. Biermann, and J. A. Pals, "Silicon-on-insulator wafer bonding-wafer thinning technological evaluations," *Jap. J. Appl. Phys.*, vol. 28, no. 8, pp. 1426-1443, Aug. 1989.

[89] T. Abe, M. Nakano, and T. Itoh, "Silicon wafer-bonding process technology for SOI structures," *Proc. 4th Int'l. Symp. on Silicon-on-Insulator Technology and Devices*, Montreal, May 1990.

[90] C. Harendt, W. Appel, H.-G. Graf, B. Höfflinger, and E. Penteker, "Wafer fusion bonding and its application to silicon-on-insulator fabrication," *J. Micromech. Microeng.*, vol. 1, pp. 145-151, 1991.

[91] A. Hanneborg, M. Nese, and Per Øhlckers, "Silicon-to-silicon anodic bonding with a borosilicate glass layer," *J. Micromech. Microeng.*, vol. 1, pp. 139-144, 1991.

[92] A. D. Brooks, R. P. Donovan, and C. A. Hardesty, "Low-temperature electrostatic silicon-to-silicon seals using sputtered borosilicate glass," *J. Electrochem. Soc.: Solid-State Science and Technology*, vol. 119, no. 4, pp. 545-546, Apr. 1972.

[93] R. D. Frye, J. E. Griffith, and Y. H. Wang, "A field-assisted bonding process for silicon dielectric isolation," *J. Electrochem. Soc.: Solid-State Science and Technology*, vol. 133, no. 8, pp. 1673-1677, Aug. 1986.

[94] T. R. Anthony, "Dielectric isolation of silicon by anodic bonding," *J. Appl. Phys.*, vol. 38, no. 3, pp. 1240-1247, Aug. 1, 1985.

[95] P. K. Tien, R. Ulrich, and R. J. Martin, "Modes of propagating light waves in thin deposited semiconductor films," *Appl. Phys. Lett.*, vol. 14, pp. 291-294, 1969.

[96] R. Ulrich and R. Torge, "Measurement of thin film parameters with a prism coupler," *Appl. Opt.*, vol. 12, no. 12, pp. 2901-2908, Dec. 1973.

[97] D. L. Lee, *Electromagnetic principles of integrated optics*, John Wiley & Sons, Inc., New York, 1986.